ECAP-2010-001

Calibration of acoustic sensors for deep-sea infrastructures and studies towards combined opto-acoustical modules

Diplomarbeit
von
Alexander Enzenhöfer

Januar 2010

Physikalisches Institut der Friedrich-Alexander-Universität Erlangen-Nürnberg

Contents

Part I

Introduction

Introduction

The generation of acoustic signals by elementary particles in water or similar media was first predicted in 1957 [1] and subsequently described by G.A. Askaryan and B.A. Dolgoshein in the so-called thermo-acoustic model [2]. According to the model, the energy deposition of a particle interaction in liquids leads to a local heating of the medium which can be regarded as instantaneous with respect to the hydrodynamic time scale. The temperature change forces the medium to expand or contract according to its volume expansion coefficient. The accelerated motion of the heated volume element transforms into a pressure pulse which propagates through the volume.

In the interactions of high energy particles in water, cascades form which deposit the energy into the water in a similar pattern and thus give rise to an acoustic signal. The attempt of detecting ultra-high energy (UHE) neutrinos with energies exceeding 100 PeV via such an acoustic signal instead of the conventional approach using Cherenkov light seems promising as the range of sound in water is much larger than for light. The sound attenuation length in water is of the order of 1 km (for the peak emission frequency) compared to the attenuation length for light of the order of 100 m. This larger range enlarges the sensor spacing and would make possible the construction of much larger detector volumes. Detector sizes of $\gtrsim 100\,\mathrm{km}^3$ are necessary in the UHE regime because of the expected low flux cosmic ν's have, without the feasibility to increase the number of individual detector elements by the same factor. Thus, the possible size for water Cherenkov neutrino telescopes is most likely limited to a few cubic kilometres, due to the enormous cost involved in instrumenting these volumes with sensor distances in the order of 10 m to 100 m. The achievable size for an acoustic detector could be several orders of magnitude greater with the same total number of sensors, as the sensor density is reduced to ~ 100 acoustic antennas per km^3 and thus by one order of magnitude. This larger volume would significantly enlarge the reaction propability for ν's within the detector for the falling ν spectrum at high energies and thus the energy range for neutrino telescopes to regions out of range of existing telescopes.

To study the feasibility of a future large scale acoustic UHE neutrino detector the *AMADEUS* (ANTARES Modules for Acoustic DEtection Under the Sea) [3,4] setup was integrated into the *ANTARES* (Astronomy with a Neutrino Telescope and Abyss environmental RESearch) neutrino telescope [5,6] located in the Mediterranean Sea at a water depth of 2500 m. The AMADEUS setup was developed and constructed at *ECAP* (Erlangen Centre for Astroparticle Physics) [7] which operates and maintains the system and analyses the recorded data.

ANTARES consists of 12 vertical detection lines, L 1 – L 12, plus one additional line, called Instrumentation Line (IL07). The latter houses instruments for monitoring the deep-sea environment. Each detection line holds 25 storeys. Each of these storeys consists of a titanium support structure, the *Optical Module Frame* (OMF), holding three *Optical Modules* [8] (OMs, photomultiplier tubes (PMTs) inside water-tight pressure-resistant glass spheres) and one *Local Control Module* (LCM). The LCM contains the off-shore electronics for data acquisition (DAQ) and a power supply within a cylindrical titanium container. Figure 1 shows the schematics of a standard ANTARES optical storey.

Figure 1: Schematics of an ANTARES optical storey. The three OMs are connected to the titanium cylinder in the centre of the scheme.

For the AMADEUS setup this storey design was carried over as closely as possible to minimise the influences of the resulting Acoustic Storeys on the ANTARES detector and obtain a fully integrated acoustic setup within the optical detector. Balancing the needs for acoustic detection structures and for a maximum size of the optical detector, a total of six storeys of the ANTARES detector is equipped with acoustical, instead of optical sensors. Due to the different data acquisition requirements in both cases it was possible to equip each Acoustic Storey with a total of six acoustic sensors compared to the three OMs in the optical detector. Thus, a total of 36 acoustic sensors is available to study the deep-sea acoustic environment. The Acoustic Storeys are located on two ANTARES lines, three storeys on L 12 and three storeys on the IL07. Figure 2 shows a schematic view of the ANTARES detector with the positions of the acoustic storeys highlighted. Their position on two lines provide the system with inter-sensor spacings ranging from 1 m to 340 m to study the correlation length of noise signals and directivity of the ambient noise. For the latter purpose, several sensors have different orientation, cf. “pointing down” in Figure 2.

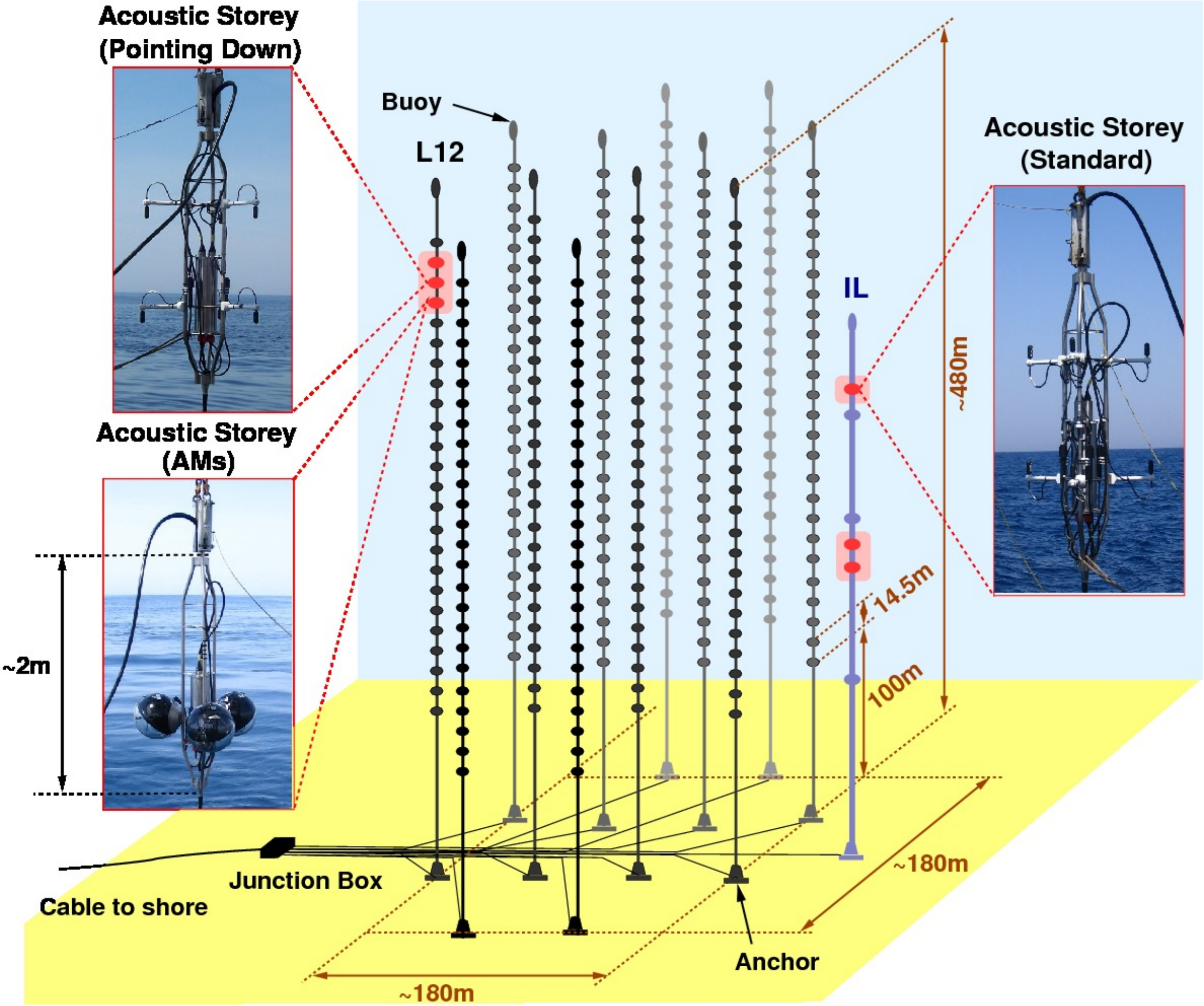

Figure 2: A schematic of the ANTARES detector. The six Acoustic Storeys are highlighted and their three different setups are shown. L 12 and IL denote Line 12 and the Instrumentation Line (IL07) holding the Acoustic Storeys, respectively.

The acoustic sensors used in AMADEUS are based on the piezo-electric effect. Thus, each sensor is equipped with a piezo ceramic. A voltage signal is generated between two piezo surfaces if it is exposed to an external force, for example a pressure wave. Due to the expected weak pressure pulse generated in particle interactions, the acoustic sensors are equipped with preamplifiers to generate measurable voltage signals. To study the feasibility of acoustic particle detection, the AMADEUS setup utilises three different types of acoustic sensors. The first type, commercial hydrophones referred to as "HTI" [9], are standard underwater acoustic sensors with a piezo cylinder moulded in polyurethan (PU). For the second type, custom-built hydrophones referred to as "LTI" [10], a design close to the HTI design was chosen. These hydrophones were developed at ECAP. The third type , referred to as Acoustic Modules (AMs), is a prototype design developed at ECAP consisting of two acoustic sensors glued to the inside of standard OM glass spheres. These acoustic sensors are similar to the LTI sensors (piezo ceramic and preamplifiers without PU coating). At the first (from bottom) Acoustic Storey on L 12 instead of hydrophones, the standard acoustic sensors, prototype Acoustic Modules (AMs) are installed.

Figure 3 shows a schematic of an Acoustic Storey equipped with hydrophones (left) and a photograph of an Acoustic Storey during deployment (right). Figure 4 shows the two non standard[1] Acoustic Storeys.

---

[1] Non standard in this context means: Not equipped with hydrophones orientated as shown in Figure 3.

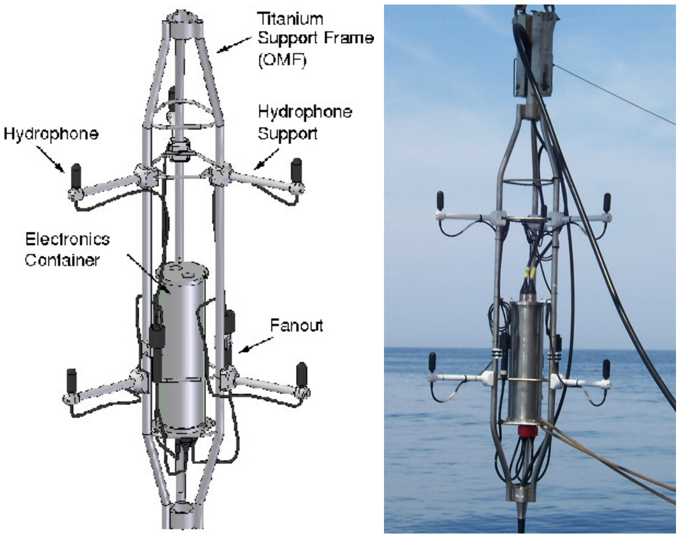

Figure 3: Drawing of a standard Acoustic Storey with hydrophones (left) and the photograph of a standard storey (storey 23 of L 12, holding LTI hydrophones) during deployment (right). This is the third Acoustic Storey on L 12.

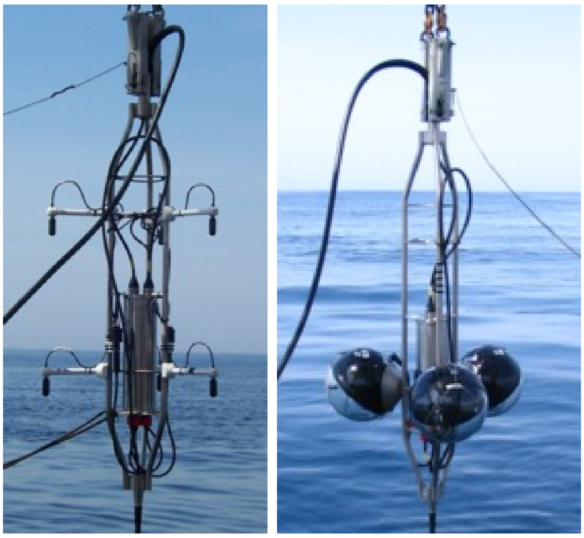

Figure 4: Photographs of the two non-standard storeys of the AMADEUS system during their deployment. The second Acoustic Storey (storey 22) on L 12 with HTI hydrophones pointing down (left) and the first Acoustic Storey (storey 21) equipped with Acoustic Modules (right).

The installation of the ANTARES neutrino telescope was completed on May 30th, 2008, together with the last components of the acoustic setup of AMADEUS.

The AMADEUS system has full detection capabilities – including time synchronisation on ns-precision and an operating mode suited for long-term continuous data acquisition – and is scalable to a larger number of Acoustic Storeys. Therefore, all the questions which are connected to the feasibility and performance of an acoustic detector can be pursued with AMADEUS in a setup similar to that of a possible future acoustic detector for UHE neutrinos, if of course much smaller.

The experiences gained with ANTARES can help to construct the next generation large volume deep-sea neutrino telescopes, for example KM3NeT [11]. One of those experiences was a water ingress into one of the LCM containers of L 12. This accidentally happened in December, 2008, and resulted in the loss of connection to more than half of the line, the acoustical part included. The successful recovery of L 12 in March, 2009, attested the feasibility of such operation and gave the opportunity to check the influence of the deep-sea environment to all parts of this line.

One key aspect of my work performed for this thesis is the recalibration of acoustic sensors. All utilised acoustic sensors are described in the following in more detail together with the performed calibration measurements. These calibration measurements are carried out according to different aspects arising from the successful operation of the AMADEUS setup. Further studies are performed to deepen the understanding of all parts of the detector to unfold its full potential and to ensure the observed high-performance for the future.

For the second key aspect of this thesis the development of new acoustic detection devices based on the gained experiences with the AM design is presented. This development towards a combination of acoustical and optical detection devices housed in one opto-acoustical module (OAM) is a promising option for future deep-sea neutrino telescopes and would combine two complementary detection methods by holding the advantages of its single components.

Part II

Acoustic signals in the laboratory

Chapter 1

Signal generation and recording

To perform the calibration measurements and tests of acoustic sensors indicated in the introduction, a set of equipment is available in our acoustic laboratory. It was already used for the development of sensors for the acoustic detection [10] in AMADEUS as well as its precursor studies [12–16] also performed at ECAP and is well suited for the desired measurements.

1.1 Water tank

There are two water tanks available for in-water measurements. The choice of the appropriate tank depends on the intent of the measurement. The first (small) tank is made of aluminium plates with a thickness of 8 mm. The dimensions of this tank are $150\times60\times60\,\mathrm{cm}^3$. The tank is covered by an aluminium frame which allows to adjust several devices at almost every position in the tank at a mm-precision. The tank is not completely filled to keep the possibility of moving the devices in the tank or to adjust the devices by hand without overflowing it. For the performed tests the water level is chosen to be 50 cm. The tank is filled with about 450 l of tap water. In this constellation a device placed in the middle of the tank is surrounded by at least 25 cm of water in every direction. In the simplest case this amounts to a travel time of surface reflections to about 380 µs compared to the travel time of the direct signal of about 170 µs for a distance of 25 cm between emitter and receiver. This is sufficient for the calibration measurements concerning the hydrophones, for description see Chapter 3 on page 23. For larger acoustic devices like the AMs, see description in Chapter 6 on page 43, the dimensions of the small tank are insufficient. The second (big) tank was especially designed for this type of sensors. It is made of painted steel in the dimensions $3.5\times2.0\times2.0\,\mathrm{m}^3$ and filled with about $14\,\mathrm{m}^3$ of tap water. This tank is equipped with a working platform and two work surfaces which can be slided on its top. On all three platforms material can be attached and adjusted. A crane above the tank allows for easy handling of large and heavy devices, as for example the AMs.

The work in the small tank is preferred as it has several advantages:

- Its dimensions allow for manual adjustment everywhere within the tank;
- The positioning frame is easy to handle and allows for fast changes in the setup;
- The short distances reduce the amount of necessary cables and material to a minimum;
- All required hardware devices can be placed on a table next to the tank or, if not current-carrying, on the framework itself.

1.2 Emitter

The emitters used for underwater sound generation in all following measurements are of the commercial transducer type "*F42D*" from *High Tech, Inc.* [9]. This transducer is a piezo based emitter moulded in polyurethan (PU) to protect the hollow piezo cylinder inside. As the acoustic impedance of PU is comparable to the acoustic impedance of water, this covering ensures the best transmission of the soundwave into the water. To generate a pressure signal (for a detailed description of the sound generation by piezo ceramics, see [17]), the transducer is stimulated by an external voltage provided by a waveform generator (see below). Figure 1.1 shows the sending characteristics[1] for this type of transducer.

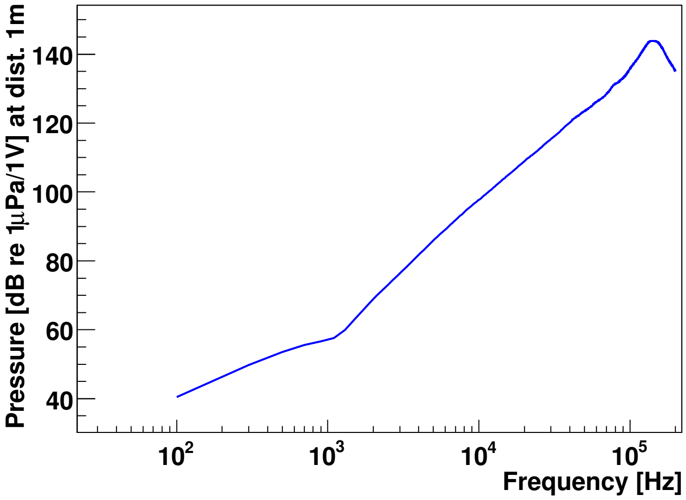

Figure 1.1: Sending characteristics of the acoustic emitter. The approximately ω^2 dependency in the main working region between 1 kHz and 100 kHz is observable in the almost linear curve progression (cf. text).

---

[1] According to the manufacturer.

Between 1 kHz and 100 kHz the logarithmically plotted sending characteristics is almost linear corresponding to a ω^2 dependency in the frequeny domain. According[2,3] to

$$\mathcal{F}\left(\frac{\partial^n}{\partial t^n}s(t)\right) = (i\omega)^n \tilde{s}(f) \tag{1.1}$$

and

$$\omega^2 \tilde{s}(f) = -(i\omega)^2 \tilde{s}(f) = \mathcal{F}\left(-\frac{\partial^2}{\partial t^2}s(t)\right) \tag{1.2}$$

this approximated ω^2 dependency of the signal $\tilde{s}(f)$ in the frequency domain corresponds to the negative second time derivative of the signal $s(t)$ in the time domain. The emitted pressure wave is therefore proportional to the second time derivative of the applied voltage signal:

$$p(t) \propto -\frac{\partial^2 U(t)}{\partial t^2}. \tag{1.3}$$

For signal generation this has to be taken into account by applying an inverted voltage signal corresponding to the twofold temporal integral of the required pressure signal. A signal with frequency components between 1 kHz and 100 kHz is sufficiently well described by this assumption, as the maximum deviation from this ω^2 dependency is $\approx 2\,\mathrm{dB}$ in this range.

The transducer is equipped with a BNC-type connector to connect it with a voltage or waveform generator.

1.3 Waveform generator

The waveform generator used throughout all measurements is a "*33220A 20 MHz Function/Arbitrary Waveform Generator*" from *Agilent Technologies* [19]. This waveform generator is able to generate a variety of predefined voltage signals with different settings and a maximum amplitude of 10 V at a sampling rate of 20 MHz. It is also capable of storing and generating custom designed signals presented in the next chapter. In addition to the voltage output, a second output provides a trigger signal which can be connected to an oscilloscope.

1.4 Signal recording

The data acquisition is performed in most cases by a digital storage oscilloscope, type "*waveRunner 6100*" from LeCroy Corp. [20]. This oscilloscope provides four input channels at a maximum sampling rate of 5 GS/s at 8 bit sampling. The employed sampling rate

---

[2] $\mathcal{F}(f)$ is the Fourier transform of f.

[3] For the proof of shown theorems and equations concerning Fourier transformation see [18].

usually ranges between 1 MS/s and 100 MS/s. Its internal memory allows for displaying the triggered signal with an appropriate surrounding time window of one million sampling points. The recorded voltage data are stored locally on the oscilloscope before they are moved to the ECAP computing network for further processing. This further processing is performed with custom developed software mainly based on C++ and ROOT [21].

Chapter 2

Calibration signals

For calibration purposes mainly two different signal types are used. These signals are emitted in short pulses to obtain a full featured calibration of the acoustic sensors. A time delay of 100 ms between pulses is chosen to ensure the total disappearance of any reflections of the emitted signal in the water tanks before the next pulse is emitted. The data acquisition is influenced by electromagnetic coupling and acoustic noise in the laboratory, therefore the finally stored emitted and received signal is an average over 250 pulses. This averaging is performed internally by the oscilloscope. Due to the dimensions of the tank the reflections from its surfaces can be separated from the primary signal without difficulties. In this chapter the calibration signals are characterised and their treatment is described.

2.1 Ramp signal

The first voltage signal is the so called “ramp” signal with an amplitude of $-4.0\,\mathrm{V}$ shown in Figure 2.1. This voltage pulse was designed to create a bipolar pressure pulse with a shape similar to an expected neutrino pulse. The expected emitted bipolar pressure pulse

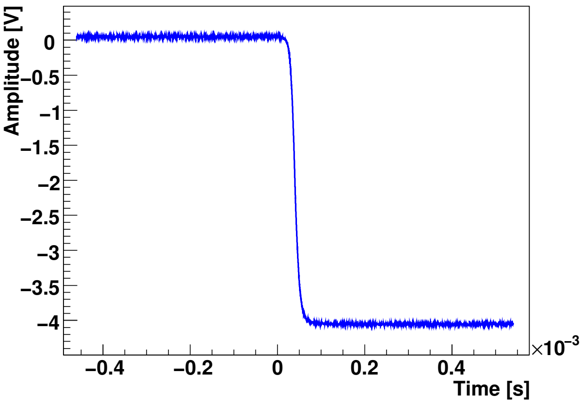

Figure 2.1: Voltage “ramp” signal emitted by the waveform generator.

is shown in Figure 2.2, according to the approximated negative second time derivative of the voltage signal. For the characterisation of this signal, its main feature, a compression followed by a rarefaction peak and its maximum and minimum can be used.

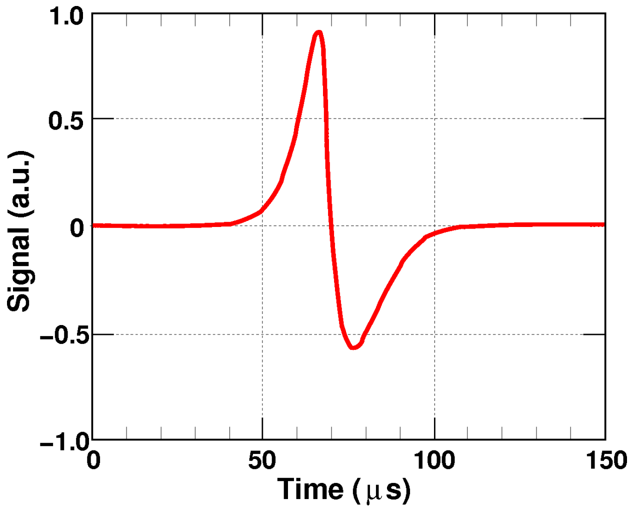

Figure 2.2: Emitted pressure signal (taken from [22]) when a transducer is stimulated by the voltage signal displayed in Figure 2.1.

The steps of analysing the recorded data by a dedicated program are as follows:

- Plot the whole data sample together with its inversion (see Figure 2.3). The inversion of the amplitudes simplifies the fit of the negative peak;
- Define a fit-region Δt_{FIT} according to:

$$\Delta t_{\mathrm{FIT}} = \frac{d_{\text{E-R}}}{c_{\mathrm{s,W}}} \pm t_{\mathrm{W}}, \tag{2.1}$$

  with
  $d_{\text{E-R}}$: Distance between emitter and receiver in the setup in m,
  $c_{\mathrm{s,W}}$: Speed of sound in water in m/s and
  t_{W}: Specified time window to take care of small variations concerning sound propagation and signal width;

- In this fit-region the maximum values of both samples, the original and its inversion (giving the maximum and the minimum of the data sample respectively), are determined. In a small interval of ± 2.5 µs around these maximum values, Gaussian functions are fitted to the data to obtain the exact extrema and the time of their occurrence (see Figure 2.4);
- The obtained parameters are saved to a summary file and can be processed by additional programs in the analysis chain.

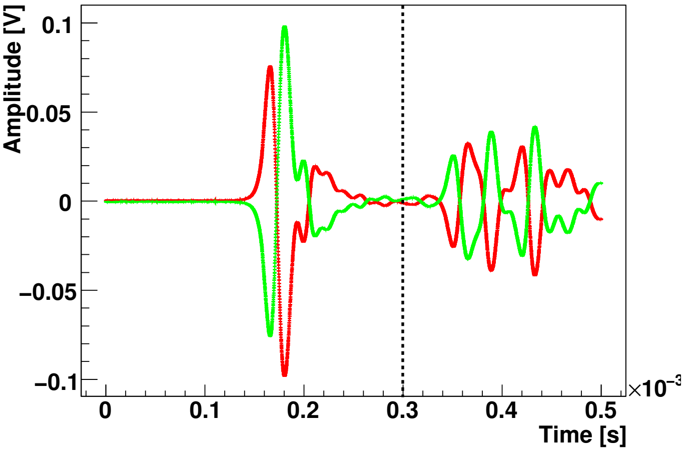

Figure 2.3: This figure shows a full data sample (red) and its inversion (green) for $d_{\text{E-R}}$= 25 cm. This sample was recorded with the commercial hydrophone HTI-016 described in Chapter 3. In this sample the signal is completely separated from any reflections as marked by the dashed black line, resulting in an almost undistorted signal.

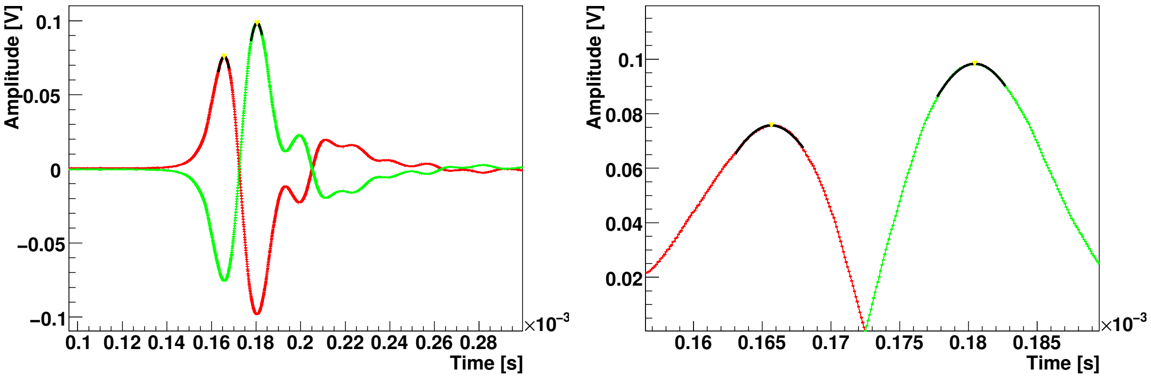

Figure 2.4: Left: Extract of the data sample shown in Figure 2.3 with cutted reflections. The Gaussian functions fitted to the data are shown as black curves. Right: In this zoom of the previous plot, the good approximation of the recorded data by the Gaussian functions is shown. The yellow triangles give the position of the fitted maximum and minimum.

Figure 2.5 shows the parameters used for the analysis of the received signals. The peak-to-peak amplitude A_{PP} is in most cases sufficient for comparison of different settings and setups, but as seen in Figure 2.4, the second (minimum) peak lies next to some resonant oscillations of the piezo sensor. These resonances can significantly alter the shape of the second peak for example depending on the incident angle, the piezo geometry or the sensor geometry. Therefore, the amplitude of the first peak A_{FP} is a reasonable option if A_{PP} is obviously distorted. Other parameters obtained in the fit process, for example the arrival time of the maximum or the distance between the extreme values, can be used to verify the correct receiver mounting (see Section 3.2) or to study the signal characteristics, the latter one being not in scope of this work.

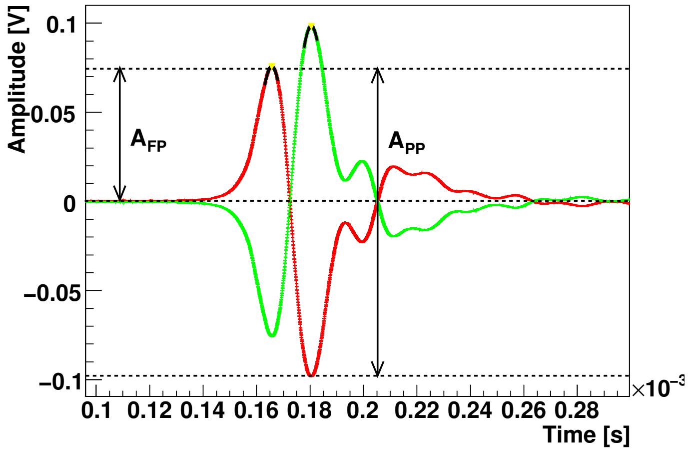

Figure 2.5: Figure 2.4 (left) with marked signal characteristics. The black dashed lines show the maximum, zero and minimum level of this sample. The arrows show how to obtain A_{FP} and A_{PP}.

2.2 Gaussian signal

The voltage signal sent to the emitter to gain a complete frequency spectrum of the acoustic receiver is a Gaussian voltage pulse of varying length. According to [10] and Equation 1.3, a Gaussian voltage pulse

$$f(t) = A \cdot e^{\left(-\frac{(t-t_0)}{2\sigma_t}\right)^2} \tag{2.2}$$

generates to a close approximation the following pressure signal

$$p(t) \approx -C \cdot \frac{\partial^2}{\partial t^2} f(t) = -C \cdot \left(1 - \frac{(t-t_0)^2}{2\sigma_t^2}\right) \cdot e^{\left(-\frac{(t-t_0)}{2\sigma_t}\right)^2}. \tag{2.3}$$

The result is a symmetrical tripolar signal. Its spectral shape exhibits a maximum at a frequency of

$$f_s = \frac{1}{\sqrt{2}\pi\sigma_t}, \tag{2.4}$$

where σ_t is the width of the Gaussian pulse in the time domain. By varying the length of the Gaussian pulse it is therefore possible to cover the whole range of interest for acoustic particle detection with sufficient emission power. This is not given for the ramp signal. A Gaussian signal with a resulting peak frequency of 80 kHz in the frequency domain is in most cases sufficient to achieve a full spectrum, cf. [10]. Most of the comparisons following in the next chapters are therefore performed with this signal, labelled "80 kHz Gaussian signal". The waveform generator produces Gaussian pulses with a total length of $10 \times \sigma_t$ in the time domain at 100 ms repetition rate. This fact in addition to Equation 2.4 leads to signals with a length of 112.6 µs, 56.3 µs and 28.15 µs corresponding to peak frequencies of 20 kHz, 40 kHz and 80 kHz, respectively. The corresponding voltage pulses are shown in Figure 2.6.

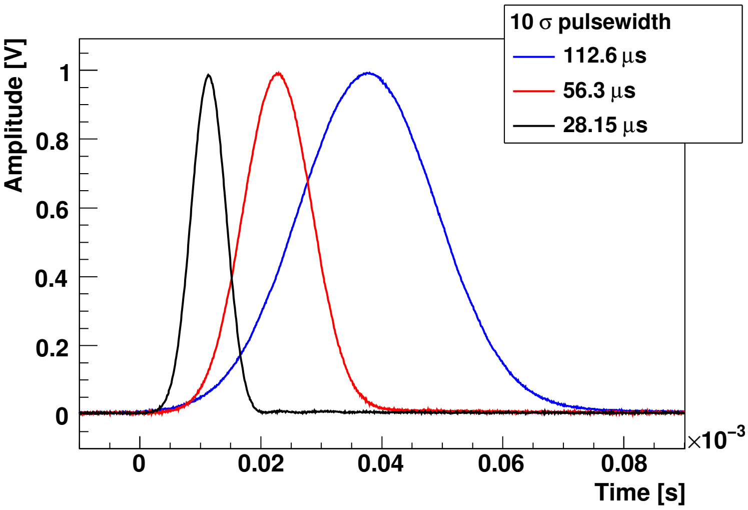

Figure 2.6: Extract of the voltage pulses generated by the waveform generator with pulsewidth shown in the legend.

The recorded signals are transformed via Fourier transformation to obtain their frequency spectrum using the *Fast Fourier Transform* (FFTW) algorithm [23]. The definition of the resulting power spectral density (PSD) used here follows the one in [10]. The SI unit for the PSD follows as $[\mathrm{PSD}] = 1\,\mathrm{V}/\sqrt{\mathrm{Hz}}$. The PSD is processed logarithmically to represent the characteristics of acoustic devices, typically varying over several orders of magnitude over the frequency spectrum. Therefore the unit of this relative PSD follows as $[\mathrm{rel.\ PSD}] = \mathrm{dB\ re}\ 1\,\mathrm{V}/\sqrt{\mathrm{Hz}}$. This representation simplifies the further processing as follows[1,2,3]:

The signal recorded by the receiver $R(t)$ is the convolution of the emitted voltage signal $E(t)$ with the transfer function $T(t)$ of the complete setup.

$$R(t) = (E * T)(t) = \int_{-\infty}^{\infty} E(\tau) \cdot T(t - \tau)\, d\tau. \tag{2.5}$$

---

[1] The following steps are described in more detail in [10].

[2] $\mathcal{F}(f)$ is the Fourier transform of f.

[3] For the proof of shown theorems and equations concerning Fourier transformation see [18].

Equation 2.5 has to be deconvoluted in order to gain the transfer function. In the time domain this is computational complex. By transferring the data in the frequency domain and applying the convolution theorem

$$\mathcal{F}(f * g) = \sqrt{2\pi}\left(\mathcal{F}(f) \cdot \mathcal{F}(g)\right), \tag{2.6}$$

Equation 2.5 transforms as follows:

$$\mathcal{R}(\omega) = \mathcal{E}(\omega) \cdot \mathcal{T}(\omega) \tag{2.7}$$

where

$$\mathcal{R}(\omega) = \mathcal{F}(R(t)), \tag{2.8}$$

$$\mathcal{E}(\omega) = \mathcal{F}(E(t)), \tag{2.9}$$

$$\mathcal{T}(\omega) = \mathcal{F}(T(t)). \tag{2.10}$$

The original convolution transforms to a simple multiplication of the corresponding Fourier transforms. The Fourier transform of the transfer spectrum $\mathcal{T}(\omega)$ is a complex function represented by:

$$\mathcal{T}(\omega) = A(\omega) \cdot e^{i\Phi(\omega)} \tag{2.11}$$

with the amplitude $A(\omega)$ and the phase $e^{i\Phi(\omega)}$. By applying a logarithm on both sides of Equation 2.7, the multiplication converts to a sum and the amplitude of the transfer function $\mathcal{T}(\omega)$ can simply be calculated by subtracting the emitted from the received spectrum (the different phases are always additive due to the properties of the exponential function).

$$\begin{aligned}\log\mathcal{R}(\omega) &= \log\left(\mathcal{E}(\omega) \cdot \mathcal{T}(\omega)\right) = \log\mathcal{E}(\omega) + \log\mathcal{T}(\omega)\\ &\Rightarrow \log\mathcal{T}(\omega) = \log\mathcal{R}(\omega) - \log\mathcal{E}(\omega).\end{aligned} \tag{2.12}$$

$\mathcal{T}(\omega)$ itself is a composition of different parts:

- An emitter part, as the emitted voltage signal has to be converted to a pressure signal;
- A translational part, as the pessure signal has to be propagated to the receiver;
- A receiver part, as the received pressure signal has to be converted back to a voltage signal;
- An electronics part resulting from the used electronics like oscilloscope, waveform generator, etc. which is negligible in this case.

All of these parts have to be determined independently for an absolute sensor calibration. In the following chapters the same emitter as well as almost the same calibration setup is used and only relative changes are investigated. Therefore it is not necessary to determine the emitter and translational part.

Part III

Hydrophones

Chapter 3

General description

The acoustic sensors referred to as hydrophones are the main active components of the AMADEUS setup, as 30 out of 36 sensors are of this type. This chapter describes these devices and the way they are treated in the laboratory. There are two types of hydrophones, the commercial hydrophones called HTI-0XX from *High Tech, Inc.* [9] and the custom-built hydrophones called LTI-1XX described in [10]. In both cases XX stands for a successive serial number. For a detailed description of the hydrophone performance and characteristics in their operation in the deep sea, see for example [22,24].

3.1 Layout

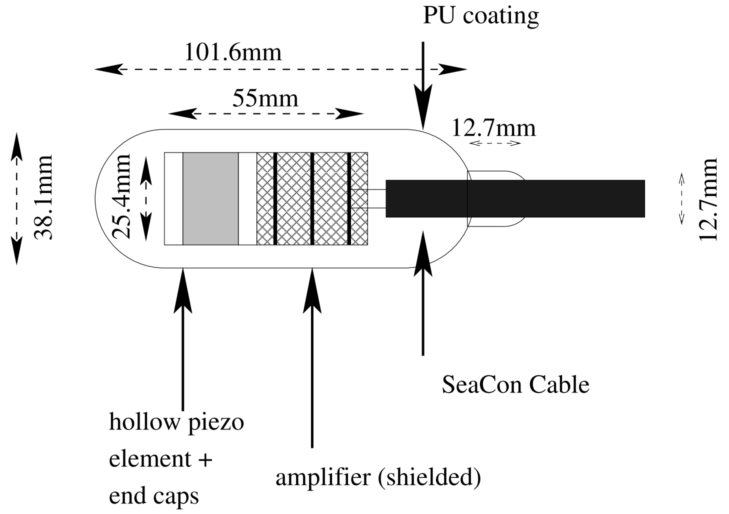

Figure 3.1: Schematic view of a custom-built LTI hydrophone [10].

Figure 3.1 shows the schematic view of a custom-built LTI hydrophone with its main parts and dimensions. The external dimensions of this design are identical to the commercial ones. This simplifies the mounting of the hydrophones in the laboratory as well as in the AMADEUS setup, as one setup can be used for all sensors. The hollow piezo cylinder with a radial polarisation and equipped with end caps is best suited for this type of sensor due to its geometry and therefore used in HTI as well as in LTI hydrophones. The piezo is connected to a shielded multistage amplifier which is further connected to a *SeaCon* cable [25]. To protect the piezo and its amplifier from the high pressure of the deep sea and from contact with sea-water, the hydrophone is moulded in polyurethan (PU). This coating additionally provides a matched coupling of an incident sonic wave to the sensor, as already described in Section 1.2.

3.2 Test setup

As the sensitivity of hydrophones is dependend both on the frequency and the angle of incident of the acoustic wave, a set of measurements with different directions of the incoming sonic wave and different signals, as described in Chapter 2, have to be performed. For these measurements both azimuth (φ) and polar (ϑ) angle, as defined in Figure 3.2, are adjusted to get a full 4π solid angle coverage.

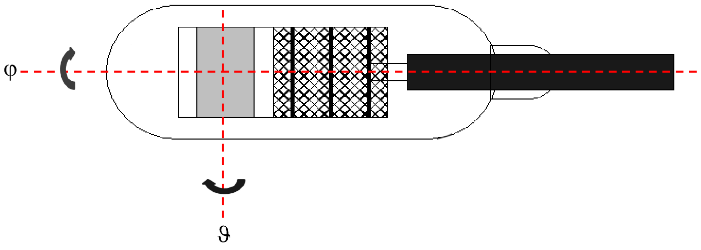

Figure 3.2: Definition of azimuth and polar angle. The red dashed line gives the rotational axis of the corresponding angle. $\varphi = 0°$ is defined through the raised writing "HTI" or the white bipolar pulse drawn onto the LTI hydrophones, see Section 3.2.1. $\vartheta = 0°$ is defined through the position of the hydrophone, when its front endcap faces the emitter (corresponding to sonic waves propagating from the left to the right in this picture). Therefore direct (perpendicular to the piezo cylinder axis) exposure to sonic waves occurs for $\vartheta = 90°$ and $\vartheta = 270°$.

The hydrophone design as shown in Figure 3.1 leads to the following expectations concerning the directivity of the hydrophones

- for variations of the ϑ angle:
  - For direct exposure to sonic waves, as defined in Figure 3.2, the sensitivity should reach its maximum as the piezo cylinder is directly stimulated parallel to its radial polarisation;

  - For sonic waves arriving laterally, the sensitivity depends on the resonance modes of the piezo cylinder. In fact it turns out that the hydrophones have comparable sensitivities in the directions around $\vartheta = 0°$ and $\vartheta = 90°/270°$;
  - Sonic waves arriving from the back ($\vartheta \approx 180°$) of the hydrophone should be shielded by the cable as well as the amplifier. The arising sensitivity should therefore reach its minimum for this direction;
  - In between the sensitivity is strongly influenced by the cylinder geometry and material and the resulting vibrational modes;

- for variations of the φ angle:
  - No significant influence of different directions should be visible due to the theoretically perfect rotational symmetry of the sensor along this axis. Small misalignments of the axis of the piezo ceramics with respect to the coating can lead to changes in the sensitivity when rotating around the "long" axis.

The hydrophones are equipped with a 4-pin (+ shield) connector (see Figure 3.3, left) providing two pins for DC power supply and two pins for differential signal readout. In the case of AMADEUS, two of these connectors can be connected to a *SeaCon* fanout "*AWQ-4/24*" (see Figure 3.3 with a fanout mounted on the transmission box further described in the text, right). The fanout itself with two sensors is connected to one of the three entries of the LCM of the Acoustic Storey which provides hydrophones with a supply voltage of 6 V and houses the DAQ hardware.

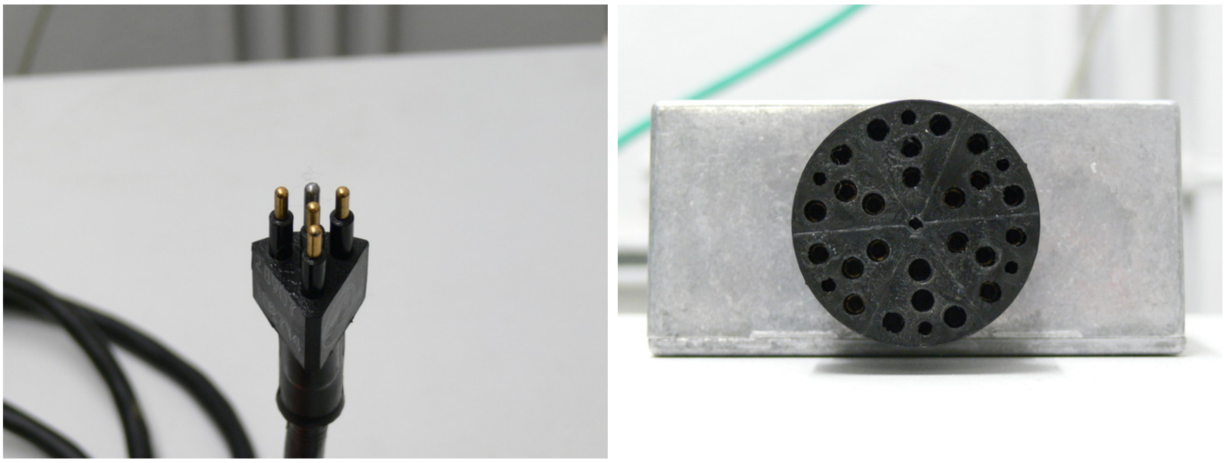

Figure 3.3: Hydrophone 4-pin connector (left). 4 pins correspond to the power supply and the differential signal, both +/-. The remaining argentic pin corresponds to an internal shield. This connector is plugged into one segment of the fanout shown right.

To simplify the measurements in the laboratory, instead of an LCM, a custom designed aluminium box is used to power and readout the hydrophones. This box is shown in Figure 3.4 (the front view is already given in Figure 3.3, right) and consists on the sensor side of a spare fanout connected to six differential signal connectors (BNC-type) and one combined voltage feed. With this box it is thus possible to operate six hydrophones simultaneously. In general only one hydrophone is connected to this box and the sensors are calibrated consecutively.

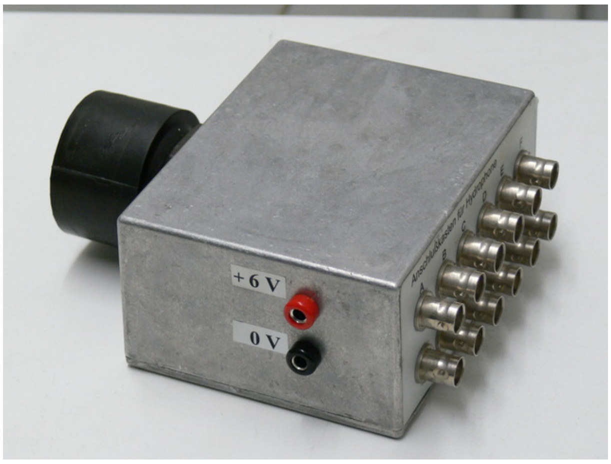

Figure 3.4: Box to supply the hydrophones with the required 6 V supply voltage and to readout their differential signals.

3.2.1 Azimuthal (φ) mounting

The hydrophone has to be placed in the water tank according to the scheme[1] in Figure 3.5 to calibrate it in the azimuthal plane. The azimuthal rotational axis of the hydrophone is aligned parallel to the one of the emitter at a distance of 25 cm. Due to the dimensions of the small tank used for this measurements both the emitter as well as the hydrophone are surrounded by at least 25 cm of water without obstacles in every direction. The hydrophone is clamped with its cable to a rod. As reference point, defining the incident angle $\varphi = 0°$, the raised writing "HTI" or the white bipolar pulse drawn onto the LTI hydrophones is chosen (see Figure 3.6). Emitter and hydrophone height are chosen to place the centre of both piezo elements at the same height and at the centre of the water level. By consecutively emitting the calibration signals and afterwards turning the hydrophone by 15° with the help of a scaled disc, the complete azimuthal calibration is performed for a full cycle of 360°.

---

[1] The schematics in Figure 3.5 and Figure 3.7 are taken from [12].

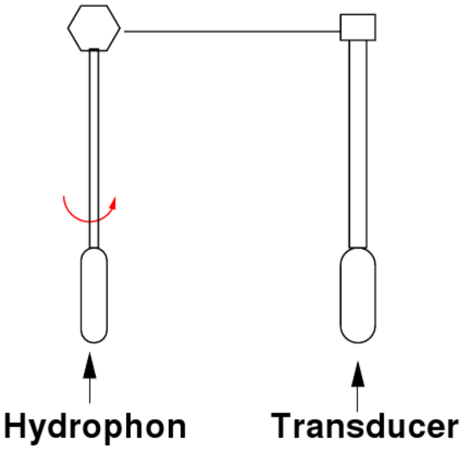

Figure 3.5: Schematics of the azimuthal mounting of the hydrophones. The red arrow gives the turning direction of the hydrophone.

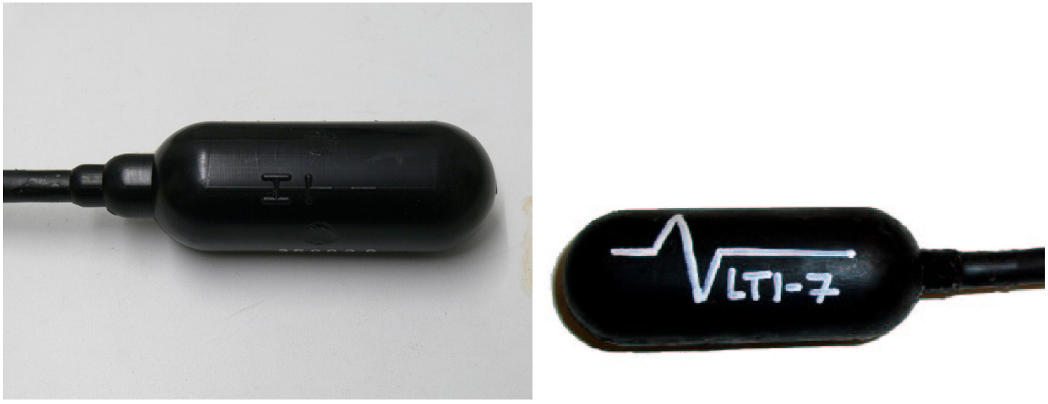

Figure 3.6: These pictures show HTI-030 (left) and LTI-107 (right). The raised writing and the white bipolar pulse are taken as reference for the adjustment.

3.2.2 Polar (ϑ) mounting

The principle of the polar mounting is shown in Figure 3.7 (left), also defining the reference for $\vartheta = 0°$. For reasons described in the following chapter, this setup is expanded by including (see Figure 3.7, right) the hydrophone support structure used in the Acoustic Storeys which is made of polyethylene terephthalate (PETP). This structure is used to mount the hydrophones to the OMF, see Figure 3.8. The positioning of the hydrophone is similar as for the azimuthal mounting. The emitter stays at its position already described before with a distance of 25 cm to the piezo centre. The $\varphi = 0°$ position is facing the water surface corresponding to the direction towards the centre of the OMF in AMADEUS. In AMADEUS this is also used for the orientation of the hydrophone. The hydrophone height is chosen to place the centre of the piezo element at the level of the one of the emitter. The rotational axis has to be aligned through the centre of the piezo cylinder in order to minimise the effects of different sound propagation distances. However, this cannot be completely avoided due to the finite dimensions of the piezo cylinder and the asymmetry of the piezo cylinder when rotated in this way. Ramp signals are emitted for a whole turn, that means 360° with a stepsize of 15°, to ensure a correct mounting of the hydrophone. The data are analysed according to Section 2.1 and the arrival time of the maximum is obtained. The speed of sound in water in the laboratory is calculated to $c_{\mathrm{s,W}} \approx 1470\,\mathrm{m/s}$ using the *UNESCO algorithm* [26]. Figure 3.9 shows an example of recorded signal arrival times for HTI-016.

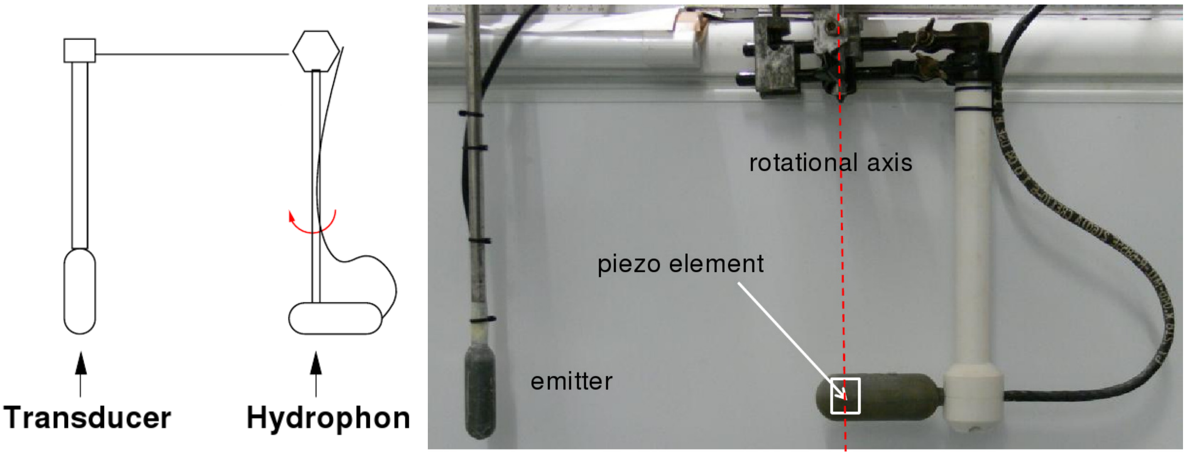

Figure 3.7: Left: Schematics of the polar mounting of the hydrophones. The red arrow gives the turning direction of the hydrophone. Right: Calibration setup in the polar plane. The red dashed line shows the rotational axis for the polar angle, the white square shows the approximate position of the piezo cylinder.

Figure 3.8: Photograph of an OMF supporting hydrophones. The white hydrophone supports are the same as used in the hydrophone calibration.

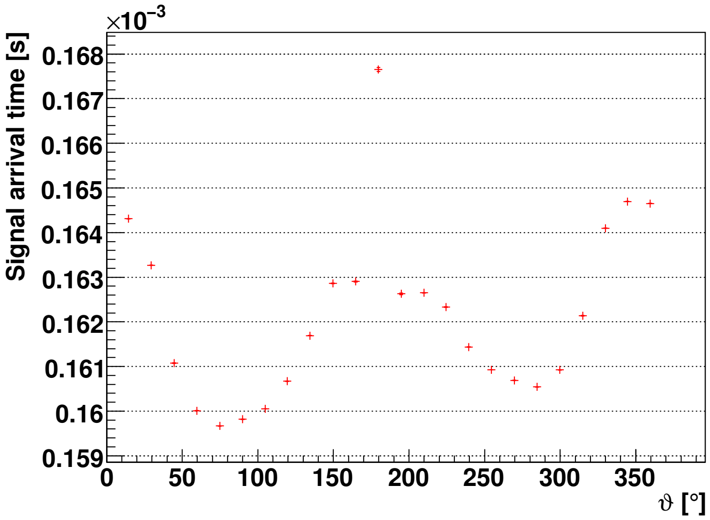

Figure 3.9: Verification of the correct polar mounting by comparison of signal arrival times. The red crosses show the obtained signal arrival times for a calibration of HTI-016 for a stepsize of 15°. The observed difference of about 0.87 µs corresponding to about 1.28 mm for $\vartheta = 70°$ and $\vartheta = 285°$ is an indication for a not fully aligned piezo ceramic. The plot is further described in the text.

This plot can be described as follows:

- For $\vartheta \leq 165°$ and $\vartheta \geq 195°$ the data progression shows an almost sinusoidal behaviour with minimum values around 90° and 270°. This progression is explainable due to the projection of the geometrical shape of the cylinder during rotation. The differences in the arrival times are of the order of 5 µs, corresponding to about 7.4 mm. This difference is negligible for calibration measurements as compared to the 25 cm distance;
- For $\vartheta = 180°$ the arrival time of the signal is obvious separated from all other arrival times. This behaviour is explainable through the fact that the sound wave is shielded by the interior of the hydrophone as well as through the support structure. This causes a small time shift as well as distortions in the signal rendering it difficult to define the arrival time;
- All together the difference between maximum and minimum is about 6 µs, corresponding to about 9 mm. With respect to the difficult situation for $\vartheta = 180°$, the hydrophone as shown in Figure 3.9 is mounted correctly to a sufficient accuracy.

Again, by consecutively emitting and recording of the calibration signals and afterwards turning the hydrophone by 15° with the help of a scaled disc, the complete polar calibration is performed for 180° or 360° intervals, if necessary.

Chapter 4

Calibration under different aspects

In this chapter no full hydrophone calibration is performed. Instead, the sensitivity of a hydrophone never exposed to the deep sea, HTI-016, is examined under aspects arising from the successful operation of the AMADEUS setup. The data recorded since 5th of December, 2007, for the IL07 and since 5th of June, 2008, for L 12 give a sufficient amount of data to perform reliable noise studies. The measured data differ from the data expected from the hydrophone calibrations[1] performed prior to deployment and simulations of the ambient noise characteristics in the deep sea. Therefore, the attempt is made to explain the observed deviation in the data by differences in the setup used for the calibration procedure and in the final data taking.

4.1 Differences between data and simulation

The AMADEUS setup in its final design, consisting of 36 acoustic sensors, is equipped with a variety of different sensors in different distances and orientations (in the case of Storey 22 on L 12) to each other. This allows for detailed noise studies in the deep sea, for example correlation length of noise signals and directivity of the ambient noise. In the following, Storey 6 on IL07 (pointing upwards[2]) is compared to Storey 22 on L 12 (pointing downwards[3]), both holding HTI sensors. Storey 22 is the only downward pointing storey whereas Storey 6 is chosen as it is placed at a similar level above the seabed (about 305 m for Storey 6 compared to $\sim$ 395 m for Storey 22). This fact render these storeys predestined for the influence of the hydrophone directivity to ambient noise which is assumed to be mainly generated on the sea surface.

Figure 4.1 shows the simulated[4] sensitivities for these storeys for an isotropic generated

---

[1] All sensors where calibrated before the integration into AMADEUS.

[2] "Upwards" means the piezo element facing the sea surface whereas the cable faces the seabed.

[3] "Downwards" means the piezo element facing the sea bed whereas the cable faces the sea surface.

[4] These simulations were performed by Dr. J. Hößl from ECAP.

noise and surface generated noise. These simulations are based on the calibrations performed in the laboratory prior to installation. In the latter case an obvious difference of about 3 dB ± 1 dB occurs which should be visible in the real noise data, too. The difference in the sensitivities for isotropic generated noise of ∼ 1 dB is a good approximation of the calibration uncertainty as the sensitivities should be almost equal in this case.

The data obtained with both storeys in fact show no significant difference in the obtained spectra as can be seen in Figure 4.2.

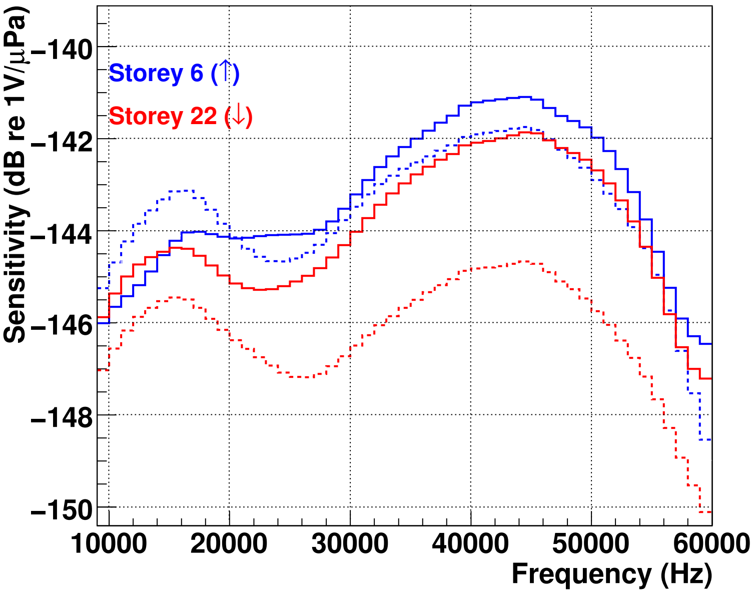

Figure 4.1: Expected sensitivity for differently orientated storeys. The solid lines show the sensitivities for a simulated isotropic noise distribution and the dashed lines show the sensitivities for simulated surface generated noise for both storeys. An almost constant difference of 3 dB occurs in the latter case.

An attempt to understand this discrepancy is to examine the differences in the calibration setup and in the data taking conditions in the deep sea. Two main changes can be pointed out:

- The calibrations prior to deployment were performed without the support structures of these hydrophones. In the deep sea the hydrophones are fixed by these structures;
- In the laboratory the hydrophones are directly connected to an oscilloscope whereas the data acquisition in the deep sea is performed via an AcouADC board[5] for signal filtering, amplification and data handling.

In the next sections both changes are discussed in more detail.

---

[5] For detailed informations on the AcouADC board, see [22].

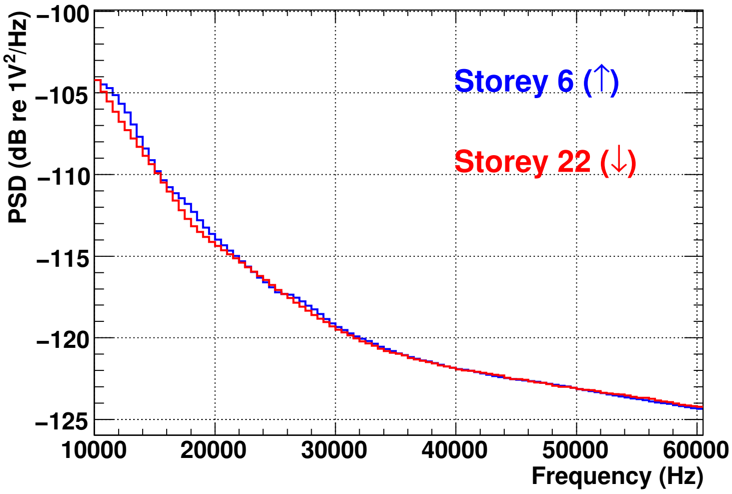

Figure 4.2: Median PSD for differently orientated storeys. The obtained data for a period of one month show no significant difference.

4.2 Support structure

The support structures (Figure 3.7 (right) shows a hydrophone already mounted to the support structure) used for AMADEUS were designed to clamp the hydrophone cables and thereby fixing the hydrophone at its position. Their length of 35 cm was chosen to match the dimensions of an Acoustical Storey with the dimensions of an optical one. The rear view of a support structure with attached hydrophone is shown in Figure 4.3. The support structure obviously completely covers the hydrophone in that direction, which should strengthen the shielding for $150° \lesssim \vartheta \lesssim 210°$.

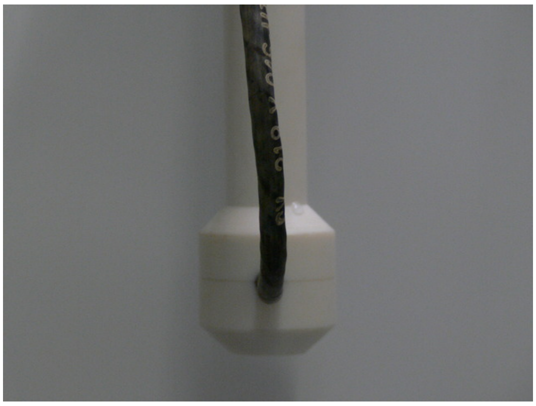

Figure 4.3: Rear view of a hydrophone support structure obviously covering the attached hydrophone.

The speed of sound in PETP ranges between 1300 m/s and 1400 m/s depending on its composition. This difference in the sound velocities in water and PETP of about 70 m/s to 170 m/s might lead to a lensing effect strengthening the signals for the “downward” direction, although not by much. Possible internal interference could also strengthen the signals.

The hydrophone, HTI-016, is mounted according to Figure 3.7 to test these assumptions. The ramp signal is emitted and the hydrophone data are recorded for the full range of 360° in steps of 15°. Figure 4.4 shows the comparison for a hydrophone mounted without support structure and calibrated prior to deployment and HTI-016 with support structure. The observed directivity is identical for both measurements. The signal attenuation's up to $\sim 60\%$ occur for ϑ between 135° and 165° (66% without and 56% with the support structure) and maximum sensitivities occur for $\vartheta = 0°$ and $\vartheta = 90°$. Due to the sensor symmetry values for $\vartheta = 180° + \mathrm{X}$ are almost identical to the ones for $\vartheta = 180° - \mathrm{X}$ (where X denotes an arbitrary angle). Table 4.1 shows the comparison of the obtained sensitivities. The comparison of $\mathrm{R}_{\mathrm{without}}(\vartheta)$ and $\mathrm{R}_{\mathrm{with}}(\vartheta)$ shows only a variation in the ratio between 0.975 and 1.184. This variation is no explanation for the deviation to the simulated data of $\sim 3\,\mathrm{dB}$, corresponding to a ratio of 1.4. Thus no significant effect arises from the support structure.

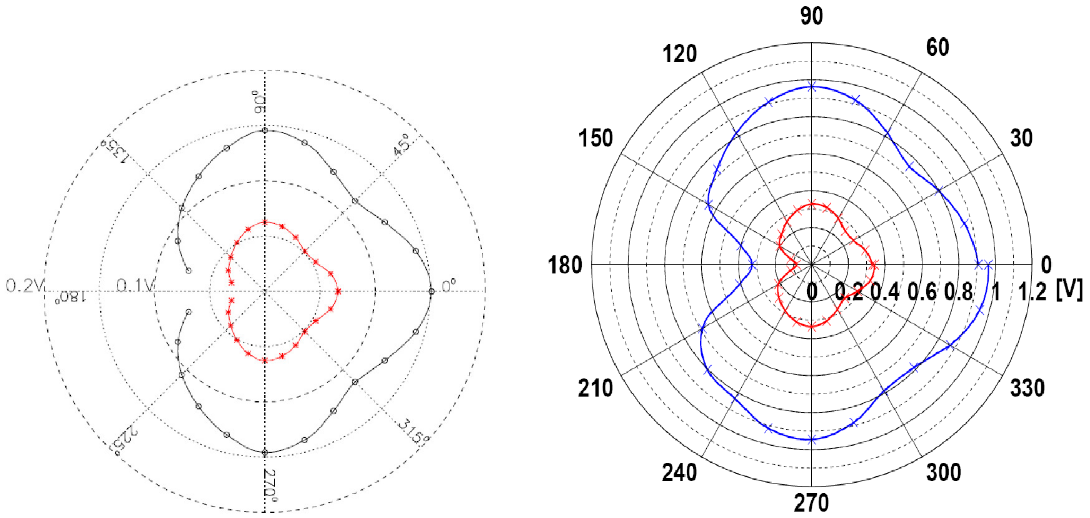

Figure 4.4: Directivity comparison for hydrophones calibrated with (right) and without (left, [10]) the support structure. The curves show A_{FP} (first peak amplitude; red) and A_{PP} (peak-to-peak amplitude; black and blue respectively). The plots are further described in the text. The connecting lines are only to guide the eye.

ϑ [°]	$\mathbf{A_{without}}(\vartheta)$ [V]	$\mathbf{A_{with}}(\vartheta)$ [V]	$\mathbf{R_{without}}(\vartheta)$	$\mathbf{R_{with}}(\vartheta)$	$\frac{\mathbf{R_{without}}(\vartheta)}{\mathbf{R_{with}}(\vartheta)}$
90	0.143	0.964	1	1	1
105	0.136	0.900	0.951	0.934	1.018
120	0.121	0.814	0.846	0.844	1.007
135	0.107	0.729	0.748	0.756	0.992
150	0.093	0.643	0.650	0.667	0.975
165	0.071	0.407	0.497	0.422	1.184

Table 4.1: Influence of the hydrophone support structure on the hydrophone sensitivity. $\mathrm{A_{without}}(\vartheta)$ and $\mathrm{A_{with}}(\vartheta)$ represent $\mathrm{A_{PP}}$ as a function of ϑ for the measurement without and with the support structure, respectively. The absolute amplitudes shown in volt are not comparable as these values were obtained in different measurements. For a comparison the ratios $\mathrm{R_{without}}(\vartheta)$ and $\mathrm{R_{with}}(\vartheta)$, given as the quotient $\mathrm{A_{PP}}(\vartheta)/\mathrm{A_{PP}}(\vartheta = 90°)$ for both measurements respectively, are calculated.

4.3 AcouADC board

The differences between the readout via oscilloscope and via AcouADC board are:

- The different impedance of both devices: The oscilloscope has a high input impedance whereas the AcouADC board was designed with a relatively low input impedance of several $100\,\Omega$ for noise reduction;
- The data processing in the analogue part of the AcouADC board:
  - A bandpass filter applied to the signal;
  - Two amplifier stages for post amplification.

The AcouADC board was tested extensively concerning the signal performance. Therefore no significant influence is expected from the board. To ensure this , especially as the hydrophones have not been fully calibrated with the AcouADC boards, the same set of measurements is performed as in the previous section. In the measurements the signal of the hydrophone is fed once through the AcouADC board and in parallel through the oscilloscope. Figure 4.5 shows the two schematic measurement chains. The direct measurement is identical to the measurement concerning the support structure. The measurement via the AcouADC board is performed with the hydrophone directly connected to the board. The board is then readout by the oscilloscope at the end of the analogue part. For the comparison of signals from direct measurement and measurement via AcouADC board, see Figure 4.6. The latter signal (red) arrives about $13\,\mu$s after the former signal and its amplitude is slightly smaller. This is a known and well understood effect of the applied

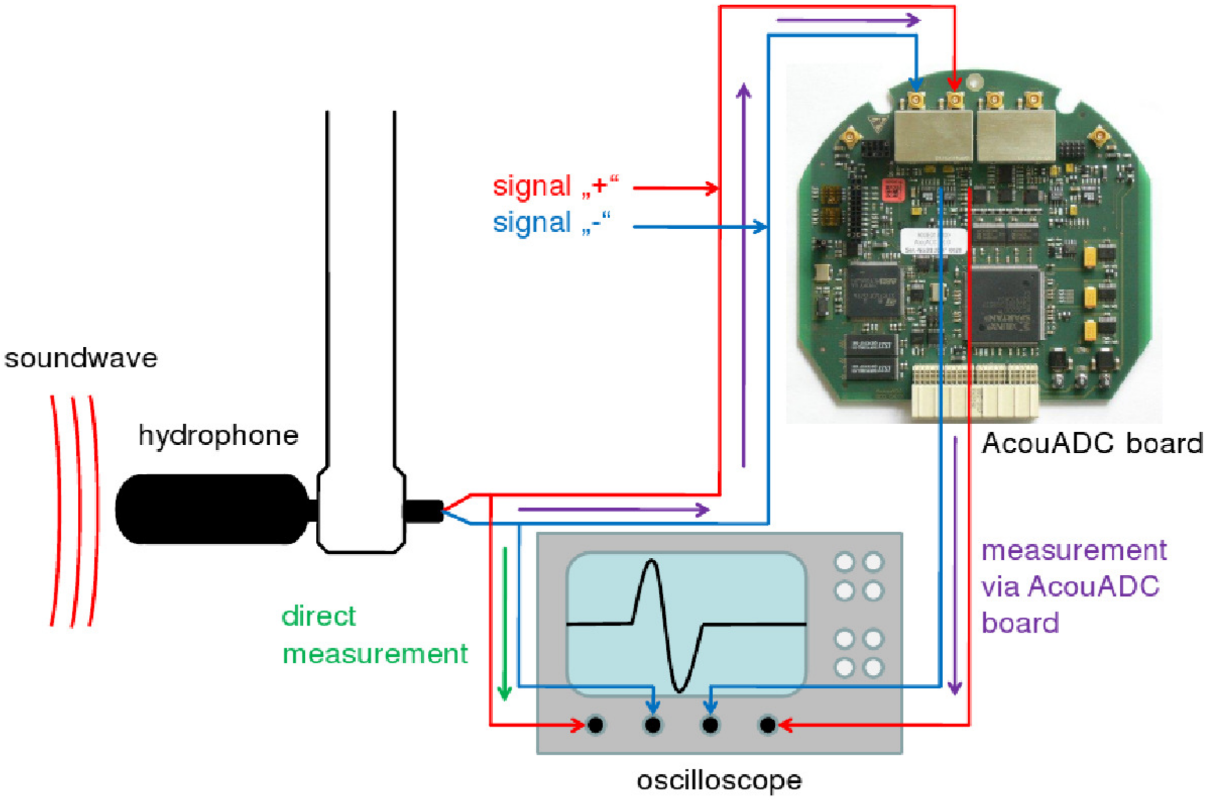

Figure 4.5: Schematic of the setup including the AcouADC board. The two different measurement chains are shown as green (direct measurement) and violet (measurement via AcouADC board) arrows.

bandpass filter [22]. Together with Figure 4.7, showing the obtained directivity for both cases, no influence on the directivity can be observed.

The results of the measurements performed in the last two sections can not explain the deviation of simulated and real data. Therefore further investigations have to be performed to understand this certainty.

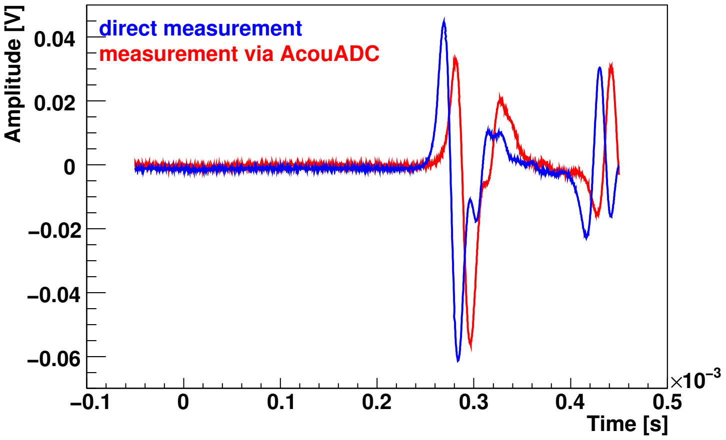

Figure 4.6: Comparison of recorded bipolar signals with and without the AcouADC board (with a gain of 1.00) for $\vartheta = 90°$. The time shift of the red signal is generated by the analogue signal path within the AcouADC board.

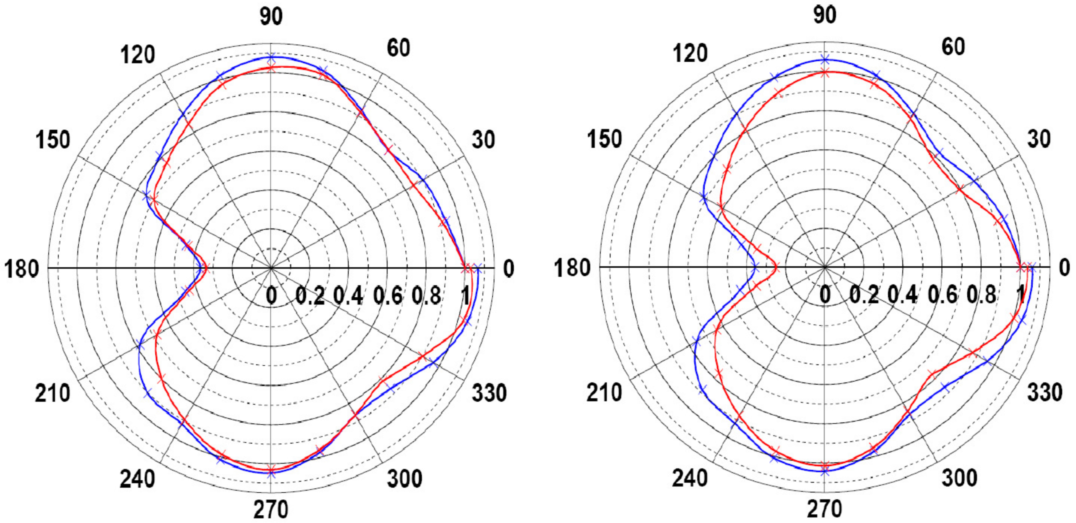

Figure 4.7: Directivity comparison for hydrophones for direct measurement (right) and measurement via AcouADC board (left). The curves show A_{FP} (first peak amplitude; red) and A_{PP} (peak-to-peak amplitude; blue). In both cases the amplitude values are normalised to one at $\vartheta = 0°$. No significant influence is observed applying an uncertainty of the measurements (defined through the discontinuity of the amplitude values for $\vartheta = 0°$ and $\vartheta = 360°$) of about 6%. The lines are only to guide the eye.

Chapter 5

Hydrophone sensitivities

The recovery of Line 12 (L 12) in March, 2009, gave the unique opportunity to test all acoustic sensors on this structure, repair (in case of the AMs) or exchange (in case of the hydrophones) inoperabel or malfunctional acoustic sensors. In addition, the sensors were recalibrated after their ~ 300 days exposure to the high pressure and the deep-sea environment. In the following sections, the recalibrated data of the hydrophones are compared to the data obtained prior to deployment in order to determine any significant influence of the deep-sea environment on the sensor performance.

The hydrophones were sent to Erlangen after unmounting them from the OMFs, but still mounted to their support structure; they are kept on this support structure for the calibrations as the influence of this structure on the calibration is negligible, as described in Section 4.2. In addition a hydrophone never exposed to the deep sea, HTI-016, is recalibrated to compare both calibrations unbiased from environmental influences.

5.1 HTI hydrophones

The functionality test of the seven HTI hydrophones installed on L 12 (HTI-007, HTI-011, HTI-013, HTI-025, HTI-026, HTI-027, HTI-029) showed a new inoperabel hydrophone, HTI-013. This sensor worked perfectly until the loss of connection to L 12, which was due to a powering problem. Therefore, a voltage peak during the loss or the recovery with its depressurisation is assumed as the cause of this damage. The other sensors including HTI-016 are calibrated according to Section 2.2 to obtain their spectral and directional sensitivity. Only the calibration for the polar angle is performed as the azimuthal calibration requires the dismounting of the support structure which is not preferable. In addition, the uniformity ($\sim 15\%$) in azimuthal direction shown in [10] and in the calibration of the spare hydrophones not yet mounted to their support structures, see Section 5.3, justifies this approach. The differences resulting from the exposure to the deep-sea environment (for example caused by ageing of the PU coating or the disappearance of small air bubbles inside this coating) should be more pronounced in the calibration for the polar angle as well.

The data obtained with the hydrophones are treated, in addition to Section 2.2, by cutting reflections resulting from the dimensions of the small tank. The cut is performed according to a travel time estimation for the first reflections and by additional zero-padding (restoring the original sample length by adding zeros). In Figure 5.1 the effect of this cut on the PSD is shown. The oscillations in the former PSD are mainly caused by the signal cut with a non-zero amplitude at the end of the data sample (for a detailed description of this effect, see [10]). Removing the reflections leads to the smoothed latter PSD. This PSD plot depicts the limits of the performed calibration:

- For frequencies below 10 kHz, the emitter strength gets unsatisfactory for calibration purposes (see Figure 1.1);
- The emitter-receiver distance of 25 cm (constituting the minimum wavelength for a homogeneous sound field) only allows for reasonable calibration measurements above a frequency of 6 kHz, representing a wavelength of about 25 cm;
- For frequencies above 80-90 kHz the hydrophone sensitivity is largely reduced.

The resulting sensitivities for the different polar angles can be compared one by one to the ones obtained prior to deployment. To compare the sensitivities in a more rational way, it is useful to define a mean sensitivity[1]. This is done by giving each ϑ angle a weight proportional to the corresponding differential solid angle, as defined in Figure 5.2, with the assumption of constant sensitivity in azimuthal direction, which is confirmed by the results obtained in Section 5.3. Therefore the mean sensitivity becomes

$$\overline{S(\omega)} = \frac{1}{A}\int_0^\pi S(\vartheta,\omega)\frac{\partial A}{\partial\vartheta}d\vartheta = \frac{1}{4\pi}\int_0^\pi 2\pi\sin(\vartheta)S(\vartheta,\omega)d\vartheta \tag{5.1}$$

corresponding [10] to

$$\overline{S(\omega)} = \frac{1}{4\pi}\left(\sum_{k=1}^{n-1} 4\pi\sin(k\Delta\vartheta)\sin\left(\frac{\Delta\vartheta}{2}\right)S_k(\omega) + 2\pi\left(1-\cos\left(\frac{\Delta\vartheta}{2}\right)\right)(S_0(\omega)+S_n(\omega))\right) \tag{5.2}$$

with

$$S_k(\omega) = S(k\Delta\vartheta,\omega); \tag{5.3}$$

for a discrete distribution in ϑ, given in these measurements[2].

The results obtained for HTI-027 are shown in Figure 5.3. The effect of the averaging process is obvious as well as the directivity of the spectra. The frequency dependent difference of the mean sensitivities prior to deployment and after the recovery for HTI-027 is shown in Figure 5.4 together with the distribution of the data. The distributions for the other hydrophones are given in Appendix A.1. The mean value of the distribution indicates

---

[1] The definition of the mean sensitivity used here follows the one in [10].

[2] $\Delta\vartheta = \frac{\pi}{n}$, with the number of performed steps n.

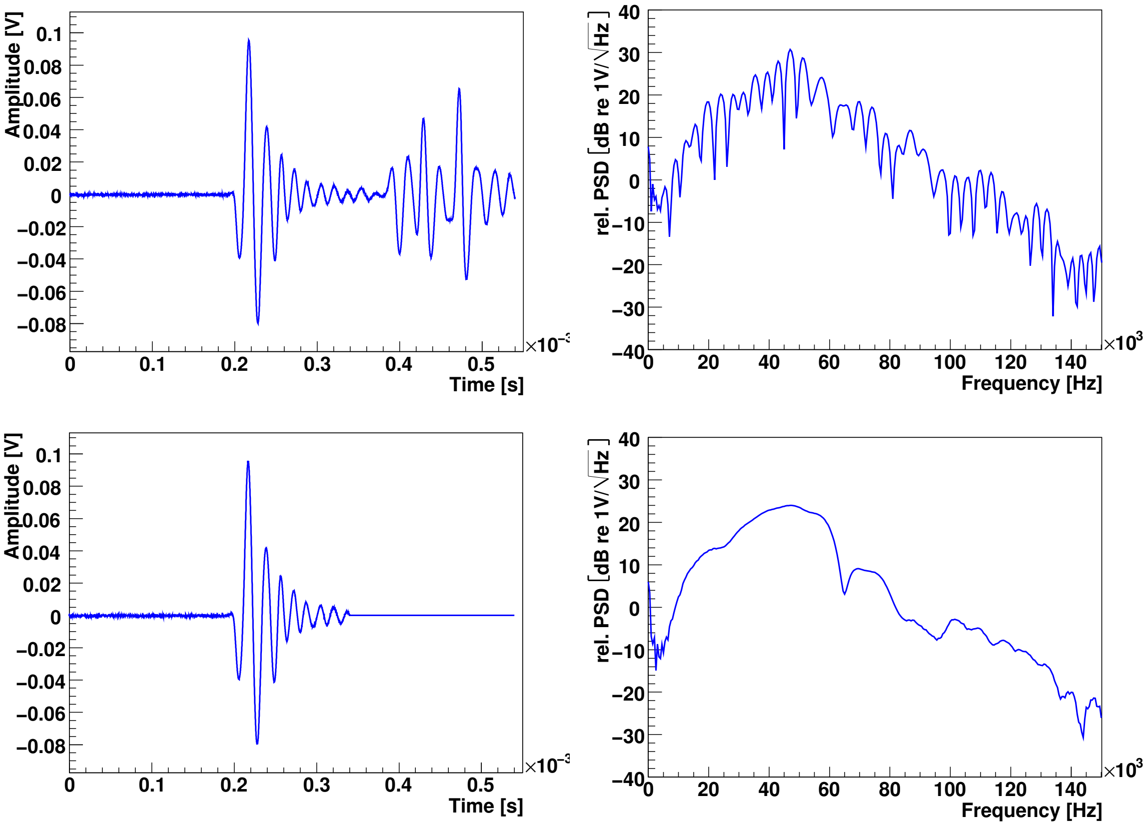

Figure 5.1: Calibration signal recorded for HTI-025 (top left) with $\vartheta = 0^\circ$ and the 80 kHz Gaussian signal. In this case the received signal is clearly distinguishable from the reflections arising through the dimension of the small water tank. The bottom left plot shows the same signal with applied cut to the signal. This cut is applied according to a travel time estimate for the first reflections in the small water tank. The resulting PSD in the former case (top right) is obviously dominated by oscillations caused by the signal cut at the end of the data sample. The resulting PSD in the latter case (bottom right) shows a smooth curve progression and is further described in the text.

a decrease of sensitivity of about 2.24 dB with a RMS of 1.51 dB. Figure 5.5 shows the results for HTI-016 to study the systematics of the measurements. In this case the mean sensitivity is increased by about 1.42 dB with a RMS of 0.94 dB. Both values determine the extreme values in the distribution of the data obtained for all HTI hydrophones (see Table 5.1). The accuracy of the performed measurements itself is of the order ± 30% or ± 2.5 dB, rendering the results for the HTI hydrophones consistent with no variation due to the exposure to the deep sea.

These hydrophones where redeployed and are fully operational, except for HTI-013 (defective) and HTI-007 (malfunctional) exchanged by HTI-031 and HTI-033 respectively.

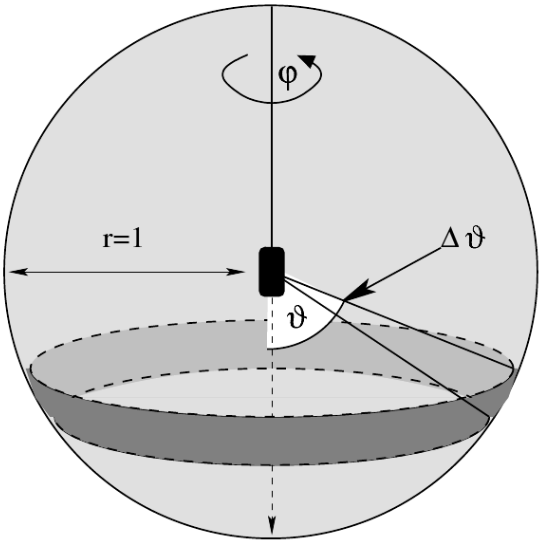

Figure 5.2: Schematic for ϑ-averaged calibration. The averaging occurs along the polar angle ϑ in steps of $\Delta\vartheta$. Each slice is weighted by the surface area of the unit sphere between $\vartheta - \frac{\Delta\vartheta}{2}$ and $\vartheta + \frac{\Delta\vartheta}{2}$.

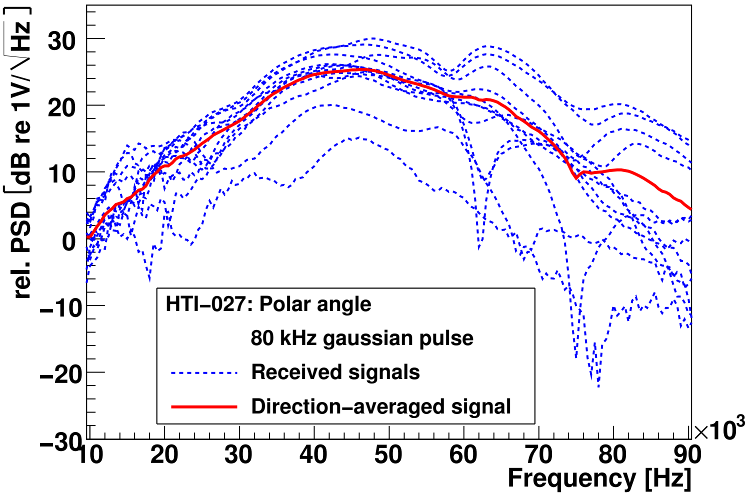

Figure 5.3: Polar sensitivity for HTI-027. The blue curves show the sensitivities for the different polar angles. The red curve shows the mean sensitivity described in the text.

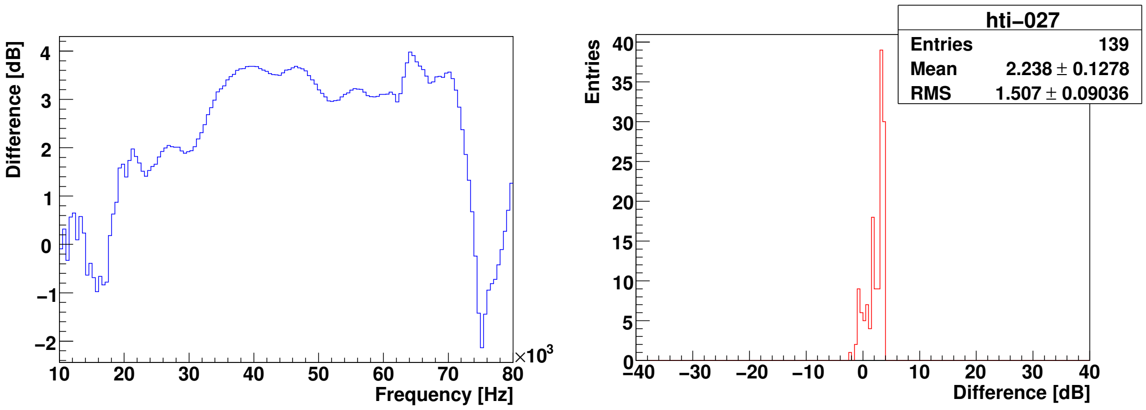

Figure 5.4: Frequency dependent difference of the mean sensitivity for HTI-027 (left) and distribution of differences (right).

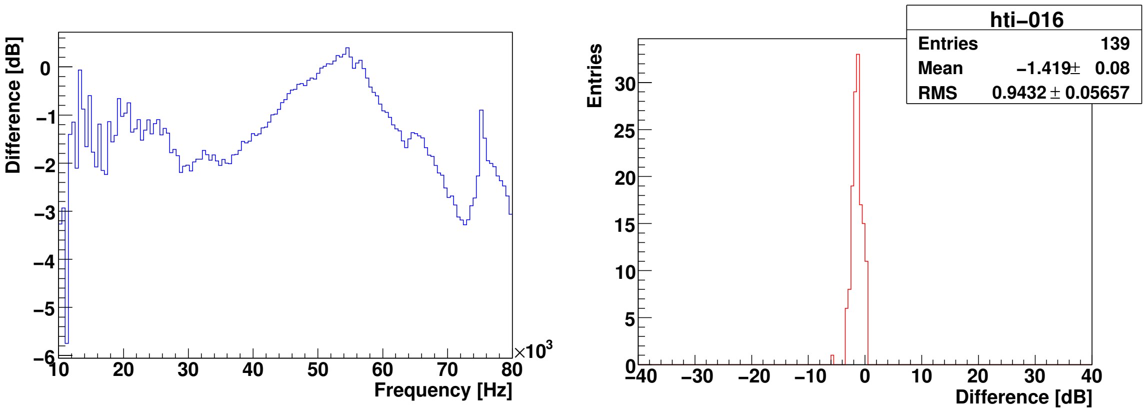

Figure 5.5: Frequency dependent difference of the mean sensitivity for HTI-016 (left) and distribution of differences (right).

HTI-	Mean	RMS
007	+ 0.71 dB	1.94 dB
011	+ 2.00 dB	1.39 dB
016	- 1.42 dB	0.94 dB
025	+ 1.50 dB	1.45 dB
026	+ 0.95 dB	1.04 dB
027	+ 2.24 dB	1.51 dB
029	+ 0.46 dB	1.36 dB

Table 5.1: Mean and RMS value for the difference (sensitivity prior to deployment minus sensitivity after recovery) of the mean sensitivity for HTI hydrophones.

5.2 LTI hydrophones

The functionality test of the five LTI hydrophones installed on L 12 (LTI-106, LTI-107, LTI-109, LTI-111, LTI-113) showed fully operational hydrophones except for LTI-107 which was inoperabel since the deployment. These sensors were recalibrated in the same way as the HTI hydrophones to obtain their sensitivity.

Exemplary, the difference of the mean sensitivities prior to deployment and after the recovery is shown for LTI-111 in Figure 5.6. The distributions for the other hydrophones are given in Appendix A.2. The mean value of the distribution indicates an increase of sensitivity of about 3.08 dB with a RMS of 2.13 dB. The biggest differences in the data distribution obtained for all LTI hydrophones (see Table 5.2) of - 4.91 dB (LTI-106) with a RMS of 3.58 dB and + 3.18 dB (LTI-113) with a RMS of 2.13 dB render the results for the LTI hydrophones also consistent with no variation due to the exposure to the deep sea. The big RMS is caused by systematics in the calibration procedure, for example by the cut of the reflections which is more difficult for this type of hydrophone.

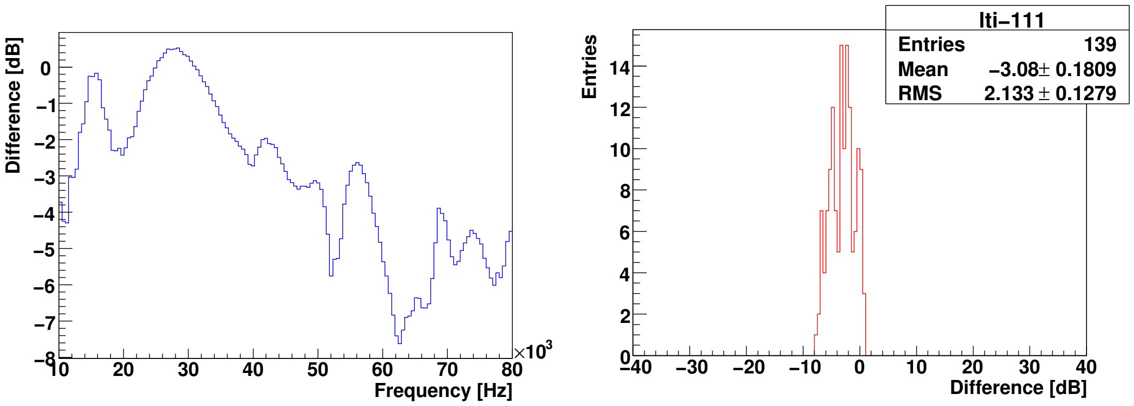

Figure 5.6: Frequency dependent difference of the mean sensitivity for LTI-111 (left) and distribution of differences (right).

LTI-	Mean	RMS
106	- 4.91 dB	3.58 dB
109	- 0.82 dB	1.72 dB
111	- 3.08 dB	2.13 dB
113	+ 3.18 dB	2.13 dB

Table 5.2: Mean and RMS value for the difference (sensitivity prior to deployment minus sensitivity after recovery) of the mean sensitivity for LTI hydrophones.

These hydrophones were redeployed and are fully operational. The defective LTI-107 was exchanged by HTI-032.

5.3 Spare hydrophones

In this last section of this chapter the calibration results for spare[3] hydrophones labelled HTI-030, HTI-031, HTI-032, HTI-33 and HTI-034 are described. As already mentioned, three out of these five hydrophones were deployed as replacement for other sensors and are taking data. The last two are kept for additional tests and eventual replacement in the laboratory. As all HTI hydrophones show similar behaviour, only data obtained with HTI-033 are shown. These are representative for all spare hydrophones.

A calibration in azimuthal angle is performed for the spare hydrophones in order to verify the assumption of an almost constant sensitivity for this orientation. The hydrophones are mounted as described in Section 3.2 and the calibration signals are emitted and treated as described in Chapter 2. Figure 5.7 shows the obtained result for the ramp signal (left) and the 80 kHz Gaussian pulse (right), again with a stepsize of 15°. Both plots verify the expected high uniformity of ∼ 15% in the azimuthal plane.

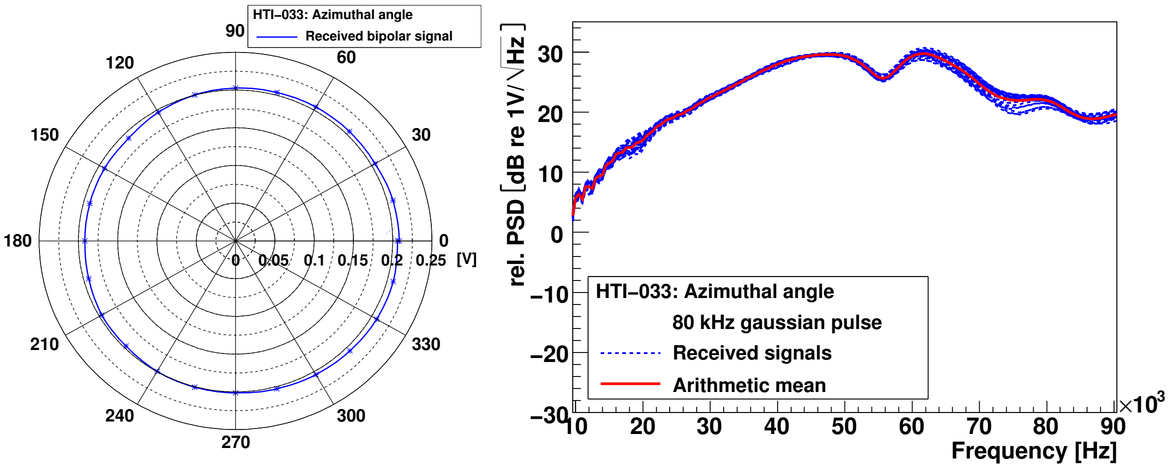

Figure 5.7: Azimuthal calibration for HTI-033. The APP values of the received bipolar pressure pulse (left, blue crosses) are almost equal for a complete turn in azimuth. The deformation of the result, observable as small shift to the right, might be an indication for a misaligned sensor. The PSDs of the recorded 80 kHz Gaussian pulses (right, 24 blue dashed curves) vary only slightly. The red curve gives the arithmetic mean.

The results of the polar calibration for HTI-033 (mounted as described in Section 3.2) are shown in Figure 5.8. The calibration signals are again emitted and treated as described in Chapter 2. These spare hydrophones behave exactly as the other HTI hydrophones before.

---

[3] Spare, as not already used in the AMADEUS setup.

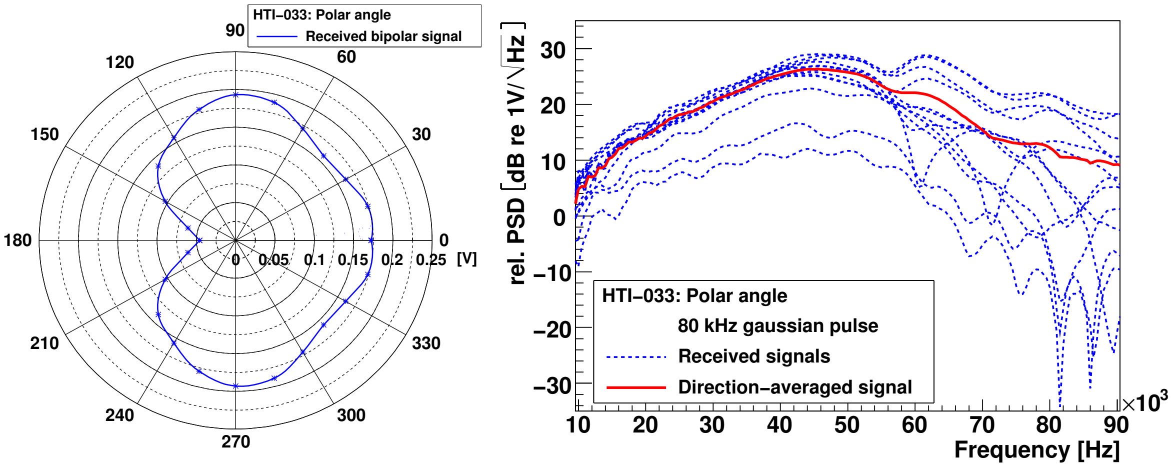

Figure 5.8: Polar calibration for HTI-033. The A_{PP} values of the received bipolar pressure pulse (left, blue crosses) show the same behaviour as for all the other hydrophones with an obvious signal attenuation for ϑ between 135° and 225°. The PSDs of the recorded 80 kHz Gaussian pulses (right) are shown as blue dashed curves together with the red direction-averaged curve.

Part IV

Acoustic modules

Chapter 6

General description

This chapter gives a short description of the Acoustic Modules (AMs) which were developed in [10] and which were taken up again in this work. An AM consists of two acoustic sensors glued to the inside of a standard ANTARES glass sphere. This sphere is a "*VITROVEX®sphere*" from *Nautilus Marine Service GmbH* [27] with an overall diameter of 17" (432 mm) and a glass thickness of 14 mm rendering it pressure resistant up to $7 \cdot 10^7$ Pa corresponding to a water depth of about 7000 m. This sphere consists of two hemispheres:

- An upper hemisphere painted black to protect the PMT inside a standard Optical module (OM) from light arriving from the back (Figure 6.1, top). This hemisphere is equipped with a manometer and a pressure valve needed for the closing of the sphere and a penetrator for signal/voltage feed and readout cables;

- A naked lower hemisphere as glass window for the PMT (Figure 6.1, bottom).

There is no reason to use a black painted upper hemisphere in the case of an AM, but as its design is based on the OM design, the identical spheres are used accordingly. Each of the three OMs of an ANTARES storey is connected to a dedicated sampling board inside the LCM. In the case of the AMs it was possible to share one ADC board (the AcouADC board) for the readout of two acoustic sensors due to the different data acquisition requirements. Thus a total of six sensors can be operated with the three available AcouADC boards for every AM Acoustic Storey. These six sensors are distributed allover the horizontal plane to completely cover this plane with overlap in the opening angles of the single sensors. The horizontal plane is defined by the plane perpendicular to the storey vertical axis at the maximum circumference of the three glass spheres. This plane is preferred for acoustic detection methods because of the larger "visible" volume for each sensor. In vertical direction this volume is restricted by the sea surface on the one hand and the sea bed on the other, whereas in the horizontal plane the volume is only limited by the signal attenuation length (of the order of 1 km in the frequency range of interest). The two sensors in each sphere (the spheres themselves are separated by 120°) are separated by 60° on a great circle in the equator (horizontal) of the sphere. As the spheres are tilted by 45°,

Figure 6.1: Photograph of the two hemispheres of a Vitrovex sphere:
The photograph on the top left side shows the inside of the upper hemisphere. The penetrator with the cable feed-through and the manometer for pressure monitoring are visible in the upper half of the photograph. The small argentic point on the lower half is the pressure valve for the depressurisation of the sphere. On the top right side the photograph shows the outside of the upper hemisphere. The penetrator with the attached cable is visible next to the manometer almost in the centre.
The photograph at the bottom shows the lower hemisphere. The attached tape with markers is used for the AM assembly described later.

this results in a position in the lower hemisphere. Thus the sensors are placed 45° below the equator of the hemisphere. Figure 6.2 depicts the final position of the sensors.

The acoustic sensor itself consists of a piezo disc of cylindrical shape, 25.4 mm in diameter and 10 mm in thickness. The sensor is in principle the same as in the LTI hydrophones, except for the piezo ceramics. It is equipped with a twostage preamplifier (for a more detailed description see [10] and Chapter 9) and several copper shields to minimise electromagnetic coupling arising from internal electromagnetic noise. This is already done as preparation for a combined usage with PMTs, cf. Chapter 11. The outer copper tube is additionally filled with PU to provide the sensor with a rigid structure and dampen the resonant movement of the piezo element. The preamplifiers are powered by a DC volt-

Figure 6.2: Photograph of an AM mounted to the OMF with the acoustic sensors located in the horizontal plane.

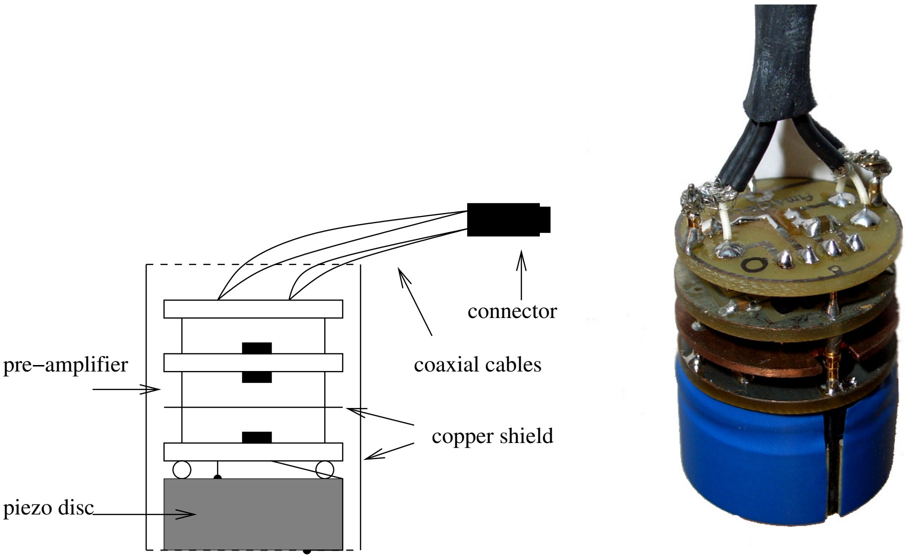

Figure 6.3: Schematic (left) and photograph (right) of an AM acoustic sensor [10]. The photograph is taken without the copper tube for visualisation purposes.

age of 6.0 V and the differential signal is readout via two cables (signal + and signal -), identical to the hydrophones. Figure 6.3 shows the shematic of an AM sensor as well as a photograph of the sensor before the PU coating.

Chapter 7

Comparison of calibration results

The recovery of L 12 gives the opportunity to test and – if needed – repair the acoustic devices mounted inside the AMs, as was already mentioned for the hydrophones. A repair was necessary as one acoustic sensor was expected (from its deep-sea performance) to be detached from the sphere. A recalibration in the sense performed for the hydrophones should not be necessary for the AMs as their sensors are well-protected against the deep-sea environment by the glass sphere. No pressurisation and ageing takes place as long-term stability is guaranteed by using piezo ceramics, a low voltage power supply and mostly resistors and capacitors to operate the sensors.

The recovery exposed a different problem instead. The lower hemispheres (the ones with the attached sensors) for two AMs showed spalling of glass. This spalling was caused by the AM support frames as seen in Figure 7.1 (left).

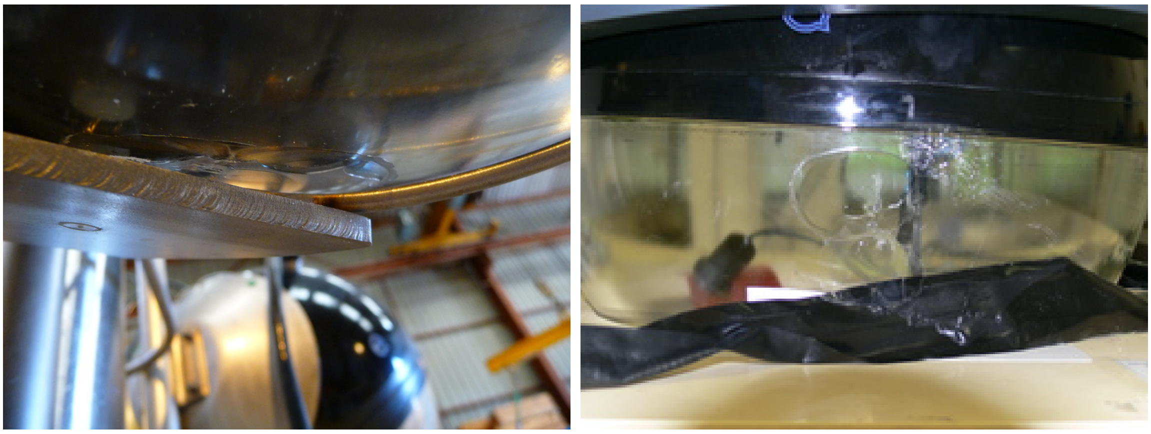

Figure 7.1: Photograph of an AM with visible spalling. On the right side the black tape covering the AM is visible with an attached piece of thin glass.

The surface area of these spallings covers about 5×5 cm^2 near the equator of the sphere but is only superficial with a thickness of a fraction of 1 mm (see Figure 7.1, right). In principle these spallings represent no harm to the structural integrity of the sphere according to the manufacturer and their safe operation is confirmed. To further study the problem, the decision was made to open all three AMs and to exchange the damaged hemispheres. The third AM is opened to reattach the sensors and thus to ensure a good connection of all sensors to the glass surface. Therefore all six sensors were reglued. The resulting characteristics of the AMs are not comparable to the "old" ones because of:

- Their sensor positions, which are not identical due to the difficult determination of the correct position on a curved surface;
- The way they are glued to the sphere is different. This manifests itself in a different glue composition as well as in different amounts of inserted glue and the processing of both, glue and glueing;
- The small amount of residual glue on the piezo faces was not removed in order to protect the piezo surface. Therefore the acoustic sensors are connected over a second layer of glue to the glass. As both layers are very thin, effects of this double layer should be negligible.

Therefore, a new calibration for the reintegrated AMs was performed, described in the next section.

An assembly instruction for AMs is developed in the course of the glueing procedure, this instruction is presented in Appendix B.

7.1 Calibration

Three facts render it impossible to operate an AM in the small tank:

- There is no way to adjust the orientation of an AM unless it is mounted to an additional support structure due to its almost perfect spherical shape;
- The buoyancy of about 200 N has to be countered by a sufficient amount of weight to keep it under water;
- Its overall dimensions allow for only insufficient coverage with water in all directions in the small tank.

The AMs are calibrated in the big tank within the setup described schematically in Figure 7.2.

The AM is mounted to its support inclined by 45° (corresponding to its final position on the OMF) by clamping two flat steel rings ("discs") with three all-thread rods to the top and to the bottom of the sphere. Small strips of neoprene are placed in between the glass and the discs to protect the AM. A lead weight (about 25 kg) is attached to the steel

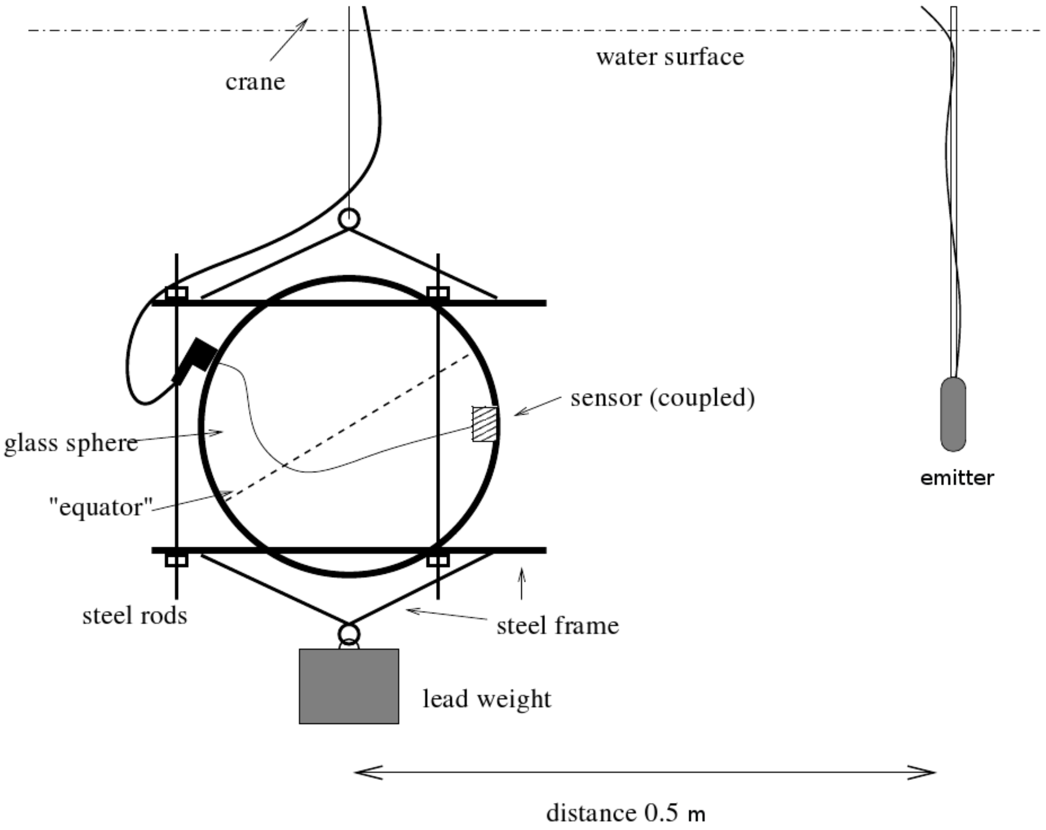

Figure 7.2: Schematic AM calibration setup. The shown distance of 0.5 m between the emitter and the centre of the sphere corresponds to a distance between emitter and sensor of about 25 cm.

frame of the lower disc whereas the steel frame of the upper disc is connected to a crane. An emitter is mounted to the working platform at a fixed distance and at the required depth. It is possible to move the complete setup (AM mounted to its support structure and equipped with a weight, adding up to about 50 kg) to almost every position in the big tank with the help of the crane. Once submerged, the support structure of the AM has to be connected to a working surface to fix the AM in its position. The calibration depth (depth measured from the water surface to the piezo centre both for emitter and AM) is restricted to ~ 30 cm by the output cable of the AM with a length of 1 m. At this maximum depth it is still possible to turn the AM in azimuthal direction. The distance between emitter and receiver is chosen to be 25 cm when both are directly facing each other. When the AM is turned in the horizontal plane around its centre, the sensor being off centre turns away from the emitter. The reference angle $\varphi = 90°$ is defined through the position where the emitter is facing the acoustic sensor directly. For the second sensor the reference is chosen accordingly. This setup with varying emitter-receiver distances is chosen for simplicity of the calibration procedure as it is possible to adjust both devices to separate work surfaces or the working platform at a defined distance. The different sensors of one sphere are powered and readout consecutively through a connector, cf. Section 10.1. Due to the short time available for the calibration measurements it was impossible to refine the calibration setup. An improved setup used for later measurements is described in Section 10.2.

Only the measurements with varying azimuthal angle are performed for the AMs. The sensitivity gained for the polar angle should be identical due to the symmetry of both sphere and piezo disc, cf. Section 10.4. The azimuthal angle is varied between 0° and 180° with a stepsize of 15°, giving a range of ± 90° around the sensor centre. For each acoustic sensor the calibration signals are emitted, recorded and analysed.

7.2 Analysis

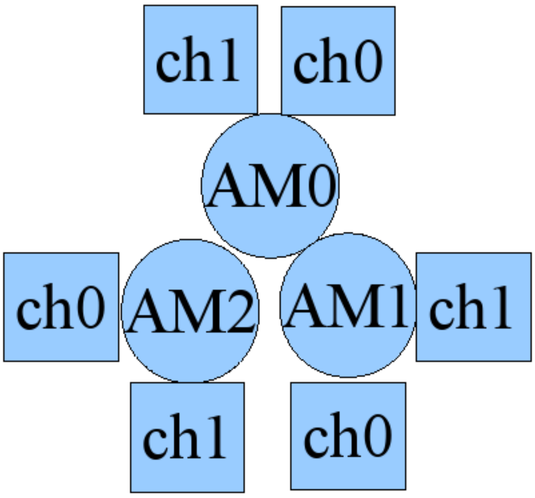

Figure 7.3: Labelling of the AM sensors with respect to the OMF, looking from above.

Figure 7.4 shows the data sample for AM1-ch1 for $\varphi = 60°$ and the 80 kHz Gaussian calibration pulse. For the labelling of the sensors, cf. Figure 7.3. In this exemplary data sample the sonic waves coupled into and propagating through the glass sphere lead to a superposition of the different signals rendering it impossible to separate the primary signal from the time delayed reflections. Therefore the whole data set is processed without applied cut, that means for signal lengths of 500 µs without zero-padding. Figure 7.5 shows the PSDs of the recorded data samples for the different directions together with the arithmetic mean of the PSDs. The PSDs obtained for different directions are dominated by the oscillations resulting from the not removed reflections and the signal cut with non-zero amplitude at the end of the data sample. The mean PSD is improved by averaging.

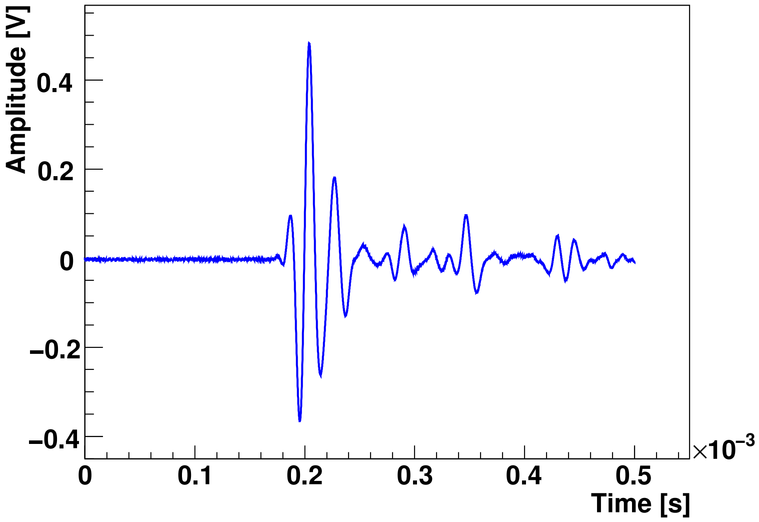

Figure 7.4: Data sample (AM1-ch1) for $\varphi = 60°$ and the 80 kHz Gaussian pulse. The signal is a composition of the primary signal, signals reflected and propagated in the sphere and external reflections.

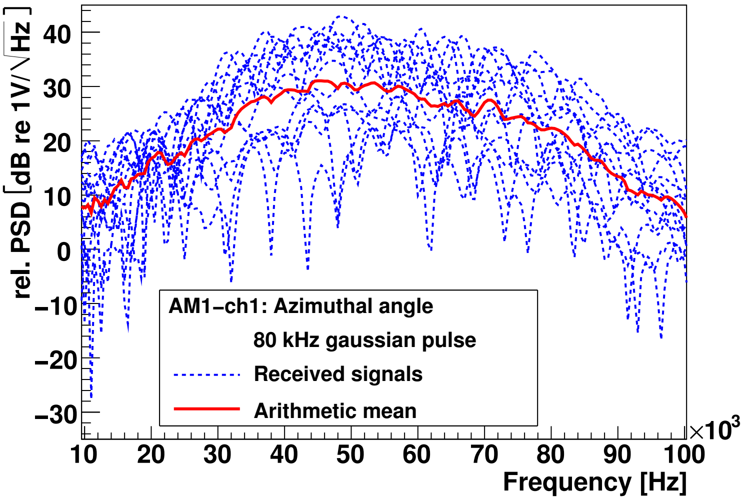

Figure 7.5: Obtained PSDs for AM1-ch1 and the 13 different incident angles (blue, dashed lines). The occurring oscillations are mainly caused by a non-zero amplitude at the end of the data sample, cf. Figure 7.4. These oscillations are smeared out in the arithmetic mean (red, solid line).

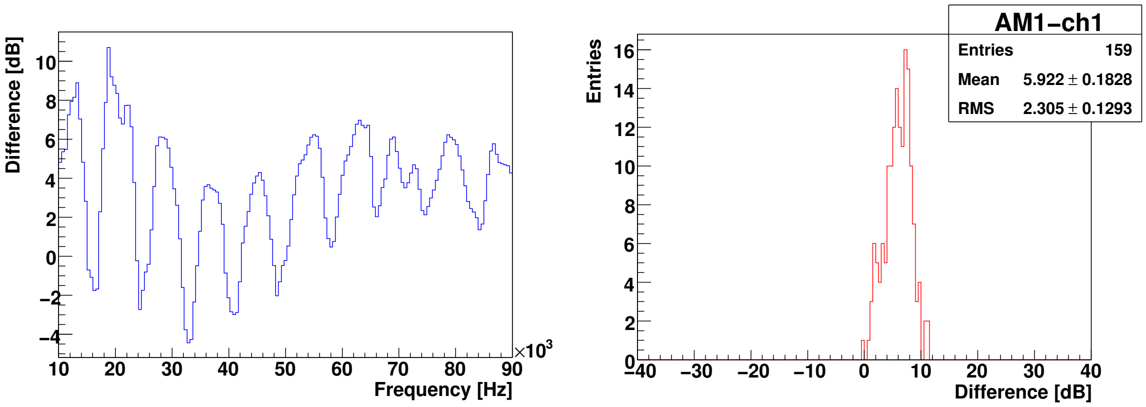

Figure 7.6: Frequency dependent difference of the mean sensitivity for AM1-ch1 (left) and distribution of differences (right).

Sensor	Mean	RMS
AM0-ch0	+ 3.72 dB	3.21 dB
AM0-ch1	+10.16 dB	5.87 dB
AM1-ch0	+ 8.23 dB	3.68 dB
AM1-ch1	+ 5.92 dB	2.31 dB
AM2-ch0	+ 3.98 dB	3.37 dB
AM2-ch1	+ 4.48 dB	4.47 dB

Table 7.1: Mean and RMS value for the difference (sensitivity prior to deployment minus sensitivity after reglueing) of the mean sensitivity for the AMs.

Figure 7.6 shows the result of a comparison of AM1-ch1 prior to deployment and after reglueing. The distributions for the other AMs are given in Appendix A.3. With a mean of 5.92 dB and a RMS of 2.31 dB the obtained result for AM1-ch1 is consistent with no significant variation, although the calibrations are not fully comparable. The data distributions (see Table 7.1) for AM0-ch1 and AM1-ch0 show abnormal deviations of 10.16 dB (RMS of 5.87 dB) and 8.23 dB (RMS of 3.68 dB), respectively. The reasons for this deviations have to be studied in more detail.

The reglued and fully calibrated AMs are operational and taking data on the redeployed L 12.

Part V

Towards opto-acoustical modules

Chapter 8

Concept of future detector elements

The experiences made with ANTARES lead to the following requirements for future active detector elements:

- The operation of the ANTARES neutrino telescope shows that the connections between the parts of the detector are the components that are most likely to fail (see loss of connection to Line 12 during operation). Therefore the amount of connectors and single components has to be reduced;
- The complexity should be reduced to a minimum. It is very difficult[1] to repair detector components after installation, so all parts have to be reliable and well tested;
- Utilise same or similar designs for pressure resistant housings of the detector elements in order to minimise efforts arising from different dimensions;
- Best possible utilisation of the existing module volume. The spheres themselves cause up to 200 N buoyancy adding up to 1.5 kN without buoy in the case of the ANTARES lines consisting of 75 OMs. This buoyancy has to be compensated by a sufficient amount of deadweight to keep the line on the seabed. This leads to higher costs because of the material as well as increasing requirements on all parts (especially the cables) of the detector to handle the occuring forces.

The AMs work very well within their specification so they seem a viable type of sensor for acoustic particle detection. This concept is in compliance with the requirement of similar design for all elements of a detector, as the same modules are used for OMs and AMs. Identical support structures as well as the whole infrastructure can be used without modifications. As expected the performance and characteristics of the AMs allows to reconstruct the position of its storey at a cm level. This is roughly the same precision as the dedicated acoustic positioning system [28] used for ANTARES consisting of a set of emitters/receivers (Rx/Tx), tiltmeters and compasses. Therefore this concept is an interesting option for the alignment of a future water Cherenkov neutrino telescope if

---

[1] The recovery of a line is expensive and exposes the material to high levels of stress.

distributed over the complete volume of the detector, rendering dedicated receivers unnecessary. Acoustic emitters at well known positions are still necessary for this positioning purposes but their power might be reduced with respect to the power of the emitters used in ANTARES, depending on the detector size, as the existing ones are saturating the AMs due to their high sensitivity.

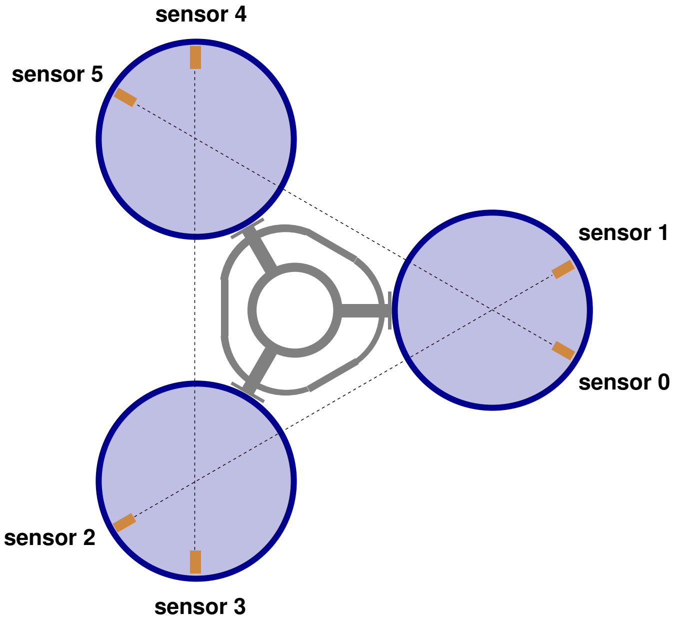

Figure 8.1: Top view of an Acoustic Storey, housing three AMs with two sensors each.

Considering the AM layout, see Figure 8.1, the sensors inside the glass spheres provide sufficient space for a possible combination of different detector parts, meeting another requirement mentioned above. For example the combination of acoustic sensors and optical beacons used in ANTARES for calibration purposes. Another possibility is the combination of optical and acoustical sensors. These sensors would in this option be housed in one sphere by additionally reducing the amount of needed electronics and connectors. The combination of a PMT together with one or several acoustic sensors would give the resulting opto-acoustical module (OAM) the opportunity to combine two complementary detection methods as well as to determine its position in space on its own.

In the following chapters first steps to test this possible combination are described.

Chapter 9

Preamplification

As already pointed out, the expected signals for acoustic detection are very weak and accordingly so are the voltage signals generated by the sensors. To minimise the pickup of noise it is mandatory to use preamplifiers directly after signal generation in the piezo ceramic before routing the signal to other parts of the module or the detector. For the following studies the same preamplifier design as already implemented in the AMs is used. This design consisting of operational amplifiers (OP) might have potential for optimisation concerning low inherent noise and power consumption but it is a very robust design fulfilling all requirements. For the future, further investigations and tests with different preamplifier designs, for example a transistor based design, can be performed.

9.1 Design

Concerning its design, the preamplifier has to fulfill two major tasks:

- Preamplification of the signals by a reasonable factor of about 50 corresponding to a gain of about 34 dB in the frequency range of interest, in our case between 1 kHz and 80 kHz → Amplification;
- Suppression of other frequency ranges to remove low frequent ambient noise and high frequent, mostly electronics noise → Bandpass characteristics.

The preamplifier used in the AMs is a current amplifier according to [10]. The piezo itself generates a voltage signal when pressure is put on it. Simply describing the piezo ceramic as dielectric material between two electrodes on top and at the bottom, this voltage signal is converted to a current signal according to:

$$C = \frac{Q}{U} \Rightarrow I(t) = \frac{d\,Q(t)}{dt} = \frac{d\,(C \cdot U(t))}{dt} = C \cdot \frac{d\,U(t)}{dt}. \tag{9.1}$$

The general design of the AM preamplifiers is shown in Figure 9.1, created with the program TINA-TI$^{\mathrm{TM}}$ Version 7 [29] which is a freely available Analog Circuit Simulation tool from *Texas Instruments*.

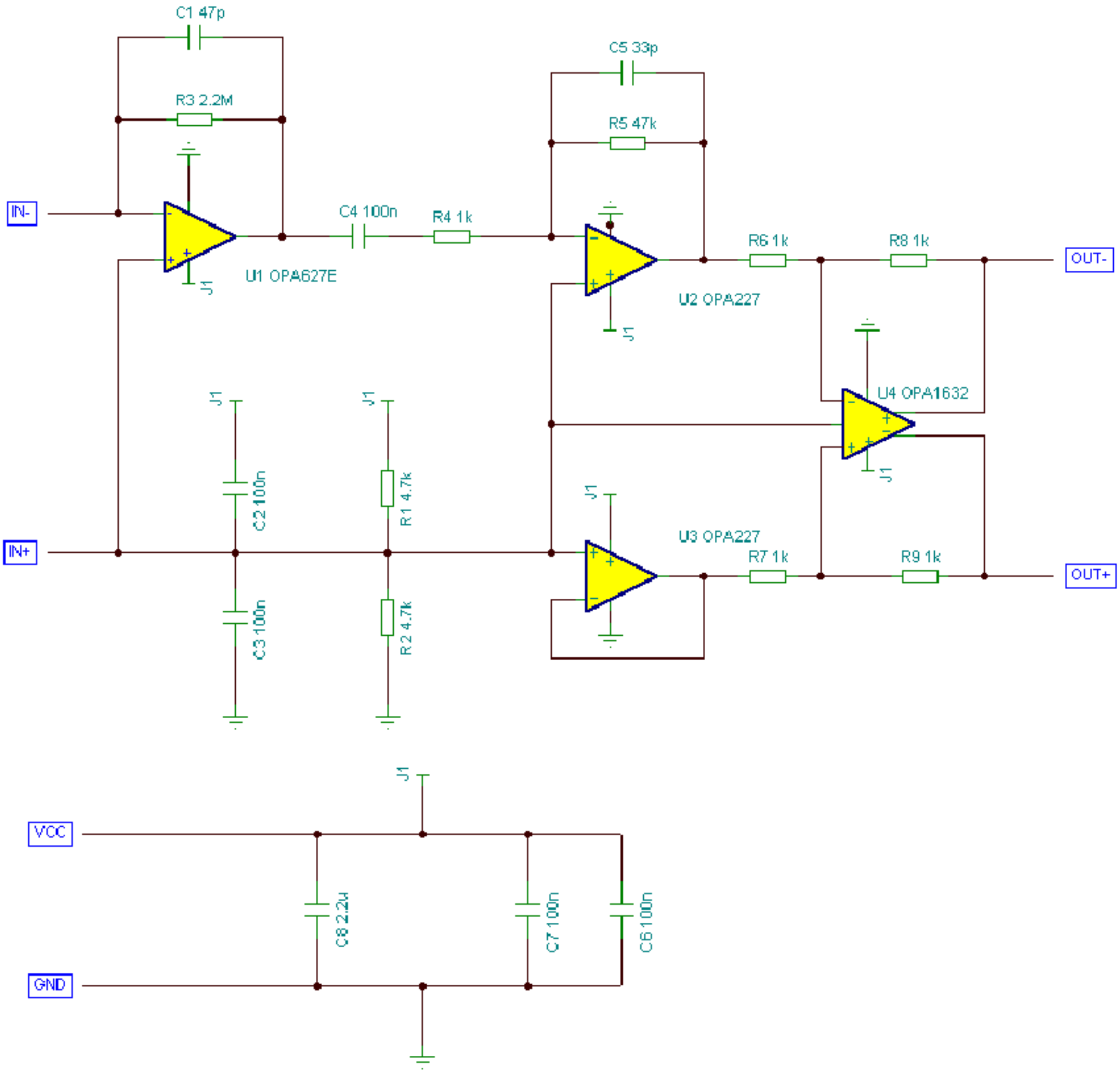

Figure 9.1: General preamplifier design.

This program is capable of creating the schematics shown in the figure as well as performing a variety of analyses of a circuit. To check whether this preamplifier design meets its requirements, the program is used to determine the AC transfer characteristic of the system, meaning the amplitude and phase response of the preamplifier to an applied signal as a function of the frequency of the signal. The program therefore performs sweeps of sinusoidal signals with frequencies in a specified range and calculates the resulting transfer spectrum. Here the range between 100 Hz and 1 MHz is chosen to cover the whole range of interest including one additional order of magnitude at high and low frequencies. The schematic in Figure 9.1 shows only the design of the amplifier and no fully operational

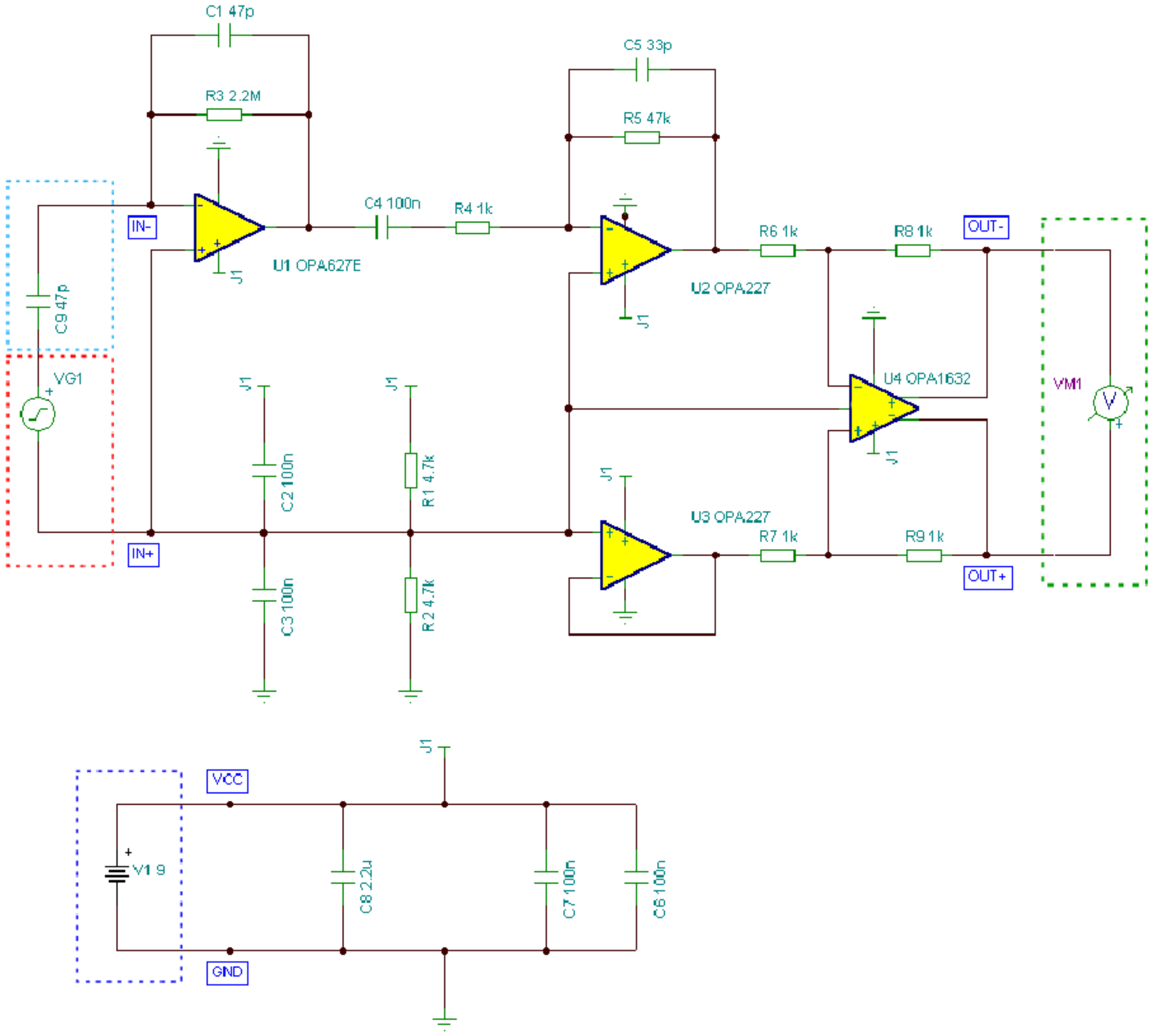

Figure 9.2: Schematic used for system characteristics test with power supply (blue dashed box), voltmeter (green dashed box), voltage generator (red dashed box) and 47 pF capacitor (black dashed box) as described in the text.

test system where the transfer spectrum can be calculated. To complete the circuit for the simulation some parts have to be added, as shown in the color bordered boxes in Figure 9.2.

These parts are:

- The power supply (V1 9), here 9 V, is chosen since the components are designed for the use in the range from 9 V to 12 V;
- The voltmeter (VM 1), to measure the resulting signal after preamplification;
- The voltage generator (VG 1), to generate the sweep of the sinusoidal input signal;
- The 47 pF capacitor (C 9) as a substitute for the main capacity of the piezo ceramic.

The Bode diagram in Figure 9.3 shows the optimal amplitude and phase response to an applied signal as calculated by TINA-TI$^{\text{TM}}$ with the settings given above.

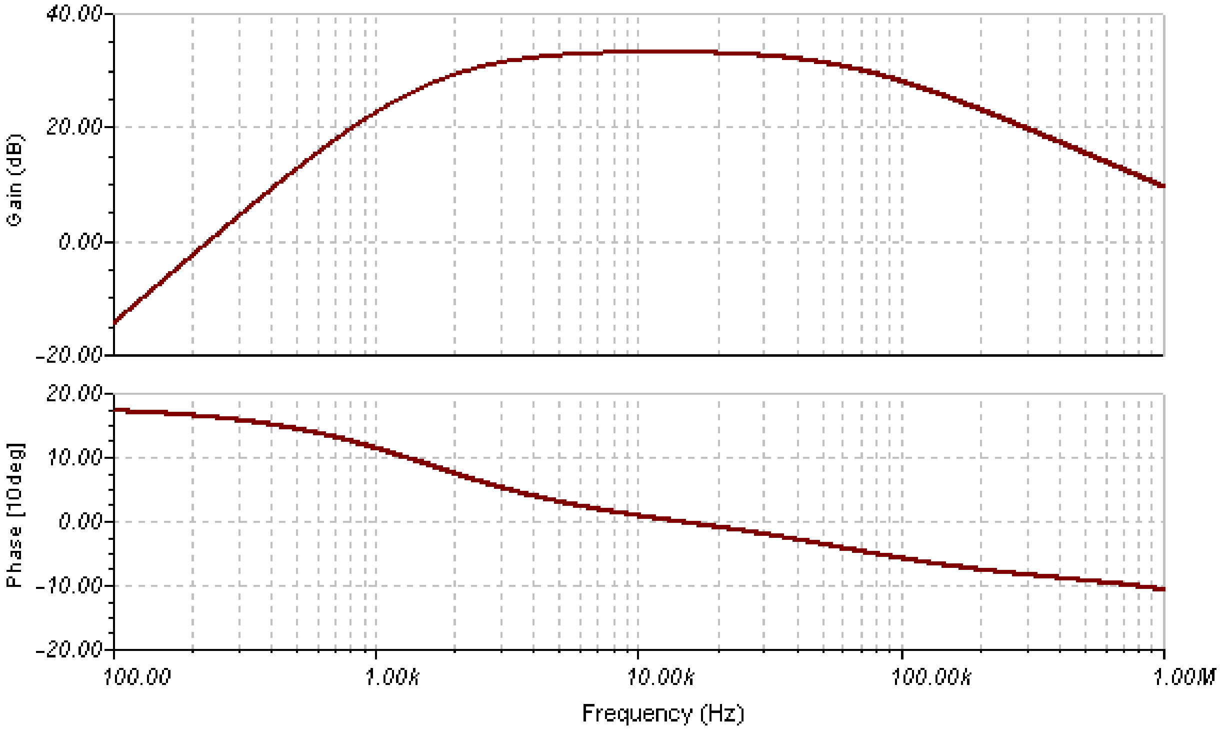

Figure 9.3: Bode diagram obtained with TINA-TI$^{\text{TM}}$.

This plot confirms that the tasks set forth for the circuit are well fulfilled. In the range from about 800 Hz to about 300 kHz the gain lies above 20 dB corresponding to an amplification factor of 10 for the amplitude and the phase response is nearly linear corresponding to an almost constant time shift for all signal frequency components. In the frequency range between 3 kHz and 60 kHz the gain lies above 30 dB.

9.2 Measurement

As the preamplifier design was confirmed to comply with the requirement, a total of three specimen was ordered at our local electronics workshop. After delivery, the first step was to reproduce the theoretically expected characteristics in the laboratory. Therefore the transfer spectra for amplitude and phase were quantified.

The procedure is similar to the sensitivity measurements of the hydrophones described in Section 2.2. The preamplifier is powered by a 9 V external power supply. The calibration signal, Gaussian signals with different pulsewidth corresponding to different main frequencies, is emitted via a waveform generator with an amplitude of 50 mV. This signal is coupled via a 47 pF capacitor, mimicing the dielectric characteristics of a 25.4×10-disk shaped piezo element as used in the AMs, to the input of the preamplifier. In parallel the signal is fed without capacitive load to one input channel of the oscilloscope. The external trigger signal for the oscilloscope is also emitted from the waveform generator. The two outputs of the differential preamplifier are then connected to two channels of the oscilloscope which accordingly calculates the received signal by subtraction. Both, the emitted and the received differential signal are saved to disk. To improve the performance of the measurement a total of 2000 pairs of emitted and received signals is recorded and subsequently averaged for every pulsewidth.

The different Gaussian signals are chosen such that they cover the complete frequency range between 100 Hz and 1 MHz, therefore varying between a σ of 1.00 µs and 10.24 ms. To obtain a sufficient amount of data points with the oscilloscope, 250 kS are recorded for every pulse with varying timebase between 20 ms and 20 µs as this also has a great impact on the frequency range. Figure 9.4 shows some examples of the recorded signals for different combinations of pulsewidth and timebase. For the signal with 80 µs pulsewidth and 40 µs pulsewidth, both with 10 ms timebase, see Figure 9.4 (middle row), it is obvious that the amount of useful data points in this combination reaches a lower limit. For smaller σ's therefore a shorter timebase is needed. The improvement can be seen in the last two plots.

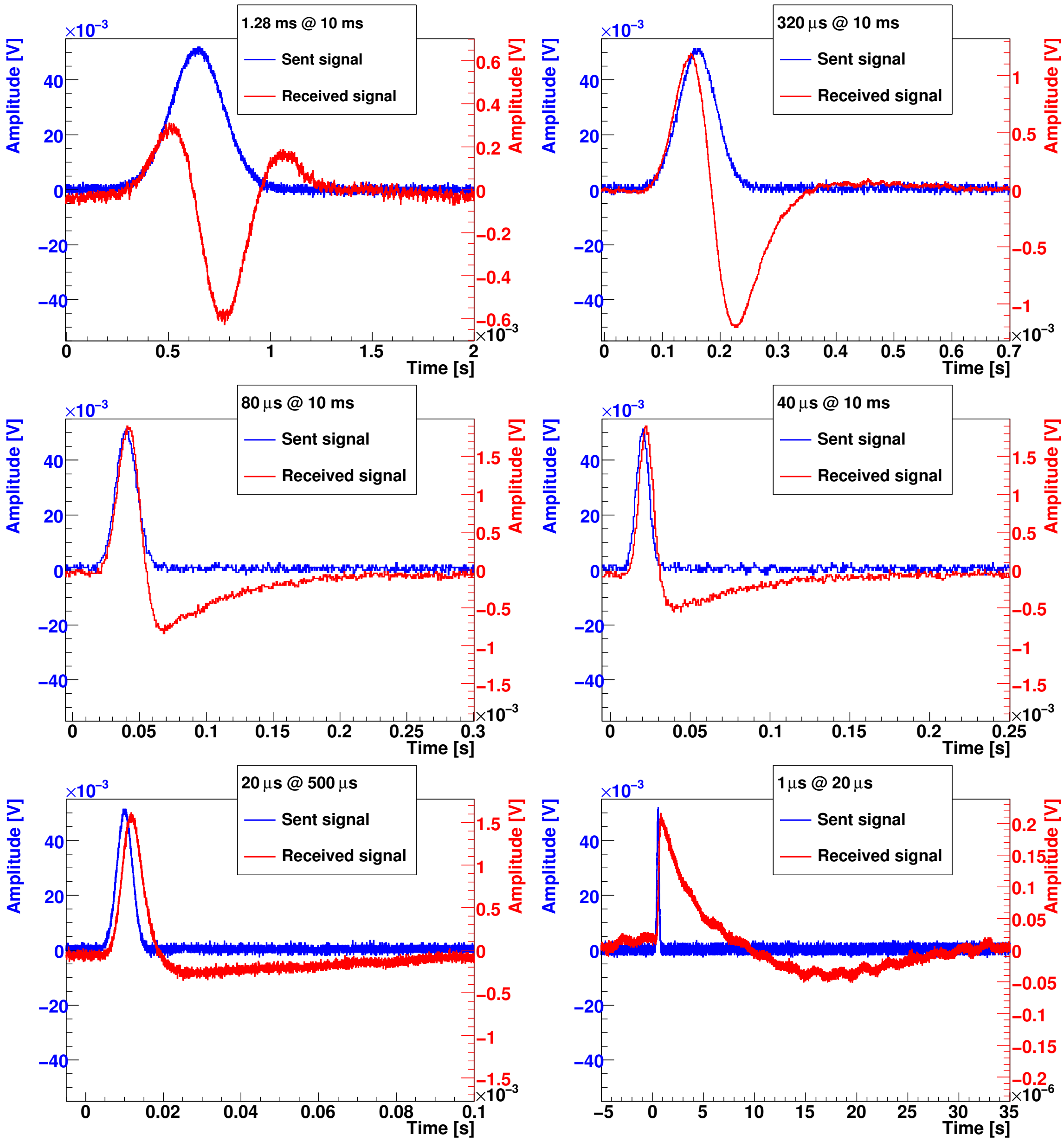

Figure 9.4: Sent and received calibration signals with decreasing pulse width from top left to lower right.
Top row: Sent signal with 1.28 ms pulsewidth and 10 ms timebase (left), sent signal with 320 µs pulsewidth and 10 ms timebase (right);
Middle row: Sent signal with 80 µs pulsewidth and 10 ms timebase (left), sent signal with 40 µs pulsewidth and 10 ms timebase (right);
Bottom row: Sent signal with 20 µs pulsewidth and 500 µs timebase (left), sent signal with 1 µs pulsewidth and 20 µs timebase (right).

9.3 Results

After the measurement, the data are moved to the ECAP computing network where the PSD of the signals is obtained by applying a Fourier transformation. The difference of the PSD for the emitted signal and for the received one gives the transfer function of the system as described in Section 2.2. Figures 9.5 and 9.6 show examples of calculated amplitude and phase response, respectively, together with the theoretical values obtained with TINA-TI$^{\mathrm{TM}}$. From these it is obvious that one signal with a given pulsewidth is not sufficient to cover the whole frequency range of interest, as one pulse setting only covers a part of the spectrum with sufficient signal to noise ratio S/N. It is mandatory to use only parts of the PSD for each pulse, removing frequency intervals where no physical information is gained or where measurement systematics dominate the PSD. These parts are identified by the green dashed lines visible in the Figures. The systematics show up for the higher frequencies in an almost constant gain level for the amplitude response and in the distribution all over the range of values for the phase response. In the lower frequency regime, the appearing deviations from the theoretical data might also be the effect of the systematics of this measurements. After that the single spectra of the various measurements are combined to the spectrum shown in Figures 9.7 and 9.8.

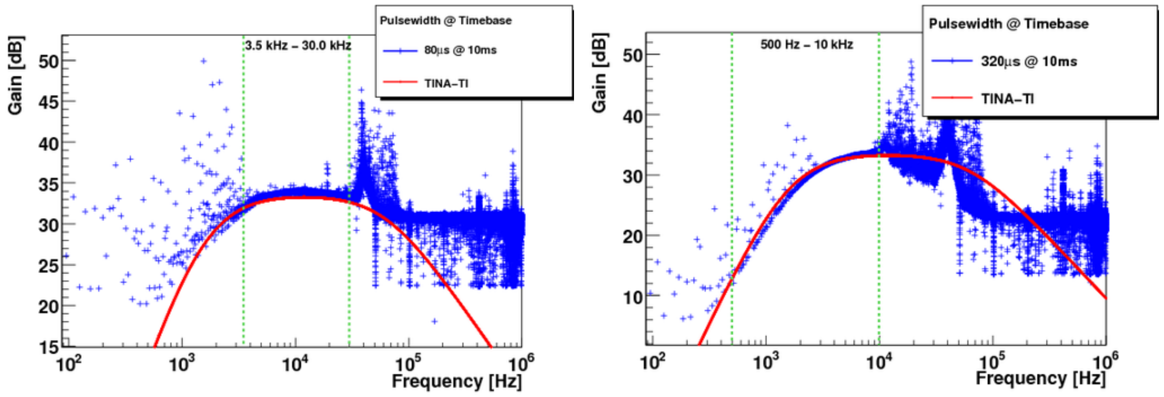

Figure 9.5: Examples of the calculated and expected amplitude response for signals with 80 µs (left) and 320 µs pulsewidth (right), both with 10 ms timebase. The green dashed lines mark the used parts of the PSD. These plots are further described in the text.

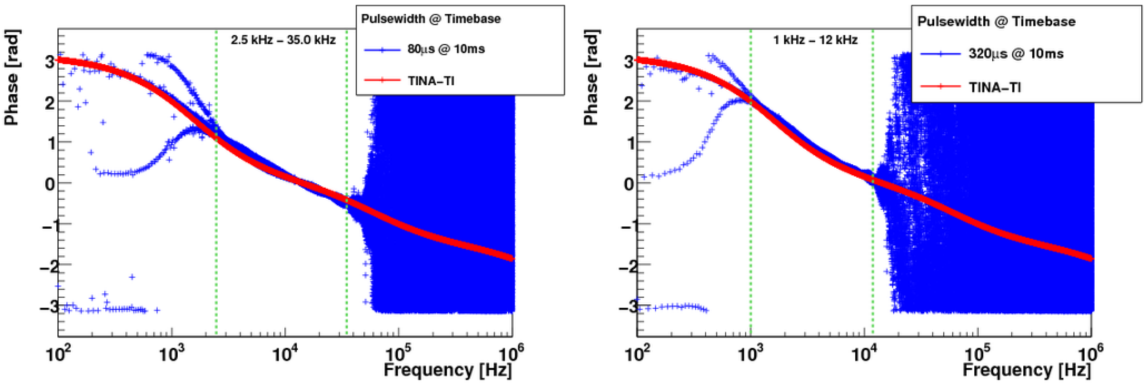

Figure 9.6: Examples of the calculated and expected phase response for signals with 80 µs (left) and 320 µs pulsewidth (right), both with 10 ms timebase. The green dashed lines mark the used parts of the PSD. These plots are further described in the text.

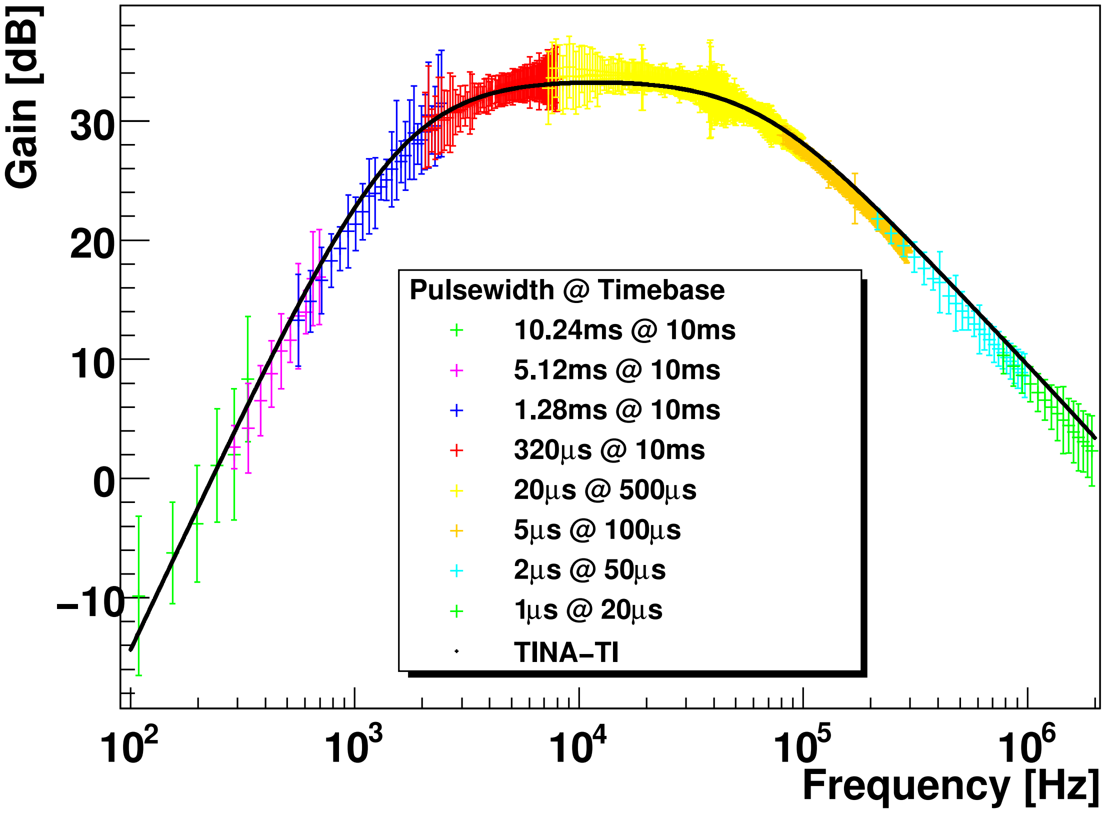

Figure 9.7: Amplitude response. The plot is further described in the text.

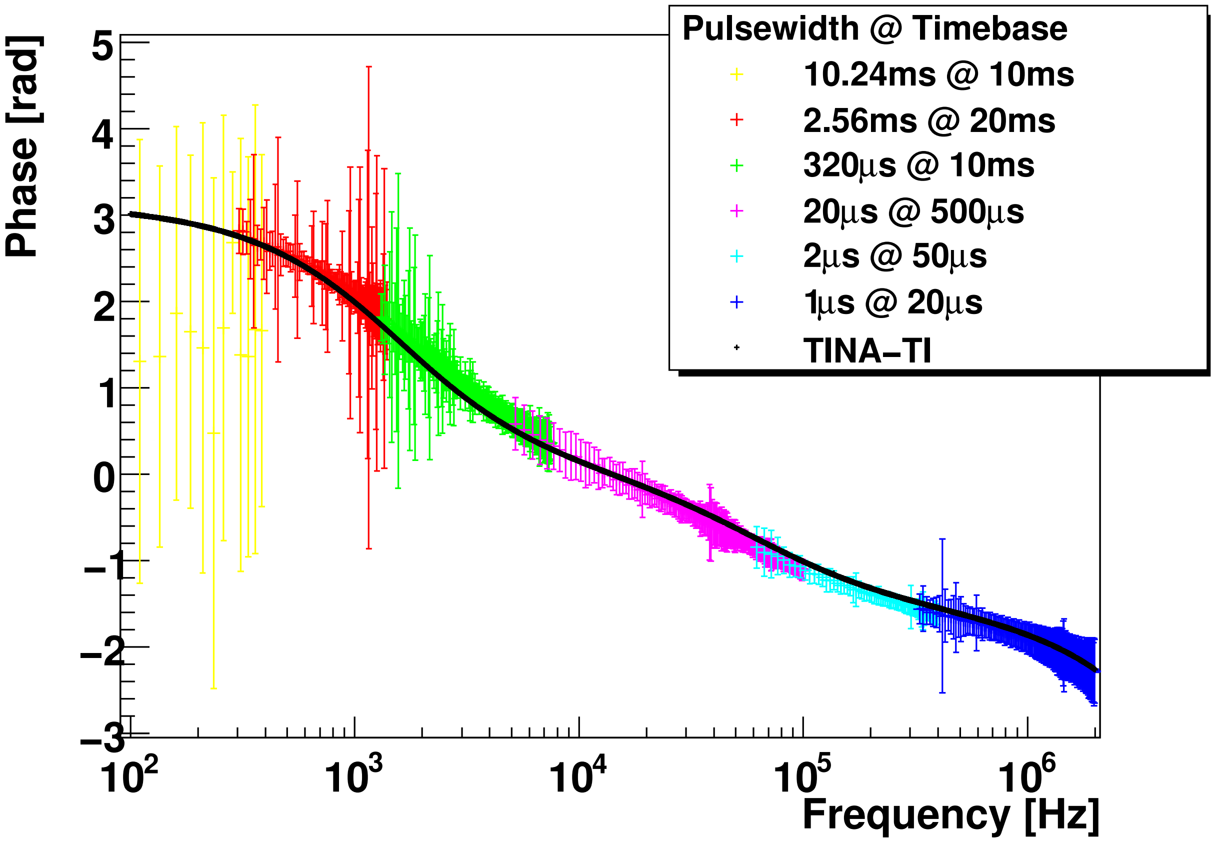

Figure 9.8: Phase response. The plot is further described in the text.

In the last two plots the measurement systematics are visible through the large error bars for some parts of the spectrum. Manufacturing tolerances of the components contribute to the systematic errors as well as some differences in the active components used as TINA-TI$^{\mathrm{TM}}$ only supports devices available from *Texas Instruments*. Our local electronics workshop however uses equivalent devices depending on costs and availability. Furthermore, the real parts are not ideal parts as well as the laboratory environment is not ideal for measurements as there are disturbing influences such as electromagnetic coupling.

As the result of these measurement, it can be concluded that the preamplifiers are fully functional and can therefore be used for further tests. The next step towards analysing data obtained with these preamplifiers will be to parameterize the transfer spectra. With these parameterized spectra it will be possible to obtain sensor sensitivities and in the follow-up to calibrate the sensors in order to reconstruct received signals. This is not part of this work.

Chapter 10

Angular acceptance

For a possible module design it is mandatory to know the amount of sensors needed to establish a geometrical coverage sufficient for detection and positioning purposes. Therefore the angular acceptance of one piezo element glued to the inside of the module has to be obtained. For the AMs and the Acoustic Storey housing them, the ANTARES design was inherited, see Chapter 6, which allowed the use of three modules each provided with two sensors. In this design it is possible to cover 360° in the horizontal plane by six sensors leading to a minimal required angular acceptance of ±30°. With this setup, at least two sensors are triggered by a source near the horizon, as the angular acceptance of one sensor is larger than that. Provided with a comfortable overlap of the angular acceptance, this system has very good directional reconstruction capabilities.

Future OM designs exhibit a variety of conceivable solutions and prototypes for future neutrino telescopes are under study. Therefore the need for general solutions portable to many different types of modules has to be taken into account. In the simplest consideration the OAM consists of a single glass sphere interconnected to form detection-lines. In this design, a piezo element in a given module has no piezos in neighbouring modules to obtain reasonable overlap of their angular acceptance. Therefore the whole relevant sector in solid angle has to be covered by piezos in one module to gain good position determination and directivity for source direction reconstruction.

The tests performed and their results concerning the angular acceptance are shown in the next sections as well as the impact of the results to the design of OAMs.

10.1 Test module

To test the angular acceptance of piezo sensors glued to the inside of a glass sphere, the first steps are to decide which kind of piezos to use and where to glue them to the sphere. For these tests, with three available preamplifiers, it was decided to glue three piezos of different shape at different positions to one sphere. The sphere used for this procedure is a standard ANTARES glass sphere as already described in Chapter 6. After glueing, the two hemispheres forming the sphere[1] must be closed before being put into the water tank. This procedure is time consuming as it has to be done very carefully to avoid water ingress to the sphere. The ANTARES standard 12 pin *Subconn* [30] connector (*BH12*) provides a sufficient number of signal/voltage feed and readout channels. The limiting factor concerning the amount of sensors to be read out in parallel is the oscilloscope, as there are two input channels available in differential mode. Therefore the sensors are read out consecutively by changing the input channels. In this setup it is possible to measure the signals of sensors at three different angles. This reduces the amount of required mechanical handling to a minimum and minimises the effort associated with these measurements which in the big water tank are always complex and time consuming. The different piezos chosen for this test are:

- Two Piezo discs of cylindrical shape, 25.4 mm in diameter and 10 mm in thickness (25.4×10-disc), the same ones as already used in the AMs of AMADEUS;
- A Piezo disc of cylindrical shape, 25.4 mm in diameter and 20 mm in thickness (25.4×20-disc).

These samples were chosen according to the following considerations:

- The results obtained from the AMs proved that the shape of a cylindrical disk is suitable for acoustic detection;
- The calibration of the preamplifier was performed with a 47 pF capacitor substituting a 25.4×10-disc, as the preamplifier was especially designed for this type. Therefore these dimensions are most prefereable;
- The thicker piezo was chosen to study the change of angular acceptance and sensitivity depending on the thickness by keeping almost the same sensor geometry and keep the sensor still at a reasonable dimension;
- These piezos were in stock, so there was no need to order some piezos, which is quite difficult if only a small amount is needed.

As the module is to a very good approximation spherical symmetric there should be no dependence of the angular acceptance on the position of the piezo element, but the fact that it consists of two glass hemispheres might cause some difficulties, for example reflections and distortions of the signal at the glass interfaces. The first difficulty arises due to the different speed of sound in both media, water and glass. For glass one gets for the longitudinal speed of sound c_{s_l}:

$$c_{s_l} = \sqrt{\frac{E\,(1-\mu)}{\rho\,(1-\mu-2\mu^2)}} = \sqrt{\frac{64\,\mathrm{GPa}\cdot(1-0.2)}{2230\,\frac{\mathrm{kg}}{\mathrm{m}^3}\cdot\left(1-0.2-2\cdot(0.2)^2\right)}} \Rightarrow c_{s_l} = 5646.98\,\frac{\mathrm{m}}{\mathrm{s}} \qquad (10.1)$$

---

[1] According to ANTARES technical note 3-OMS-00-19-A.

with
E: Young's modulus (stiffness)
μ: Poisson's ratio (transverge to axial strain) and
ρ: Specific density at 20° C.
(All values according to the manufacturer [27].)
The speed of sound in water can be calculated, for example with the help of the *UNESCO algorithm* [26]. For the parameters at the ANTARES site, it gives about 1540.00 m/s and for the laboratory about 1470.00 m/s. The comparison of the speed of sound for glass and water results in a factor of about 3.8 in our laboratory which leads to losses due to reflexions on the glass surface. The acoustic impedances can be calculated according to:

$$Z = \rho \cdot c_{s_l}. \tag{10.2}$$

This leads to the following acoustic impedances for water (Z_W) and the glass sphere (Z_G):

$$Z_W = \rho_W \cdot c_{s_l,W} = 1000\,\frac{\mathrm{kg}}{\mathrm{m}^3} \cdot 1470.00\,\frac{\mathrm{m}}{\mathrm{s}} = 1.47 \cdot 10^6 \frac{\mathrm{Ns}}{\mathrm{m}^3}, \tag{10.3}$$

$$Z_G = \rho_G \cdot c_{s_l,G} = 2230\,\frac{\mathrm{kg}}{\mathrm{m}^3} \cdot 5646.98\,\frac{\mathrm{m}}{\mathrm{s}} = 12.59 \cdot 10^6 \frac{\mathrm{Ns}}{\mathrm{m}^3} \tag{10.4}$$

and therefore to a reflectivity of:

$$r = \frac{Z_G - Z_W}{Z_G + Z_W} = 0.79. \tag{10.5}$$

On the other hand, sound coupled to the glass propagates very fast inside the glass of the sphere. Therefore the acoustic sensor receives not only a single sound signal, it actually receives a superposition of the original soundwave and some time delayed waves propagating on a longer path through the glass. Or if the sensor is turned away with respect to the line between the emitter and the centre of the sphere, the "original" signal can be later. In these superpositions there are destructive and constructive interferences, attenuating or enhancing the signal. This complicates the signal determination as the time delays are rather short due to the high speed of sound in the glass. Also resonant oscillations are excited in the glass. Another uncertainty may be caused by the interface of both hemispheres, where the sound wave has to "jump" from one hemisphere to the other.

Taking into account the points mentioned above, it was decided to glue the sensors to the following positions (for illustration see Figure 10.1):

- The first 25.4×10-disc is glued at 10.0° below the equator, which is the interface of both hemispheres, corresponding to about 3.6 cm on the inner circumference. This is close to the interface in order to determine its influence on the directionality. The sensor is labelled "ch0";
- The second 25.4×10-disc is glued at 36.5° below the equator corresponding to about 12.9 cm on the inner circumference. This distance from the equator is comparable to

the AM design of 45° but has the advantage of being not a multiple of 15°, which will be the stepsize of the measurement, therefore allowing to measure a different set of angles for both sensors. This sensor is also shifted 90° in azimuth to separate the two sensors. The sensor is labelled “ch1”;

- The 25.4×20-disc is glued on the pole, maximising the distance to the equator. The sensor is labelled “ch2”.

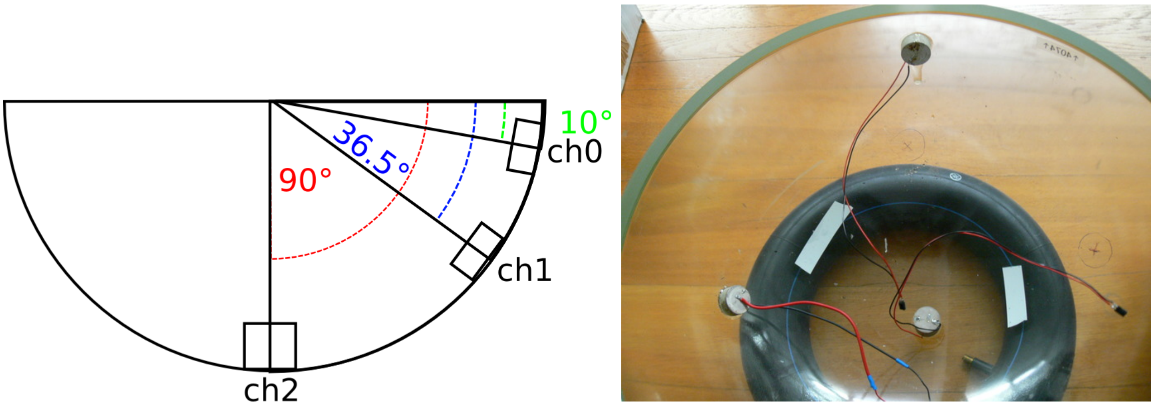

Figure 10.1: Left: Schematic of the sensor positions in the test module. Right: Sensors glued inside the sphere with cables soldered to them.

After connecting all cables for sensor feeding and readout, see Section 10.2, the module is closed. Afterwards the module is mounted to its support structure in such a way that the pole with the third sensor is pointing downwards and the equator is parallel to the floor, as seen in Figure 10.2 (left). This mounting may look unfavorable as the weight mounted under the support structure is totally covering the piezo at the pole (see Figure 10.2 (right)). Furthermore one disc of the support totally covers the second 25.4×10-disc. But as the scope of the following measurement is not to prove whether the piezos are sensitive to direct exposure to sonic waves or to determine their absolute amplitude but rather to determine to which angle still reasonable signals can be received, this mounting is an adequate solution. Anyway it is not possible to keep the module free floating in the tank and therefore there will always be parts of the support structure covering subareas of the module for some positions of the emitter.

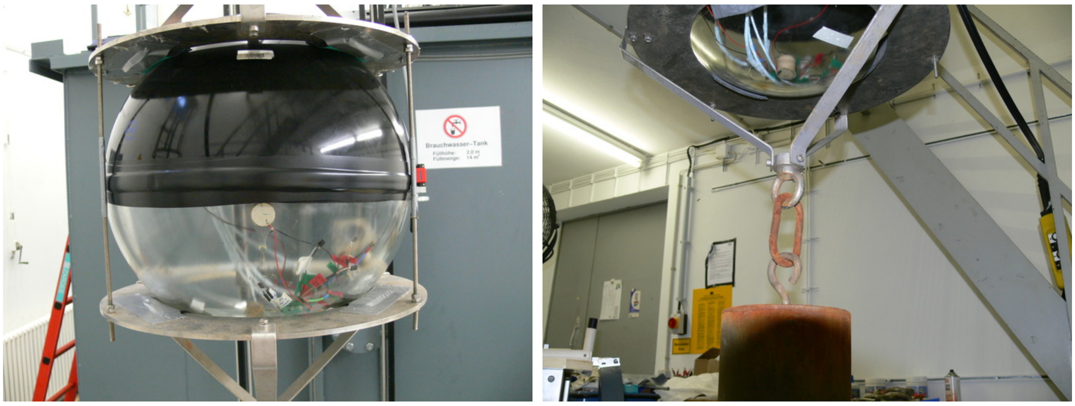

Figure 10.2: Left: Module mounted to its support structure. Right: Weight hanging from the support structure, shadowing the piezo at the south pole for signals coming from below.

10.2 Test setup

To measure the characteristics of the test module a test setup suitable for the measurement is created. Preferably not only suitable for this single measurement but for a variety of possible future tests and measurements. Therefore some considerations have to be taken into account:

- Find a way to properly power and read out the channels and keep this cabling as flexible as possible in order to perform any changes or extentions without soldering anew the affected cables and connectors;
- Determine the range of interest in azimuth and polar angle for the acceptance measurement and how this range can be covered with a minimum effort;
- Find the right emitter-receiver distance
    - far enough to ensure a homogeneous sound field and to minimise shadowing effects due to the support structure;
    - close enough to ensure that the received signal is almost undistorted by any reflections on the tank surfaces;
- Chose an emission signal which is adapted to the specified purpose.

.

10.2.1 Cabling

For the AM measurements, as the AMs only contain two sensors, it is sufficient to use the standard 12 pin *Subconn* connector and to use separate lines for both sensors. That means both powering and readout of each sensor are connected by a separate set of cables as it is done in AMADEUS. In this case eight[2] out of twelve pins are used which still leaves two additional connections as spares. The last two pins are connectd to the two shieldings of the cable. For this test involving three sensors, this scheme implies that at least one power supply of the sensors has to be shared between two sensors. However as it is planned to execute some further tests on this type of combined module the cabling has to fulfill some additional requirements. Future tests including a high voltage power supply (HV-PS) for the PMT to study the effect of high voltage generation and in the follow-up including a fully functional PMT result in the following requirements:

- Enable the readout of up to three acoustic sensors by only changing the signal cables instead of all cables belonging to the sensor or even opening and closing the sphere;
- Maintain the possibility to separately power the acoustic sensors and an additional element such as a PMT HV-PS;

---

[2] Voltage and ground in addition to signal +/- for both sensors

- Allocate a maximum number of readout channels to simplify further test setups;
- Enable a correct connection of the PMT for further tests, therefore in principle inherit the ANTARES cabling as close as possible.

The last point is the most difficult requirement to meet as the PMT itself uses ten out of twelve pins[3], see Figure 10.3. The remaining two pins feed the LED pulser in the OM used for calibration purposes. In principle, with this kind of 12 pin connector, it is possible to operate the fully connected PMT without LED pulser in addition to one acoustic sensor, if the sensor is powered by one of the PMT voltages (48 V or $1.25\,\mathrm{V} - 3.75\,\mathrm{V}$[4]) or a voltage derived from those. However some of the pins are not essential for proper operation of the PMT, for example the connections to dynode 12, dynode 14 or anode (at least one of them is needed but not all three of them), so there are a couple of possible pin combinations available for the tests without constraining the use of existing ANTARES equipment. The cabling as shown in Figure 10.3 therefore was used as a guideline, but in order to keep the cabling as flexible as possible the end parts like PMT, piezos or their preamplifiers are not soldered directly to the cable. Instead, short pieces of cable are soldered to them which in turn are soldered to connectors which can be easily connected to matching connectors at the end of the OM cables. The resulting interchangeability is exactly what is needed for the successful measurements with different module settings.

Pin	Function
6	0V
7	48V
8	Shield
4	PMT HV monitor
5	PMT HV adjust
2	PMT Dynode D12
3	ground
1	shield
11	PMT Anode
12	PMT Dynode D14
9	Ground LED
10	LED +

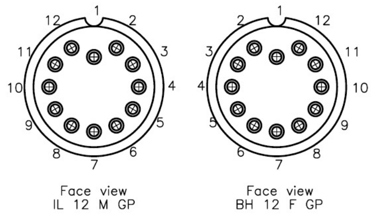

Figure 10.3: OM connector power scheme.

For the angular acceptance measurements presented in this chapter there is no need for different voltages being supplied to the module as only the preamplifiers of the three

---

[3] According to ANTARES technical note 3OMS-02-05D.

[4] These low voltages are used to adjust the HV of the PMT.

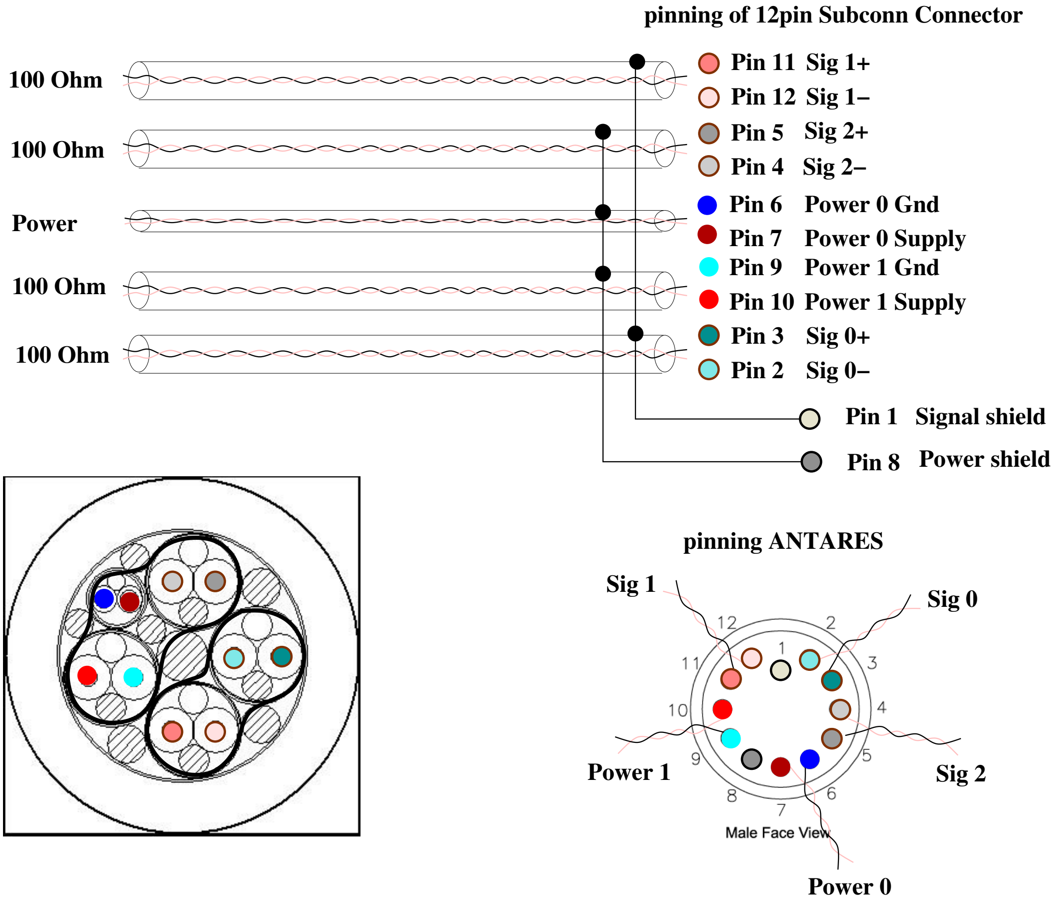

Figure 10.4: AM cabling scheme. Cables with 100 Ω impedance were originally foreseen for signal readout from the OMs. The bottom left diagram shows the cross section of the OM cable. The thick black loops indicate the conjunction of the shields for their connection to pin 1 and pin 8, respectively.

piezos have to be powered and read out. This is achieved by applying 9 V to the Power 0 pins (cf. Figure 10.4) and then distribute this voltage to the three preamplifiers inside the sphere by an internal fanout. The readout channels are connected according to the cabling of AMs [31], to Sig 0, Sig 1 and Sig 2 (see also Figure 10.4).

10.2.2 Angular range of the measurement

The information about the angular acceptance of a sensor is obtained by covering 180° in azimuthal and polar direction starting from the sensor position. The acoustic irradiation of the remaining sections of the module should be equivalent as the used piezo discs are cylindrical symmetric. Thus less coverage would also be sufficient. Detailed information on the covered ranges will be given in Section 10.3.

10.2.3 Mounting of the emitter

Azimuthal mounting

The Azimuthal mounting of the sphere is equal to the one used in Chapter 7 allowing a full 2π coverage. Two possible variants arise from this constellation:

- Mounting of the sender to the working plate of the tank as described in Chapter 7 at a fixed distance;
- Mounting of the sender to one of the support discs with the help of a lever arm to fix the distance.

The first possibility, which worked very well for the AM measurements is not preferable in the case of changing polar angles. The adjustement of sender depth and distance to the module is quite complicated and an additional source of errors and reaching the pole regions of the module is impossible in that case. Therefore the second option is chosen as here depth and distance are only determined by the lever arm and the disc allows good determination and fixing of the azimuthal angle.

Polar mounting

The rotating axis for the polar angle lies in the equatorial plane of the sphere perpendicular to the longer side of the water tank in order to take advantage of the existing space in this direction. This axis causes a set of difficulties which have to be solved or circumvented by the mounting. These problems are:

- The mounting itself can not be rotated as it is pulled underwater by a weight and held in its position by the crane; therefore the emitter has to be adjusted. In the previous section it was pointed out that the sender has to be mounted to a support disc so it is neccessary to construct a frame to adjust the sender at the requested position, see Figure 10.5;
- The axis lies in the equatorial plane of the sphere but the support discs are in the bottom and top region of the sphere. The frame has to shift the emitter mounting point into this plane, see Figure 10.6;
- The top pole region of the sphere is unreachable as the chains of the crane get in the way of the sender. This constitutes no obstacle as there is no reason to get in this region as even the first sensor is shifted by 10° and it is not foreseen to measure to an extend of 100° in that direction. The completed frame is shown in Figure 10.7.

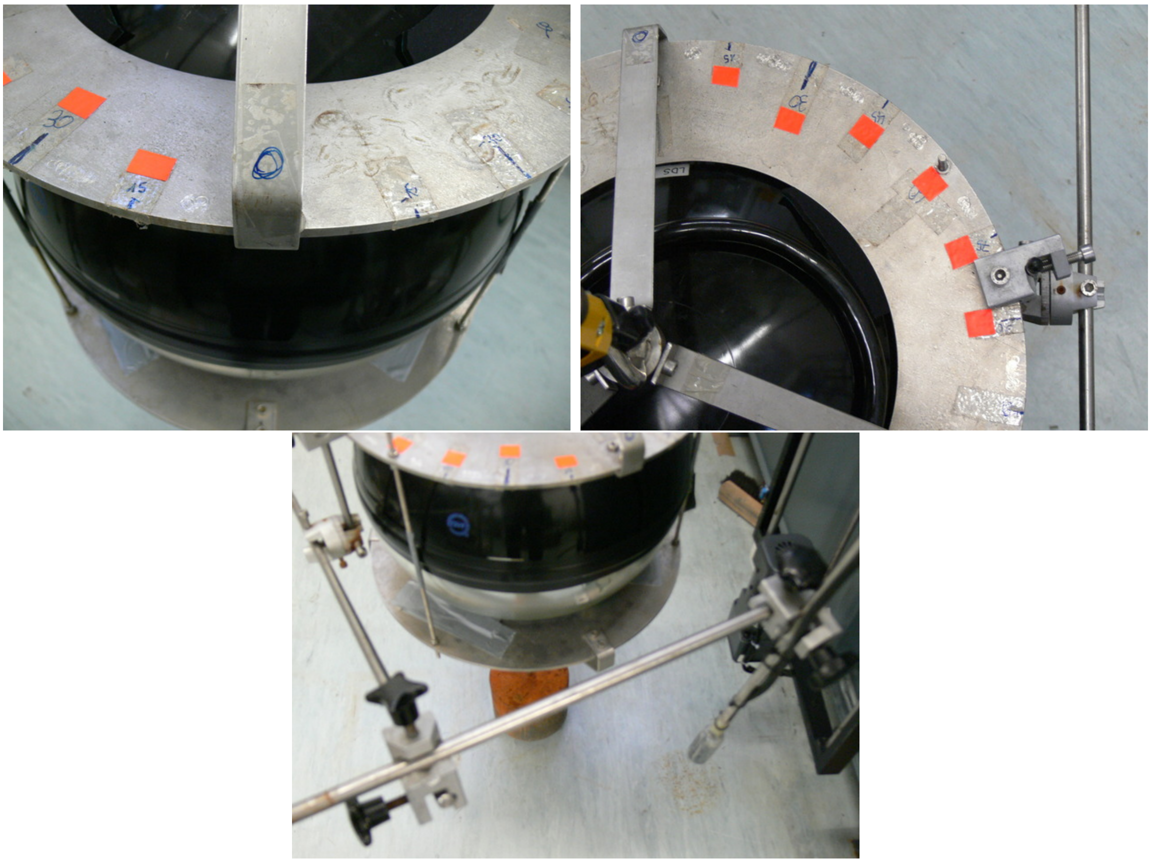

Figure 10.5: Top left: Support disc with adjustment scale. Top right: Azimuthal adjustment mounted on the disc.
Bottom: Appearance of the complete frame. For better visualisation, the radial distance of the emitter from the sphere is scaled down with respect to the distance used for the measurement.

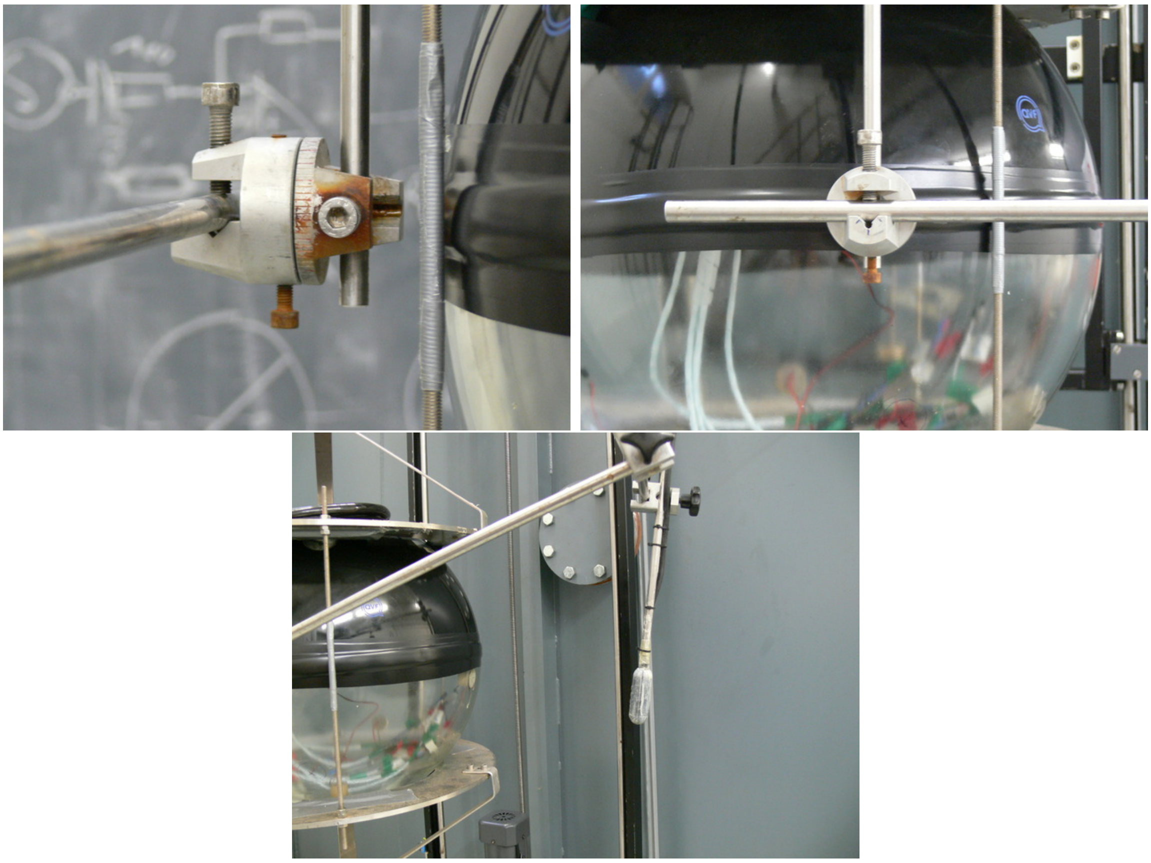

Figure 10.6: top left: Polar rotating axis in the equatorial plane (head on), top right: Polar rotating axis in the equatorial plane (sideways)
bottom: Emitter facing ch0 at $\varphi = 90^\circ$ and $\vartheta = 90^\circ$.

Figure 10.7: Complete test setup with the radial distance of the emitter from the sphere scaled down with respect to the distance used for the measurement.

Radial mounting

To determine the optimal emitter-receiver distance the aforementioned items have to be considered.

- The minimum distance is given through the dimensions of the support structure and especially its weight. As it is planned to move the sender around this weight, the lever arm has at least to be so long not to get in the way of the weight. This means it has to be at least 70 cm long (coincident to the wavelength of an acoustic signal at ≈2 kHz). This also gives the required distance for the sound field;
- The maximum distance is given through the dimensions of the tank. As in the uppermost position of the sender, near the top pole, the sender should still be completely covered with a sufficient amount of water, the lever arm should not exceed 1.1 m. This distance also avoids distortions of the signal due to reflections.

To come along with this points the distance is chosen to be 1 m, coincident with the reference point of the emitter strength.

10.2.4 Emitted signal

For the angular acceptance of the piezo elements only the time series of a signal is analysed as it is sufficient to know how the amplitude evolves depending on the incident angle. Therefore the emitted signal is chosen to be the ramp signal as the resulting neutrinolike bipolar pulse shows good capability concerning amplitude measurement. As the distance is multiplied by four with respect to the measurements in Section 7.1, the ramp signal also has to be raised. Therefore its amplitude is raised to 8 V.

10.3 Measurement

For the measurement the emitter is mounted to the upper support disc. As the three sensors are at different positions and only relative directions are taken into account, ch0 is taken as reference. Angles adjusted for this sensor are translated to the according ones providing a set of different angles for each sensor. For the sensor mounted to the pole of the sphere it is in principle not neccessary to define an azimuthal angle as there should be no dependency at this position but for consistency and visualising purposes ch1 and ch2 are chosen to have the same azimuthal angle. This is done without loss of generality and just as the sensors are read out consecutive, this results in only a renaming in azimuthal direction for all sensors. The origin of the coordinate system for each sensor is chosen according to the following suggestions:

- The origin of the azimuthal angle lies 90° away from the sensor centre. Therefore at $\varphi = 90°$ the emitter is facing the sensor directly. The sensors ch0 and ch1 are shifted by an additional 90° in their positions. To cover a range of 180° for every sensor, an effective covered range of 270° is measured:

  - from $\varphi = -90°$ to $\varphi = +180°$ for ch0;
  - from $\varphi = 0°$ to $\varphi = +270°$ for ch1 and ch2;

- The origin of the polar angle also lies 90° away from the sensor centre in the same way as above, giving an emitter axis parallel to the sensor surface for $\vartheta = 90°$. The range is chosen in that way to cover at least the range from $\vartheta = 0°$ to $\vartheta = 180°$ for ch1. As the sensors have different polar positions their incident angle has to be calculated by removing 26.5° (ch1) or 80° (ch2) respectively from the reference angle. This gives the following effective ranges:
  - from $\vartheta = 0°$ to $\vartheta = 210°$ for ch0;
  - from $\vartheta = -26.5°$ to $\vartheta = 183.5°$ for ch1;
  - from $\vartheta = -80°$ to $\vartheta = 130°$ for ch2;

For every sensor more than 180° in azimuth and polar angle are covered which is sufficient to determine the angular acceptance due to the symmetry of sensors and glass sphere. The module and the emitter are moved with a crane on top of the water tank where the cables connecting the module to power supply and oscilloscope are connected. A custom build extention with a length of 1.25 m is used, which is neccessary as the standard OM output cable is only 1 m long with high rigidity. The latter alone would render the deployment of the module to the needed depth or the span of the whole azimuthal range impossible.

The three preamplifiers are supported with 9 V by an external power supply. The standard values are used for the oscilloscope settings, as this procedure is comparable to the AM measurements. The procedure for the measurement is as follows:

- Adjust the polar angle, whose adjustment is more complicated than the azimuthal one due to the long lever arm. In order to minimise the efforts and the errors resulting from this procedure the former angle is kept constant while varying the latter one;
- Adjust the azimuthal angle on the support disc;
- Deploy the module with the crane to the required depth;
- Emitt signals and record the emitted and received signal for the connected sensor while averaging over 250 sweeps;
- Change the sensors by switching the corresponding coaxial cables;
- Recover the module and change the azimuthal angle by 15°.

This procedure is repeated until all measurements are taken for the adjusted polar angle. Then this angle is changed by 15° and the procedure is repeated until all combinations are completed. Figure 10.8 on the top left shows the ramp signal sent to the emitter. This signal is totally included in the trigger signal, emitted from the waveform generator to the oscilloscope. Therefore the trigger starting point is not identical to the emission of the

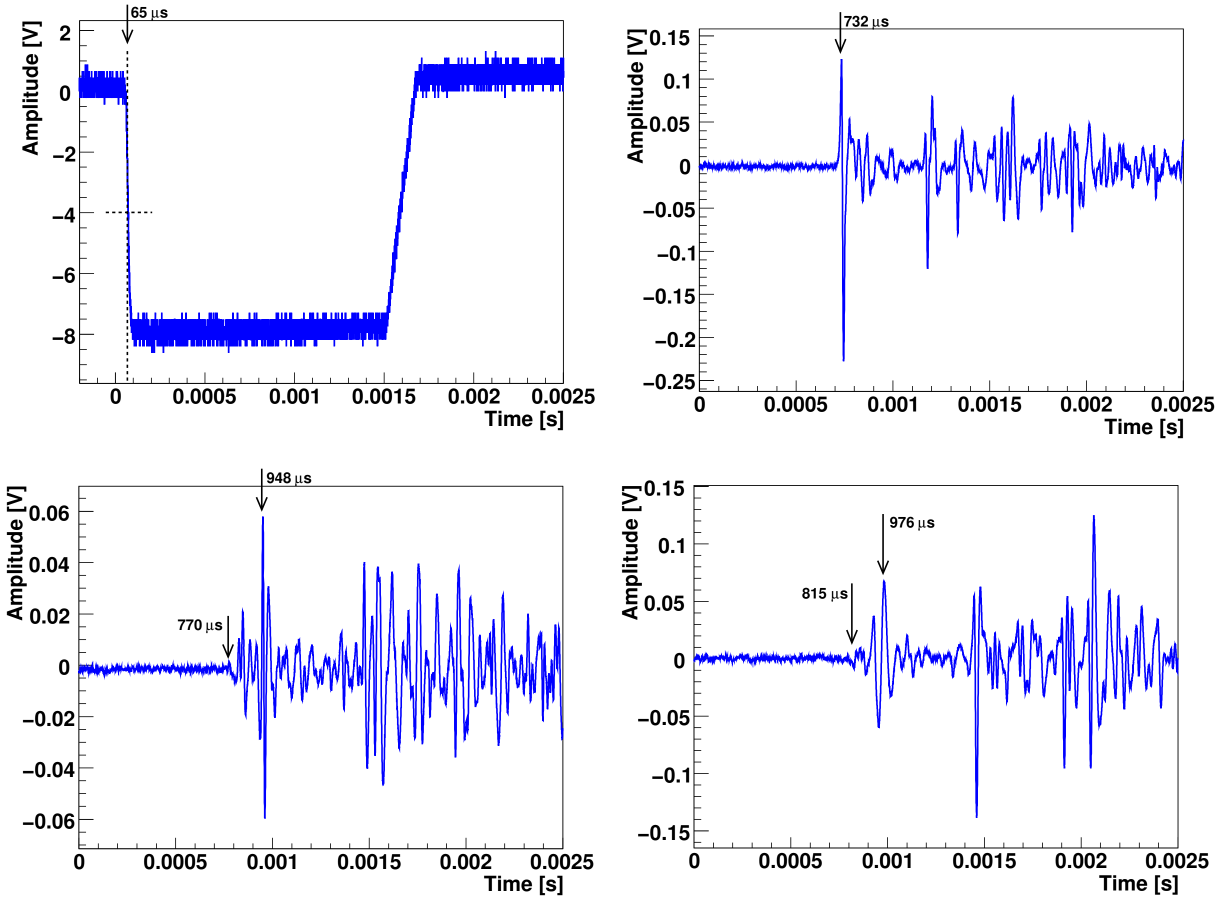

Figure 10.8: top left: Ramp signal emitted by the waveform generator, top right: ch0 with $\varphi = 90°, \vartheta = 90°$, bottom left: ch1 with $\varphi = 120°, \vartheta = 3.5°$, bottom right: ch2 with $\varphi = 165°, \vartheta = -35°$. These examples are further described in the text.

soundwave generated by the emitter. The reasonable offset of the trigger and soundwave starting point is given in this Figure as the point in time when the ramp signal reaches half of its amplitude. In this case after 65 µs. For ch0, Figure 10.8 on the top right shows the response of the module to direct exposure of sonic waves. The signal arriving first at the sensor is of clearly visible bipolar shape. The arrival time (assuming the time of the maximum as arrival time) corresponds to a distance $\mathrm{d}_{\mathrm{ch0\_max}}$ of:

$$\mathrm{d}_{\mathrm{ch0\_max}} = (\mathrm{t}_{\mathrm{arrival,ch0\_max}} - \mathrm{t}_{\mathrm{offset}}) \cdot \mathrm{c}_{\mathrm{s_l,W}} = (732\,\mu s - 65\,\mu s) \cdot 1470\,\frac{\mathrm{m}}{\mathrm{s}} = 0.98\,\mathrm{m}. \qquad (10.6)$$

This distance is in accordance with the requested distance of 1 m considering the uncertainties arising from the mounting of the emitter and the fact that the time of the maximum is only an approximation of the signal arriving time. Oscillations of the piezo as well as time delayed superimposed signals can easily be separated. This results in a good signal amplitude determination. On the bottom left the signal is shown for ch1 and a different set of angles as described in the caption. The arrival time of the signal is increased, according to the changed distance.

$$\mathrm{d}_{\mathrm{ch1\_max}} = (\mathrm{t}_{\mathrm{arrival,ch1\_max}} - \mathrm{t}_{\mathrm{offset}}) \cdot \mathrm{c}_{\mathrm{s_l,W}} = (948\,\mu s - 65\,\mu s) \cdot 1470\,\frac{\mathrm{m}}{\mathrm{s}} = 1.30\,\mathrm{m}. \quad (10.7)$$

In this case, the determination of the signal amplitude is influenced by the superposition of different signals travelling through the glass. The maximum peak occurs 178 µs after the first arriving signals. Thus the signal amplitude is not the real arriving amplitude but a result of the interference of all participating signals coming from the piezo and from the sphere. On the bottom right of Figure 10.8, the signal is shown for ch2 and incident angles described in the caption. The signal shape is no more like a single bipolar pulse for this set of angles. The shift of the signal with respect to the arrival time and the occurrence of maximum and minimum peak is comparable to the one described for ch1. In this case:

$$\mathrm{d}_{\mathrm{ch2\_max}} = (\mathrm{t}_{\mathrm{arrival,ch2\_max}} - \mathrm{t}_{\mathrm{offset}}) \cdot \mathrm{c}_{\mathrm{s_l,W}} = (976\,\mu s - 65\,\mu s) \cdot 1470\,\frac{\mathrm{m}}{\mathrm{s}} = 1.34\,\mathrm{m}, \quad (10.8)$$

and the occurrence of the maximum 161 µs after the first visible signals.

10.4 Results

The recorded data are moved to the ECAP computing network where they are analysed by the program already described in Section 2.1. The fit-region is adjusted to the distance of 1 m and the whole data set is processed. To discuss the results some considerations have to be taken into account. The first one is the background of about 0.07 V, visible in the resulting Figures for ch0 and ch1 described below. For ch2 the background has a value of about 0.1 V due to the higher sensitivity of this sensor. Therefore only amplitudes significantly above this level are considered useful. The second one is the fact that the distance from the emitter to the sphere is kept constant at 1 m. Therefore the emitter-receiver distance is varying depending on the incident angle between 1.00 m for $\varphi = 90°$, $\vartheta = 90°$, about 1.23 m for $\varphi = 180°, \vartheta = 180°$ and about 1.42 m for $\varphi = 270°, \vartheta = 90°$, as can be seen in Figure 10.8. The sound attenuation arising from the different distances is negligible on the measured scale. As the program to analyse these data obtains the amplitude by fitting Gaussian functions to the maximum and minimum value in a specified time window, this window has to be enlarged to handle the different arrival times. It opens between 525 µs and 1.28 ms after the trigger signal with an expected signal after 615 µs for 1 m distance. This enlarged time window in addition to the amount of visible signals and oscillations in the glass render the determination of the signal amplitude difficult for the different sets of angles. The applied program is not able to separate these signals, therefore it is possible that the maximum value of a signal is not directly followed by its minimum value as expected for a bipolar pulse (see also Figure 10.8). This leads to uncertainties concerning the determination of the amplitude as maximum and minimum might belong to different signals. These uncertainties manifest in the unstable curve progressions.

The resulting curves for ch0 are shown in Figure 10.9. For $\varphi < 0°$ the signal lies in the background and therefore the amplitude almost vanishes independent of the polar angle. The same result is obtained for $\varphi > 165°$. In the range from $\varphi = 0°$ to $\varphi = 165°$ the ϑ-dependency is obtainable, showing similar behaviour as in the azimuthal plane, as expected from geometry arguments. Between $\vartheta = 15°$ and $\vartheta = 150°$ the signal is clearly visible in the data. The influence of the interface can be studied by comparing equidistant sets of polar angles counted from the centre of the sensor:

- $\vartheta = 90° \pm 15° \Rightarrow \vartheta = 75°$ and $\vartheta = 105°$. These two curves show almost no difference in amplitude. This behaviour can be explained by looking at the geometry of the module. For $\vartheta = 75°$ the sender lies only 5° above the equator, therefore a significant part of the sonic wave "hits" the sender without the need to travel through the glass in order to generate the signal. This is the same for the coresponding angle below the equator;

- $\vartheta = 90° \pm 30° \Rightarrow \vartheta = 60°$ and $\vartheta = 120°$. Here the upper signal has only about 60% of the lower signals amplitude. The shape of the curve is the same for both signals;

- $\vartheta = 90° \pm 45° \Rightarrow \vartheta = 45°$ and $\vartheta = 135°$. Here the result is similar to the one above, showing a deviation of about 60% in the signals amplitude;

- $\vartheta = 90^\circ \pm 60^\circ \Rightarrow \vartheta = 30^\circ$ and $\vartheta = 150^\circ$. For these curves it is difficult to determine the influence of the interface, as for this angles the presence of the support discs also effects the recorded signal due to reflexions on its surface. This manifests in the smearing of the curve for $\vartheta = 150^\circ$ compared to most of the other curves.

For this sensor, an acceptance of about 75° is achieved both in azimuth and polar angle. The influence of the interface is visible and may be scope of further investigations concerning the effect on source reconstruction.

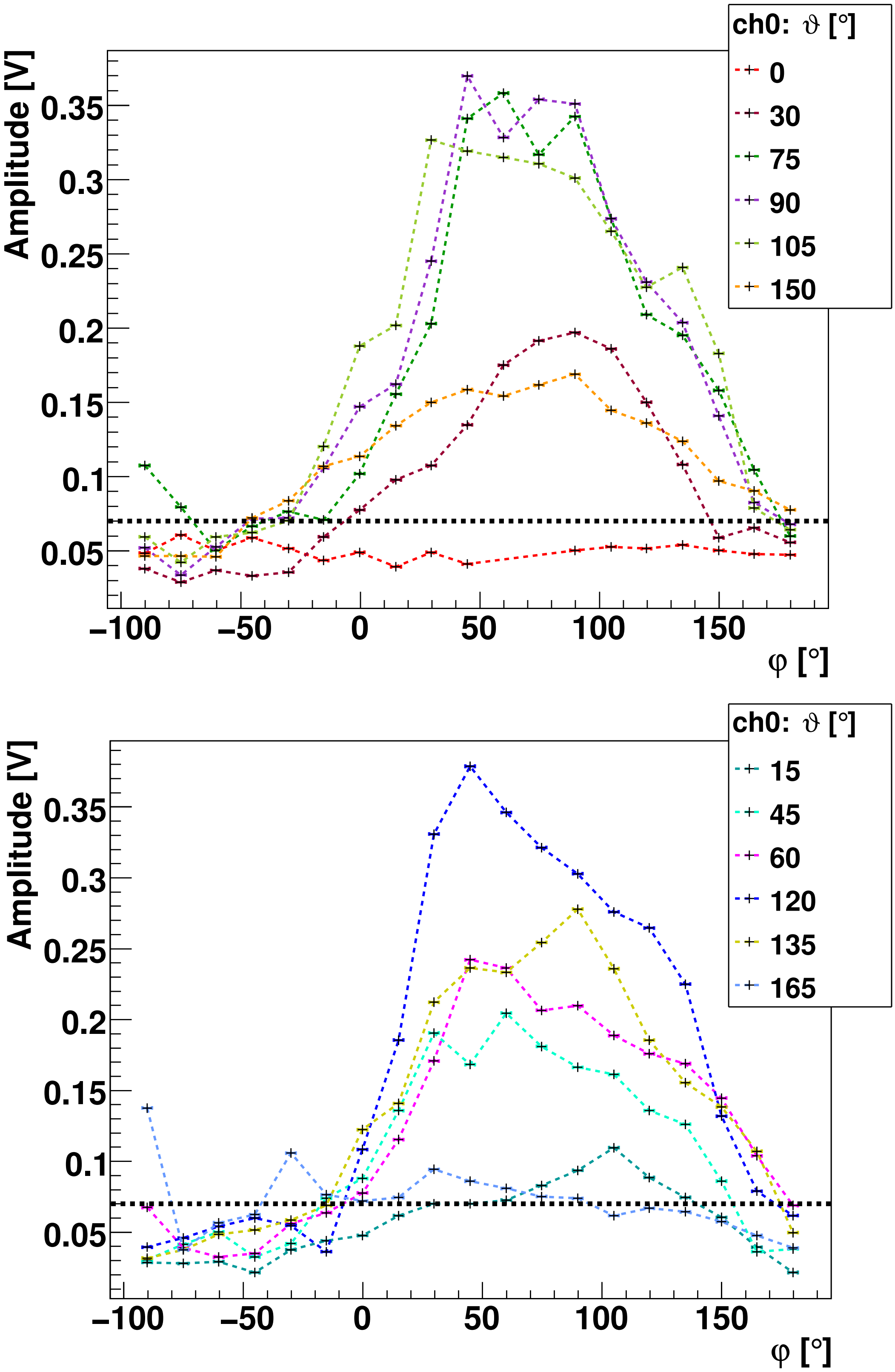

Figure 10.9: ch0: Obtained curves for different incident angles, whereas the dashed lines are only to guide the eye. The black dashed line shows the estimated background of 0.07 V. The plots are further described in the text.

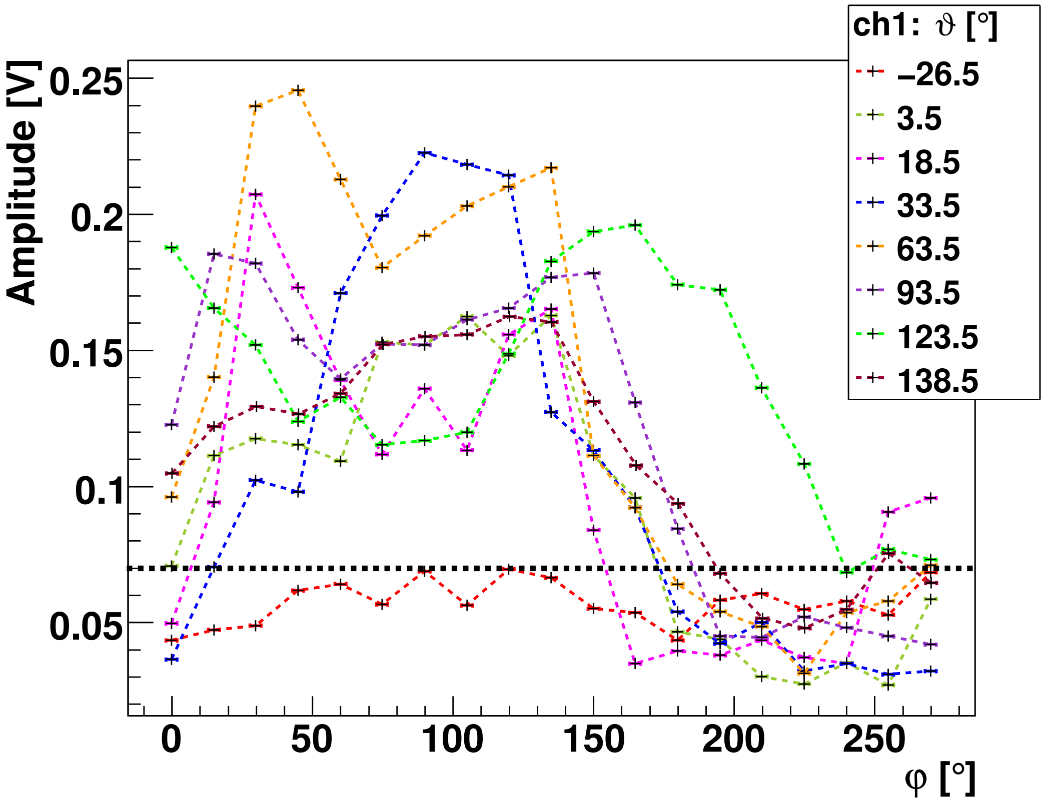

Figure 10.10: ch1: Obtained curves for different incident angles, whereas the dashed lines are only to guide the eye. The black dashed line shows the estimated background of 0.07 V. The plot is further described in the text.

The results for ch1 are shown in Figure 10.10. The curve progressions for this plot are not as clear as for ch0. The influence of the support structure covering this sensor is visible for almost every curve. It manifests in the smearing of the curves already mentioned for ch0, the occuring "dips" for angles around 90° and the strange behaviour of single curves like the one for $\vartheta = 123.5°$. In addition the shielding accounts for the in total lower amplitudes. Besides these deviations, the general conclusion from the plot is the same as for the aforementioned one. In the range from $\varphi = 0°$ to $\varphi = 165°$ and between $\vartheta = 3.5°$ and $\vartheta = 138.5°$ the signal is clearly visible in the data. The influence of the interface can not be studied here, as the lower angle of the equidistant sets of polar angles counted from the centre of the sensor is shielded by the weight. For this sensor, the same acceptance of about 75° is achieved both in azimuth and polar angle as expected.

The results for the third sensor, ch2, are shown in Figure 10.11. As expected, the amplitude in the azimuthal plane is almost constant, except some features corresponding to support structures. Depending on the incident angle, these structures cause maximum or minimum amplitudes as they are shifted by 60° between the region above or below the discs. Clearly visible comparing the curves for $\vartheta = 10°$ (below the disc) and $\vartheta = 40°$ (above the disc). One effect of the different piezo element shape is an increase of about 30% in

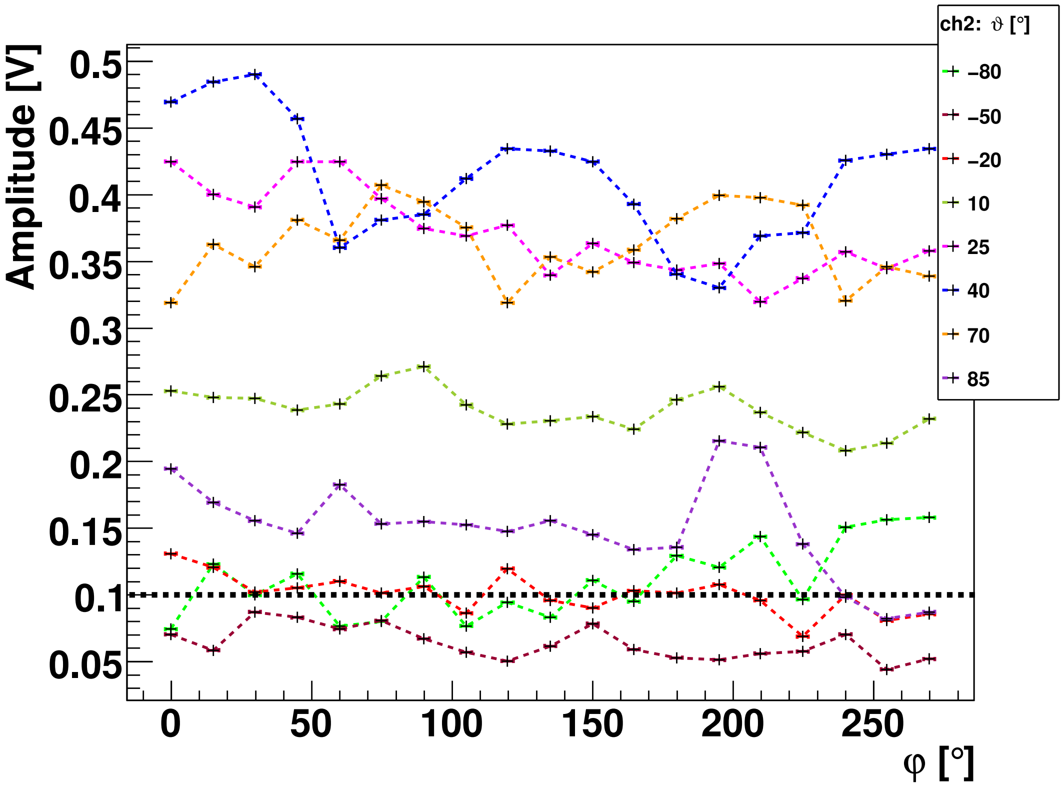

Figure 10.11: ch2: Obtained curves for different incident angles, whereas the dashed lines are only to guide the eye. The black dashed line shows the estimated background of 0.1 V for this sensor. The plot is further described in the text.

amplitude compared to ch0. For the acceptance the result is comparable to the other ones, as for $\vartheta > 25°$ the curves are clearly separated from the others, except for $\vartheta = 85°$ where the sensor is completely covered by the weight. For $\vartheta = 10°$ the amplitude lies in between all other amplitudes. This behaviour may be caused by leaving the angular acceptance or by reflexions on the disc. The fact that the shape of the curve is still comparable to other curves might be a hint that this measurement reached the edge of the angular acceptance! In that case, the acceptance is about 80° which is in good agreement to the other sensors applying a stepsize of 15°.

As a result from these measurements, the amount of used sensors in one module should be at least three. With this amount a sufficient overlap is gained for achieving good signal reconstruction capablities.

Chapter 11

Opto-acoustic sensor crosstalk

For a combination of different electronic devices in one housing, it is mandatory to know in which way they are influencing each other. Highly sensitive devices may be affected by others in a way rendering simultaneous operation impossible. Electronic devices possibly affecting the acoustic detection in an opto-acoustic combination are:

- The high voltage for PMT operation and its generation;
- The low voltage power supply for the DAQ hardware and its conversion to different voltages (DC-DC converters);
- The PMT itself when taking data.

The first two points are discussed in this chapter. The last point will be investigated if the performance of the other measurements is satisfactory enough to justify the efforts arising from careful mounting and operation of the PMT besides the acoustic sensor(s) and working in a dark room.

11.1 Crosstalk with the PMT HV power supply

In this section the effect of high voltage generation inside the sphere on the inherent acoustic sensor noise is discussed. For this purpose a standard ANTARES PMT high voltage power supply (HV-PS) is put in the same hemisphere together with an acoustic sensor including its preamplifier. The PSD of the noise data obtained in a combined operation is compared to the PSD of the data obtained without the HV-PS.

11.1.1 Utilised Hardware

Acoustic device

The acoustic device chosen for this test is the hemisphere already used for the angular acceptance measurements. This hemisphere already houses three operational sensors and allows for the measurement of two different piezo dimensions (25.4×10 and 25.4×20) without additional efforts. Only one preamplifier is used to minimise the amount of affected or interacting elements.

PMT high voltage power supply

The PMT HV-PS used for this test is a "*PHQ 7081-20 Integrated High Voltage Supply for PMT 7081-20*" with serialnumber 371036 from *iseg Spezialelektronik GmbH* [32]. It is identical to the ones used in the OMs in the ANTARES experiment. To test the functionality small cables are soldered to the HV-PS in order to meet the requirements described in Section 10.2.1. Figure 11.1 and Figure 11.2 show the schematic and the corresponding picture of the HV-PS. The HV-PS is designed to supply the PMT with an anode voltage $\mathrm{U_A}$ varying between 1300 V and 2300 V. $\mathrm{U_A}$ is a composition of voltage between dynode 1 and cathode (GND), $\mathrm{U_{D_1C}}$, which adds to about 800 V ± 5% and the voltage between anode and dynode 1, $\mathrm{U_{AD_1}}$, adjustable between 500 V and 1500 V. This adjustment is done by an input set voltage, $\mathrm{U_{AD\_SET}}$, variable between 1.25 V and 3.75 V internally multiplied by a factor of 400 giving the aforementioned voltage range. This voltage can be monitored by the output monitor $\mathrm{U_{A\_MON}}$. This voltage is identical to $\mathrm{U_{AD\_SET}}$ in normal mode but only shows values if the system is operating correctly. The HV-PS is powered by the stabilised 48 V power supply[1] "*ES 075-2*" from *Delta Elektronika BV* [33] and an additional power supply providing $\mathrm{U_{AD\_SET}}$.

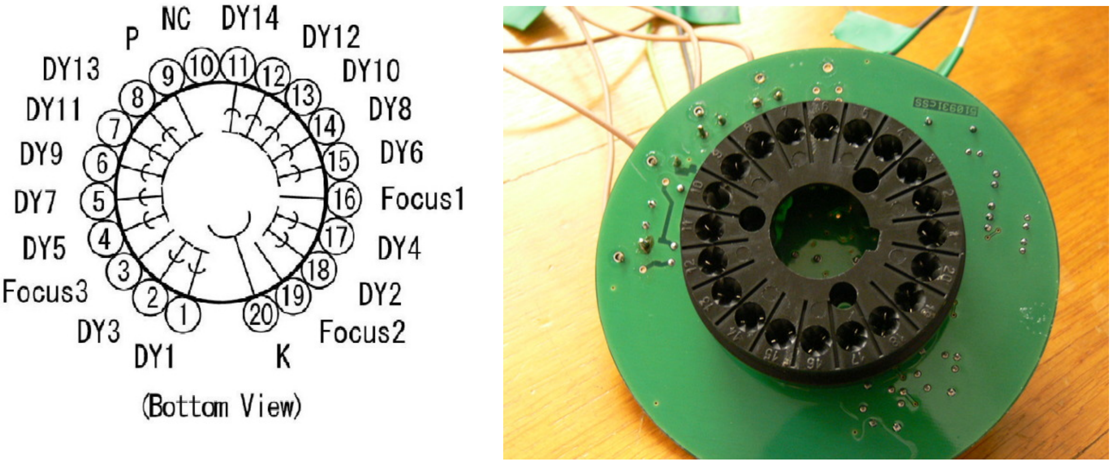

Figure 11.1: left: Bottom view of the PMT base, according to ANTARES technical note 3-OMS-06-01-A , right: Photo of the HV-PS back side with wholes for PMT connection.

---

[1] In ANTARES the PMT base is feed through the LCM by 48 V

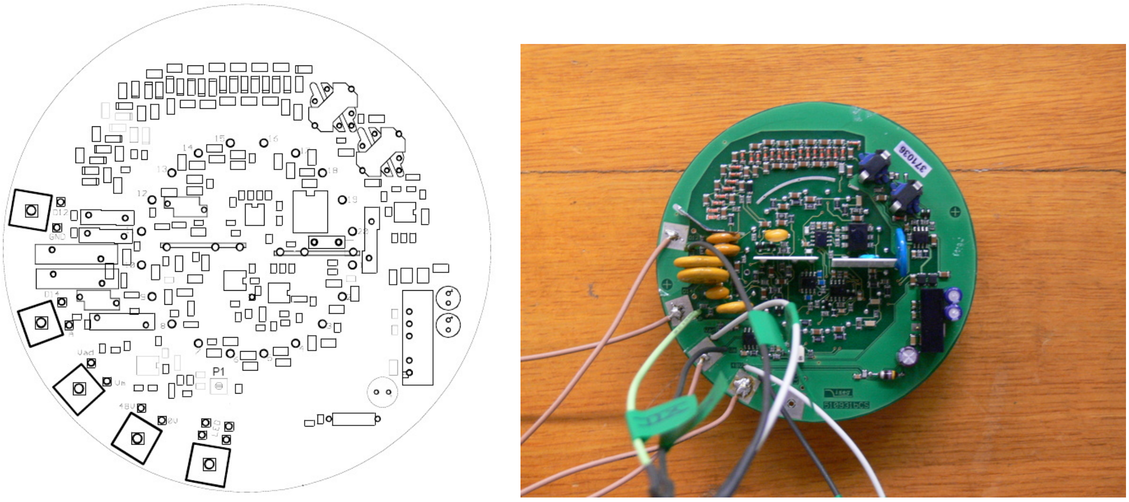

Figure 11.2: left: Schematic of the HV-PS front side according to iseg, right: Photo of the HV-PS front side with cables soldered to it.

According to the manufacturer two series of measurements are recommended to test the functionality:

- The linearity of the anode voltage, varying $\mathrm{U}_{\mathrm{AD\_SET}}$ from 1.25 V to the maximum value of 3.75 V in steps of 0.25 V corresponding to an increase of $\mathrm{U}_{\mathrm{AD}_1}$ of 100 V for each measurement;
- The intermediate voltages on the different dynodes, setting $\mathrm{U}_{\mathrm{AD\_SET}}$ to 3.0 V and measuring the different voltages between the different electrodes and cathode (GND). The intermediate voltages are obtained by substraction of the consecutive electrode voltages.

The measurements concerning high voltage are performed with a static digital volt meter "*HEINZINGER DVM 65*" from *Heinzinger electronic GmbH* [34], capable of handling high voltages with a precision of $1 \cdot 10^{-4}$ absolute ± 1 digit. The result of these measurements is shown in Figure 11.3 for the linearity compared to manufacturer's data and in Figure 11.4 for the intermediate voltages compared to manufacturer's data and the ANTARES specifications. The nomenclature of the electrodes[2] is given in Table 11.1. These results confirm the correct connection and functionality of the HV-PS.

---

[2] According to ANTARES technical note 3-OMS-06-01-A

Electrode number	**Connection**
1	Dynode 1
2	Dynode 3
3	Focus 1
4	Dynode 5
5	Dynode 7
6	Dynode 9
7	Dynode 11
8	Dynode 13
9	Anode (A)
10	Not connected (NC)
11	Dynode 14
12	Dynode 12
13	Dynode 10
14	Dynode 8
15	Dynode 6
16	Focus 3
17	Dynode 4
18	Dynode 2
19	Focus 2
20	Cathode (K)

Table 11.1: Electrodes of the HV-PS and corresponding connections.

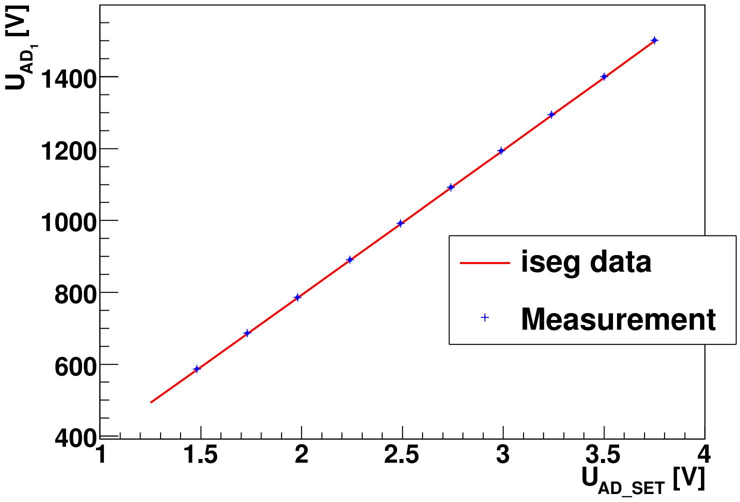

Figure 11.3: Linearity of the anode voltage.

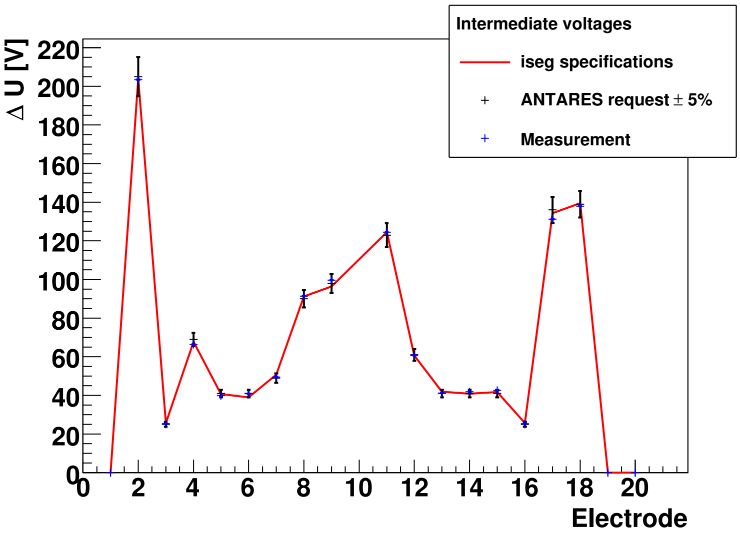

Figure 11.4: Intermediate voltages of the different dynodes. For nomenclature see Table 11.1.

11.1.2 Test setup

For the test setup, the opened test module is put on a table and both hemispheres are placed on air tubes or rubber foam to decouple these parts from vibrations and to fix their position, see Figure 11.5. As already discussed above the cabling is inherited from former measurements making it neccessary to put both hemispheres close enough together to connect all cables. In this setup the HV-PS can be put inside the hemisphere housing the sensors for combined tests as well as to remove it to test the single acoustic sensor. The required channels for the acoustic sensor, two for the power supply and two for the differential signal, are obtained by using the redundant channels for the LED pulser and the dynode 12 and dynode 14 signals. The setup is powered by three independent power supplies: the stabilised 48 V supply for the HV-PS, a 9 V supply for the preamplifier and an adjustable power supply for the input set voltage, $\mathrm{U_{AD\_SET}}$. $\mathrm{U_{A\_MON}}$ is monitored via a dedicated digital multi meter (DMM). The two differential signal lines are connected via coaxial cables to two channels of the oscilloscope.

Figure 11.5: Hemispheres placed next to each other on an airtube and rubber foam.

11.1.3 Measurement

For the measurements, the inherent noise of the three piezo elements including their preamplifiers is recorded consecutive every 100 ms for 2000 sweeps. The noise sample itself has a lenght of 50 ms. The first measurement is performed with the HV-PS totally disconnected and placed outside the hemisphere, see Figure 11.6 (left). This defines the reference for a totally undistorted acoustic sensor except for the laboratory environment. In the next step, the HV-PS is placed inside the hemisphere next to the acoustic sensors but without direct contact except through the glass, see Figure 11.6 (right). It is totally connected and supplied with 48.00 V whereas $\mathrm{U_{AD\_SET}}$ is set to 0.00 V. This is verified with $\mathrm{U_{A\_MON}}$ which also measures 0.00 V. Therefore no high voltage is set, as in this case $\mathrm{U_{D_1C}} = 0.00\,\mathrm{V}$ as well as $\mathrm{U_{AD_1}} = 0.00\,\mathrm{V}$. For the last two measurements $\mathrm{U_{AD\_SET}}$ is set to 1.25 V and 3.75 V, therefore minimum and maximum voltage are set respectively.

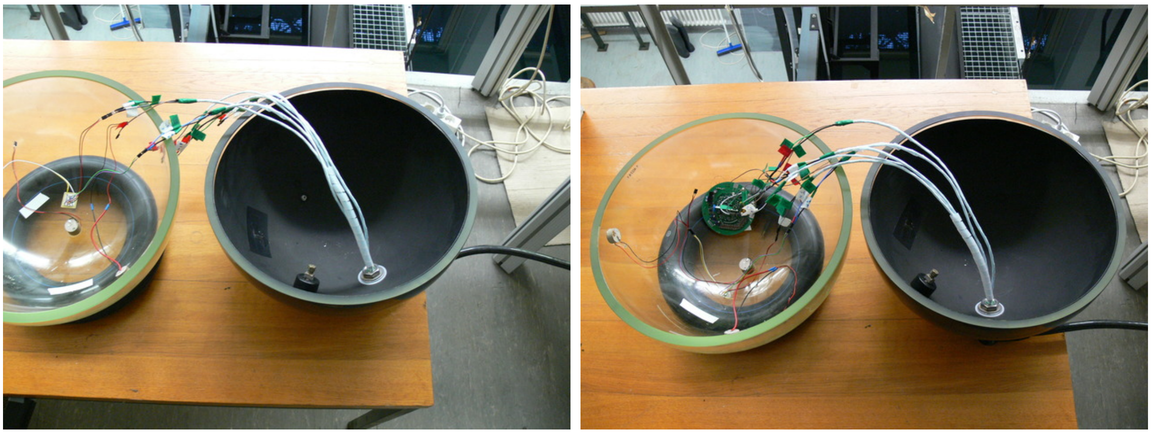

Figure 11.6: left: Noise measurement without the HV-PS, right: Noise measurement with the HV-PS.

11.1.4 Results

The result for the single sensors is shown in Figure 11.7. Sensors ch1 and ch2 show similar behaviour whereas ch0[3] shows a higher noise level in all frequency ranges with a maximum deviation of only 2 dB in the lower frequency range up to 3.5 kHz. The reason for that might be a higher vulnerability to external noise for this sensor. This deviation of 2 dB causes no complications as it is within the limits of the biased errors of these measurements. The fact that the sensors are not moulded in a copper tube as the AM sensors as well as the long unshielded connections make this setup vulnerable for internal, as well as external electromagnetic coupling. If the compatibility of both detection methods is approved even though this weak protection against electromagnetic coupling, further improvements can be achieved by effectively shielding all electronic parts. The curve progressions for all three sensors in principle follow the amplitude response of their preamplifier with its bandpass characteristics. The discrepancy for the lower frequency range arises from the limited resolution of the measurements lowering its accuracy. The most prominent differences to the ideal band pass characteristics are two wide peaks in the frequency range from 45 kHz to 120 kHz. These peaks are most likely caused by the piezos themselves.

The result for the HV-PS powered with 48 V next to the sensors but without generating high voltage is shown in Figure 11.8. In this plot the three sensors are almost identical. That means that the noise recorded with ch1 and ch2 is raised to the level of ch0 which remains in principle the same. Remarkable changes with respect to Figure 11.7 are the occurring spikes with integer multiple frequencies of about 46 kHz, marked with arrows in Figure 11.8. These spikes are most likely caused by DC-DC conversions inside the HV-PS without generating high voltage on the connections.

---

[3] For the labelling of the acoustic channels, see Section 10.1.

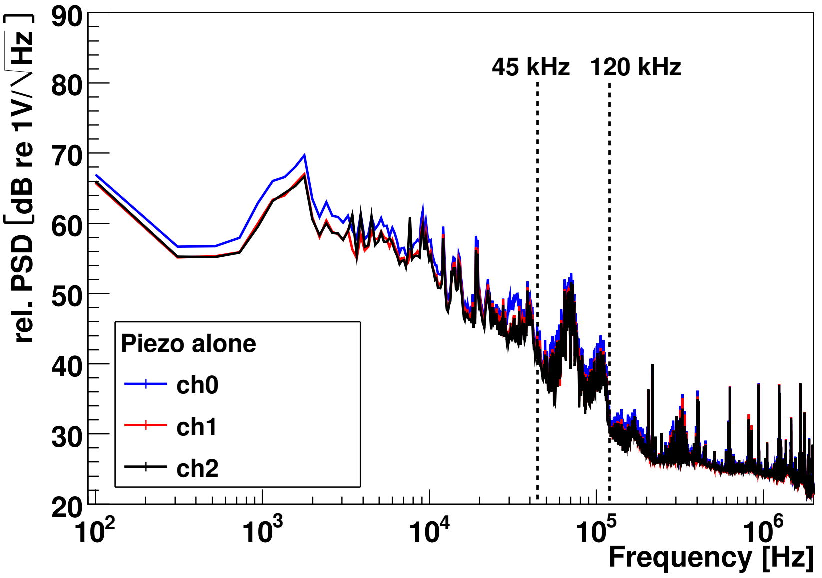

Figure 11.7: Combined ambient and inherent noise in the laboratory recorded by the acoustic sensors powered by a dedicated power supply without HV-PS. The plot is further described in the text.

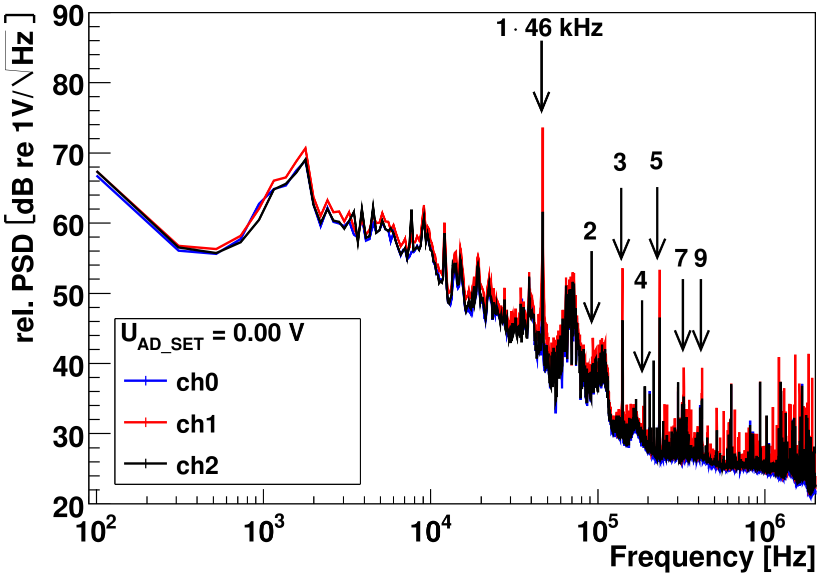

Figure 11.8: Combined ambient and inherent noise in the laboratory recorded with $\mathrm{U_{AD\_SET}} = 0.00\,\mathrm{V}$ and separated power supply. The numbers on the arrows give the multiples of 46 kHz as shown for n=1. The plot is further described in the text.

The first set of data with applied high voltage is shown in Figure 11.9. The ambient noise level for all three sensors remains almost at the same level as without the high voltage. Exceptions from this behaviour are:

- The rising noise for frequencies above 400 kHz;
- The excess between 9 kHz and 12 kHz for ch0;
- The additional clearly visible spike at a frequency of about 190 kHz and additional ones at multiples of this frequency.

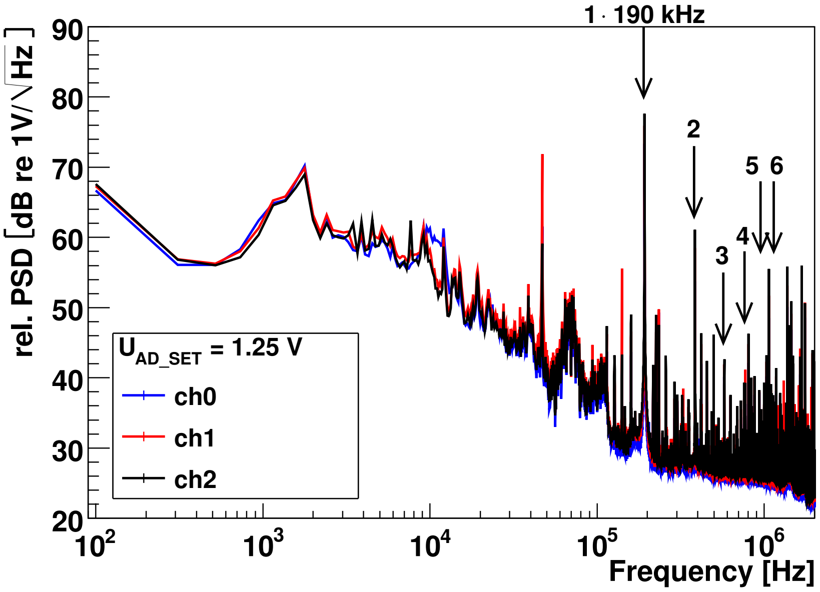

Figure 11.9: Combined ambient and inherent noise in the laboratory recorded with U_{AD_SET} = 1.25 V and separated power supply. The numbers on the arrows give the multiples of 190 kHz as shown for n=1. The plot is further described in the text.

The occurring excess for ch0 could be an indiction for a coupling loop in the cable as this feature is only visible for one sensor. The additional spikes are caused by the DC-DC conversion of the applied high voltage.

The effect of raising the high voltage is shown in Figure 11.10. In this plot the indicated excess of ch0 in Figure 11.9 is clearly visible for all three sensors in the frequency range from about 5 kHz to about 13 kHz. This might be an effect of changing the sensors as this leads to different cable positions. In the remaining frequency ranges, the raised high voltage manifests in a rise of the aforementionned spikes and the noise above 400 kHz.

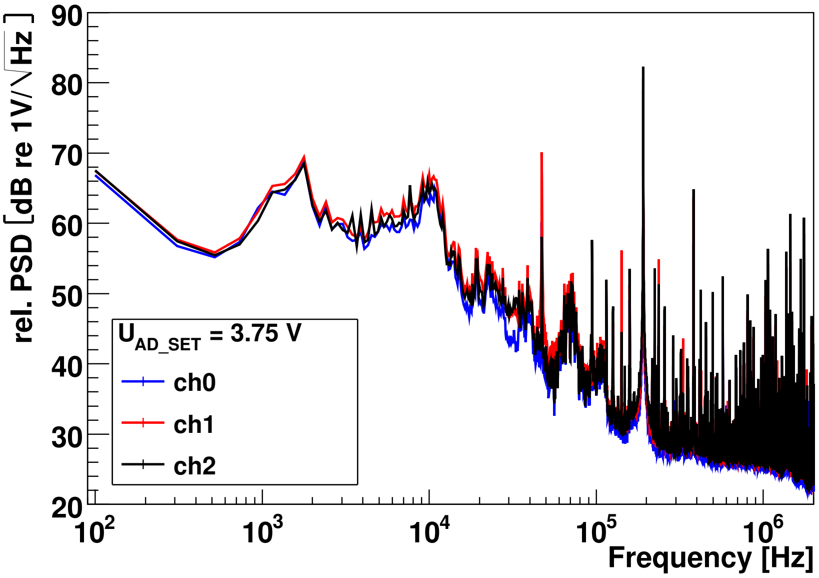

Figure 11.10: Combined ambient and inherent noise in the laboratory recorded with $U_{AD\_SET} = 3.75$ V and separated power supply. The plot is further described in the text.

To sum it up, Figure 11.11 shows the difference for ch0 between the noise recorded without HV-PS and the noise recorded with applied 2300 V. With a mean of about 0.9 dB and a RMS of about 2.9 dB, the overal influence of the HV-PS to the obtained noise data is negligible. The distribution is not Gaussian, therefore the influence of systematics has to be studied. As first conclusions the effects of the HV-PS on the acoustic sensors in this test can thus be described in the following way:

- In the low frequency regime below 5 kHz no significant variation is obtainable;
- Between 5 kHz and 13 kHz an excess reaching about 10 dB is clearly visible. This excess is most likely caused by coupling loops in the cables, therefore can be shielded effectively;
- In the frequency range from 13 kHz to about 400 kHz the common ambient noise level is again almost negligible except some significant peaks
  - located at integer multiple frequencies of about 46 kHz;
  - located at integer multiple frequencies of about 190 kHz;

  caused by the DC-DC conversion. By adjusting the HV-PS for higher frequency switching, this peaks can be removed from the frequency range of interest;
- For frequencies above 400 kHz the common inherent noise level is raised due to the applied high voltage. As acoustic particle detection only takes place up to 100 kHz the detection capabilities are unaffected by this raise.

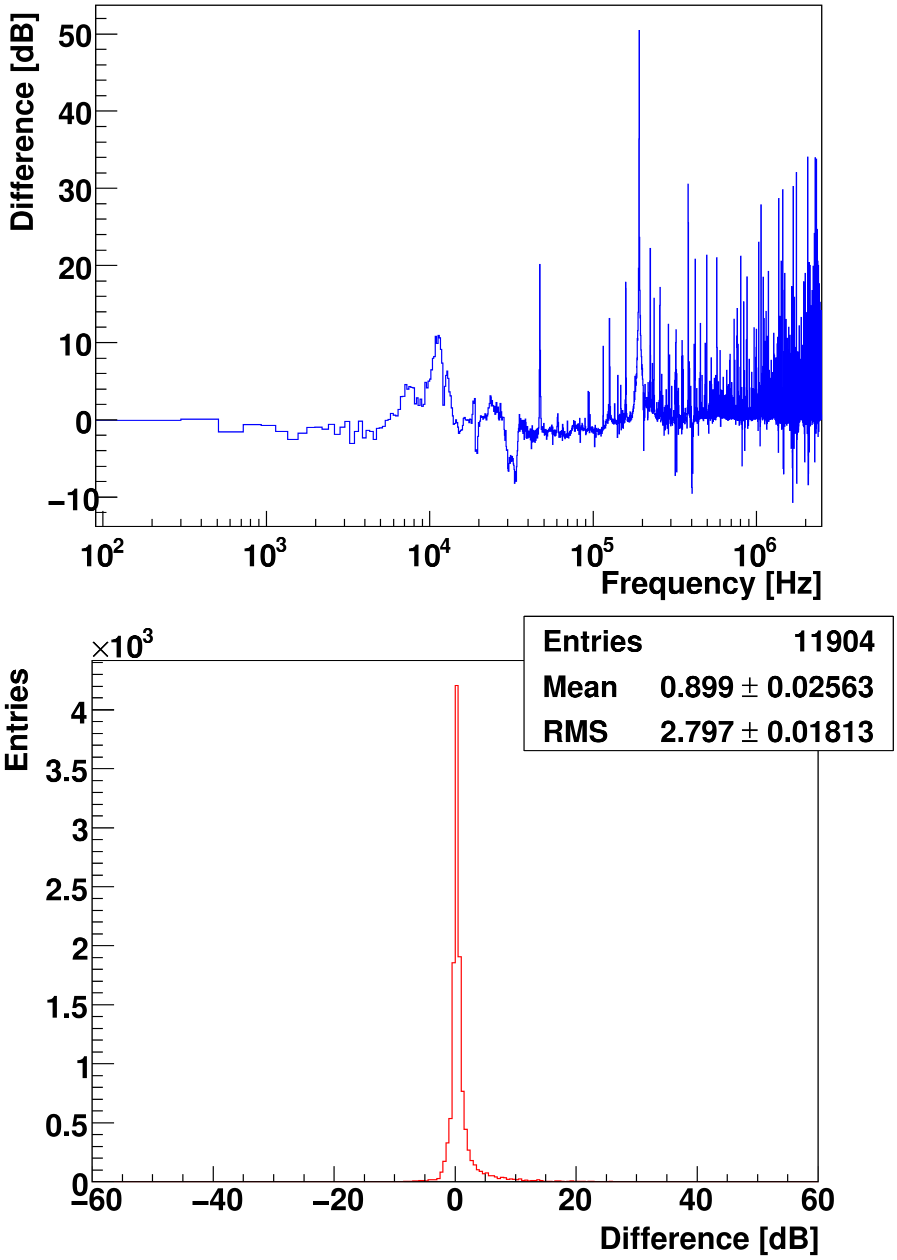

Figure 11.11: top: Difference of the recorded noise with applied 2300 V and without HV-PS for ch0 and separated power supply, bottom: Distribution of the data. The plots are further described in the text.

11.2 Impact of a combined power supply

The setup discussed in the former section holds the possibility of combining both detection techniques in an OAM in a way of totally splitting the involved sensors both in power supply and in signal processing. To simplify a future detector design it would be reasonable to power the module with only one supply voltage and derive all other needed ones from the main voltage, as already done in ANTARES. Thus in this section the effect of a combined power supply is studied.

11.2.1 Test setup

The test setup as well as the devices used for the tests are identical to the ones described in Section 11.1. The only difference in both setups is the removal of the dedicated power supply of the acoustic sensors. The 48 V supply voltage is connected to a splitter inside the hemisphere where it is feed to the HV-PS and in parallel to an DC-DC converter. This DC-DC converter, type “TMR 4812” from TRACO ELECTRONIG AG [35], converts the input voltage of 48 V to an output voltage of 12 V connected to the preamplifier matching its power requirements (instead of 9 V used in the last section. This raised supply voltage has no effect on the preamplifier performance). The switching frequency of this DC-DC converter, located in the range between 100 kHz and 650 kHz, is not perfect as it is located next to the frequency range of interest for acoustic particle detection.

11.2.2 Results

The result for the sensors powered by the DC-DC converter and without the HV-PS is shown in Figure 11.12. In this case for all three sensors almost the same noise is recorded. The band pass characteristics is observable as well as the two piezo caused peaks in the frequency range from 45 kHz to 120 kHz. Compared to the data obtained with separate power supplies, two major changes occur:

- In the frequency range from about 7.5 kHz to about 13.0 kHz an excess of about 5 dB to 7 dB is observable. This excess is comparably to the one visible in Figure 11.9 and Figure 11.10, although it is more pronounced in this case. Explainable by the additional amount of cables, their changed positions and the resulting coupling loops;
- Above 100 kHz the noise level is raised by about 10 dB compared to the noise level obtained in Figure 11.7. This might be a consequence of the switching frequency of the DC-DC converter operating in this frequency range.

Another point is the fact that in this case the noise level for ch0 is below the noise level for ch1 and ch2 in contrast to the measurements performed in the last section. This fact strengthens the aforementioned higher vulnerability of ch0 to external noise as the measurements were performed on different days. The influence of the presence of the HV-PS is shown in Figure 11.13. Here the general noise level is raised by about 3 dB to 7 dB

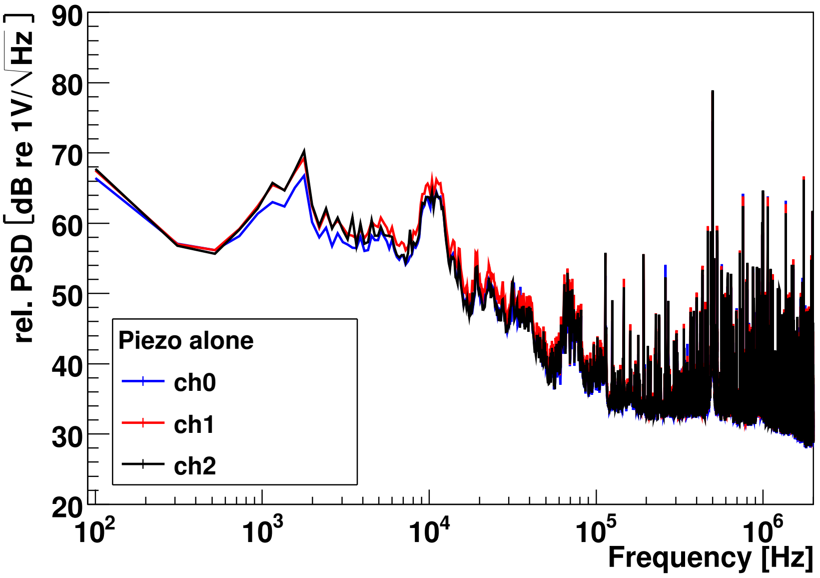

Figure 11.12: Combined ambient and inherent noise in the laboratory recorded by the acoustic sensors without HV-PS and combined power supply. The plot is further described in the text.

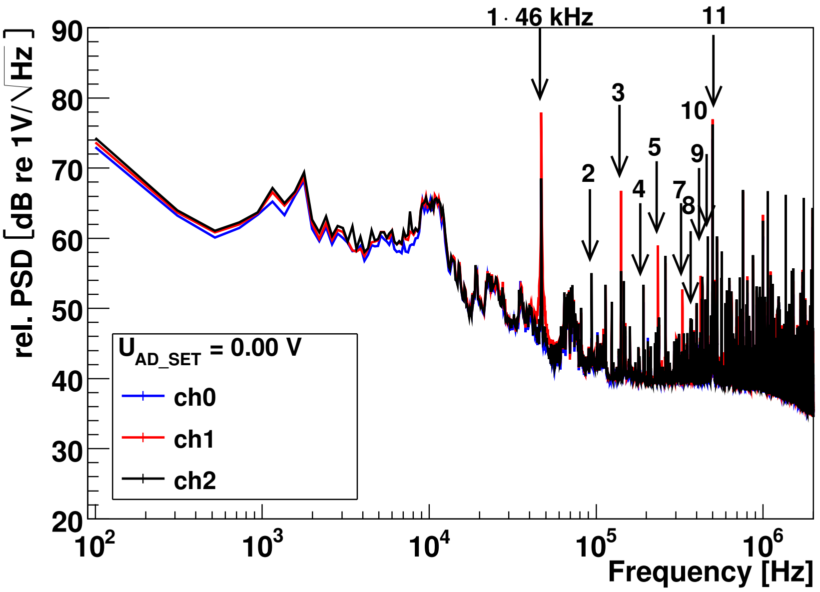

Figure 11.13: Combined ambient and inherent noise in the laboratory recorded with $U_{\mathrm{AD\_SET}} = 0.00\,\mathrm{V}$ and combined power supply. The numbers on the arrows give the multiples of 46 kHz as shown for n=1. The plot is further described in the text.

with respect to Figure 11.12. In addition, peaks located at integer multiple frequencies of about 46 kHz appear identical to the ones appearing with separate power supplies. As before only two sharp peaks occur below 100 kHz.

Generating high voltage leads to the noise spectrum shown in Figure 11.14. The variations compared to Figure 11.13 are limited to the arising peaks located at multiple frequencies of 190 kHz and an intensification of the existing peaks. The overall noise level is unaffected by the high voltage generation.

The difference of the obtained noise spectrum for ch0 with $U_{AD\_SET} = 3.75\,V$ and without the HV-PS is shown in Figure 11.15. The described peaks are visible in Figure 11.15 (top) as well as the overall shift of about 5 dB in Figure 11.15 (bottom). This shift is caused by the presence of the powered HV-PS and the DC-DC converter without generating high voltage.

The spectra recorded for ch0 with separated and combined power supply are shown in Figure 11.16 for $U_{AD\_SET} = 3.75\,V$. To better visualise the changes occuring from the combined power supply, Figure 11.17 shows the difference of both spectra. The raise of the noise level is visible in the data distribution as well as in the direct comparison of both, leading to a shift of about 13 dB.

To draw conclusions it can be stated that there are significant effects of combining acoustic sensors with a HV-PS and their combined power supply in these tests. Most of these effects take place at frequency ranges not interesting for acoustic particle detection but have to be studied as well for further investigations. The large effect of the combined power supply with a shift in the overall noise level of about 13 dB is no real drawback as the ambient noise in ANTARES is of the same order greater than the inherent noise. In addition, this setup is not a realistic design as it is possible to separate power supplies derived from a main voltage to a great extent. This is already done in ANTARES. The small effects of combining the acoustic sensors with a HV-PS are only limited to single frequencies and can be treated especially. The usage of devices optimised for acoustic detection, for example HV-PS or DC-DC converter with higher switching frequencies, can significantly reduce these effects. For a future detector design a combined power deduction has to be devised where all problems can be solved.

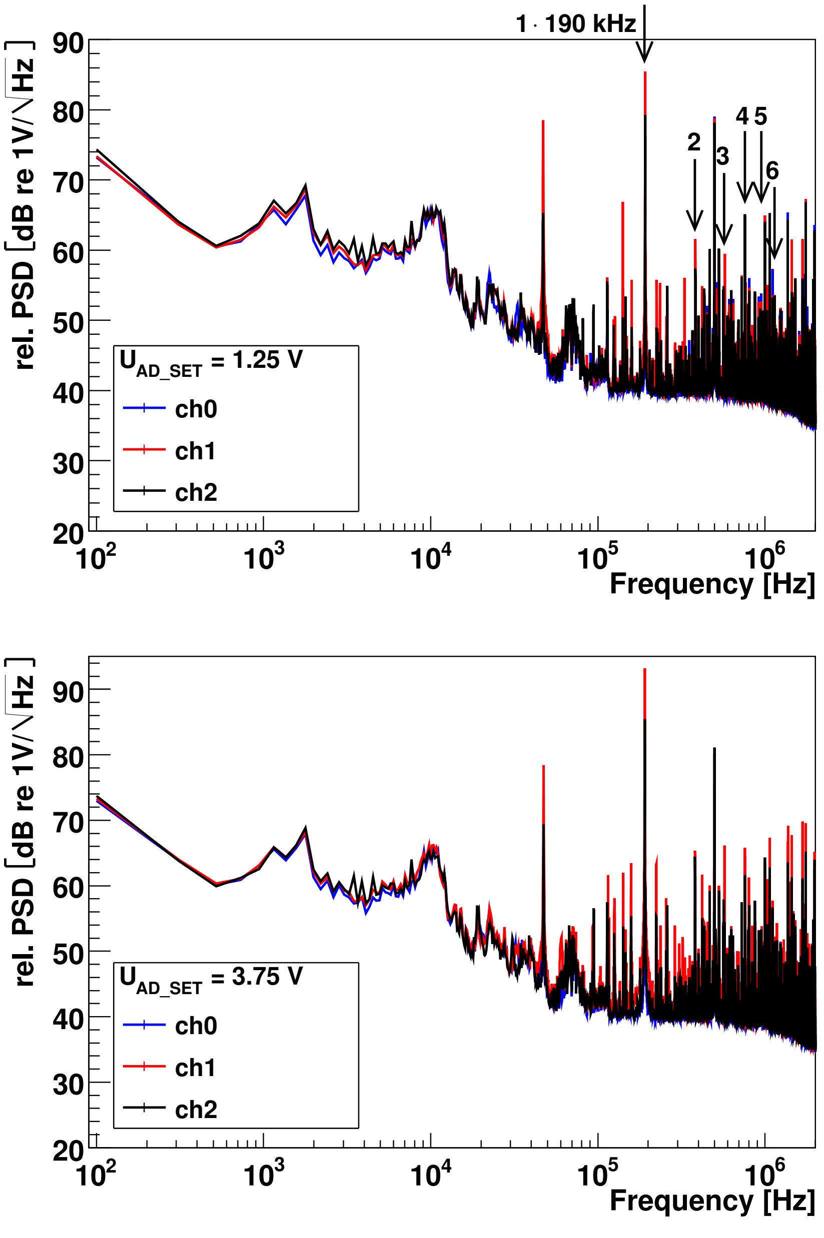

Figure 11.14: Combined ambient and inherent noise in the laboratory recorded with $U_{AD\_SET} = 1.25\,V$ (top), $U_{AD\_SET} = 3.75\,V$ (bottom) and combined power supply. The numbers on the arrows give the multiples of 190 kHz as shown for n=1. The plots are further described in the text.

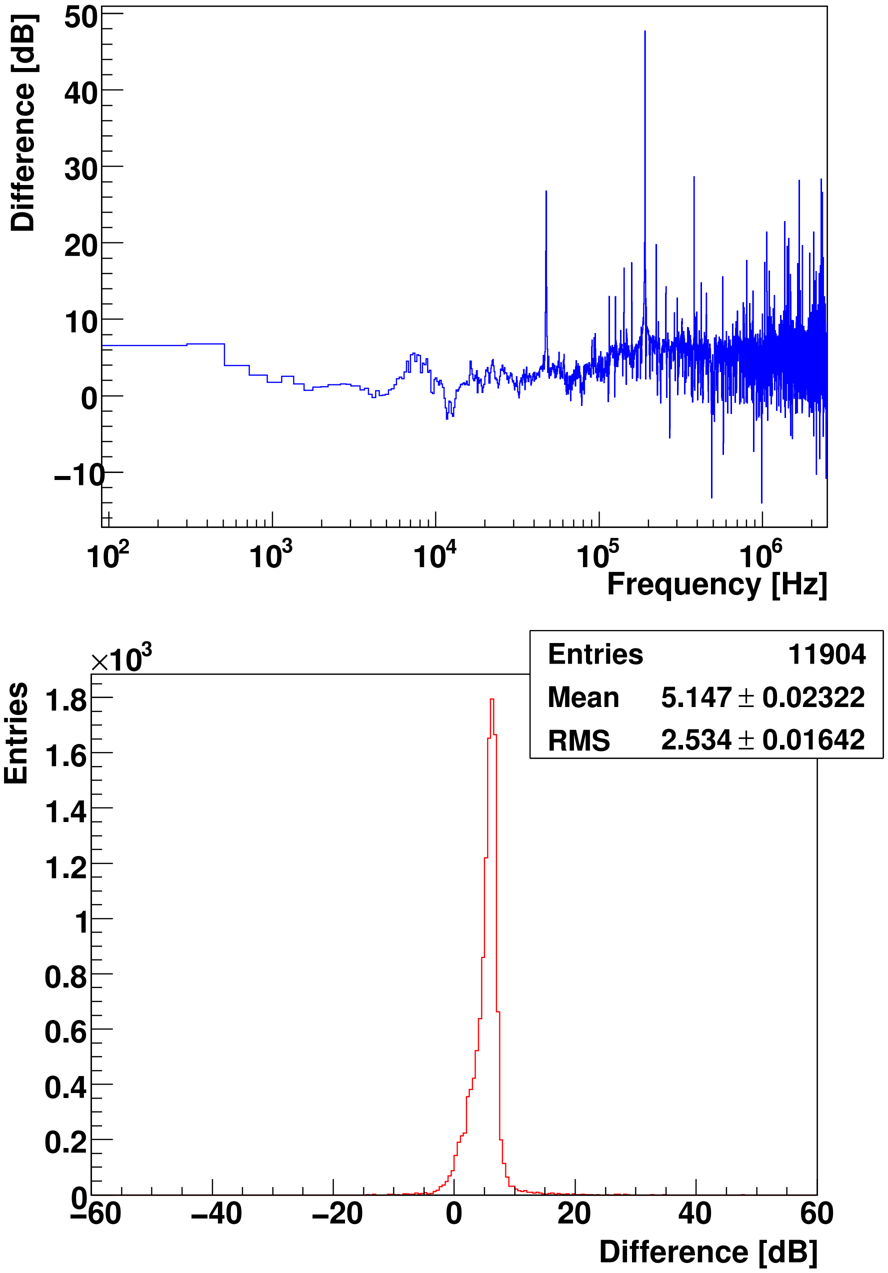

Figure 11.15: top: Difference of the recorded noise with applied 2300 V and without HV-PS for ch0 and combined power supply, bottom: Distribution of the data. The plots are further described in the text.

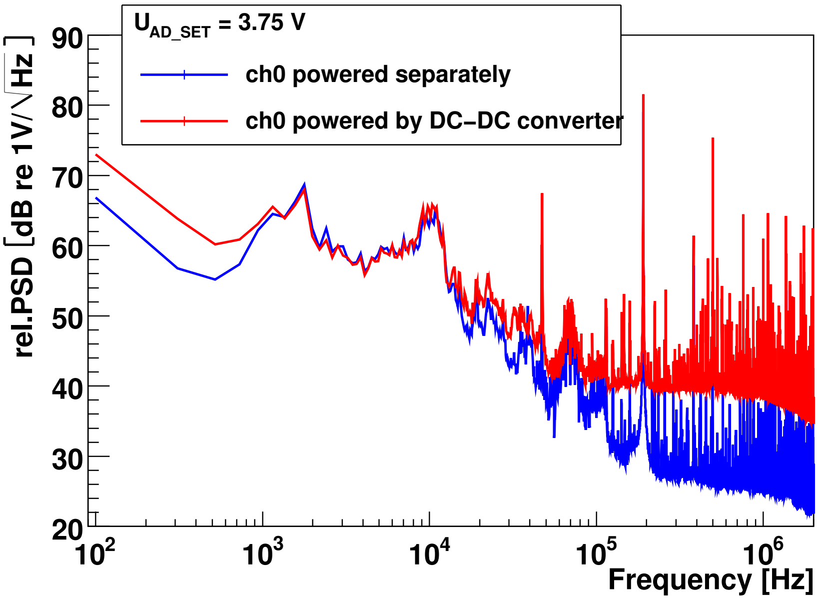

Figure 11.16: Combined ambient and inherent noise recorded with applied 2300 V with and without DC-DC converter. The plot is further described in the text.

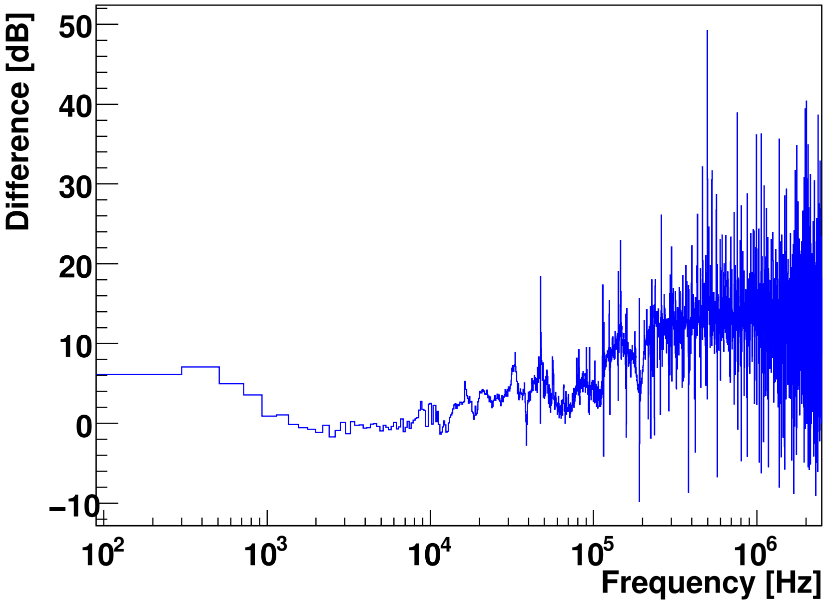

(a) A gl

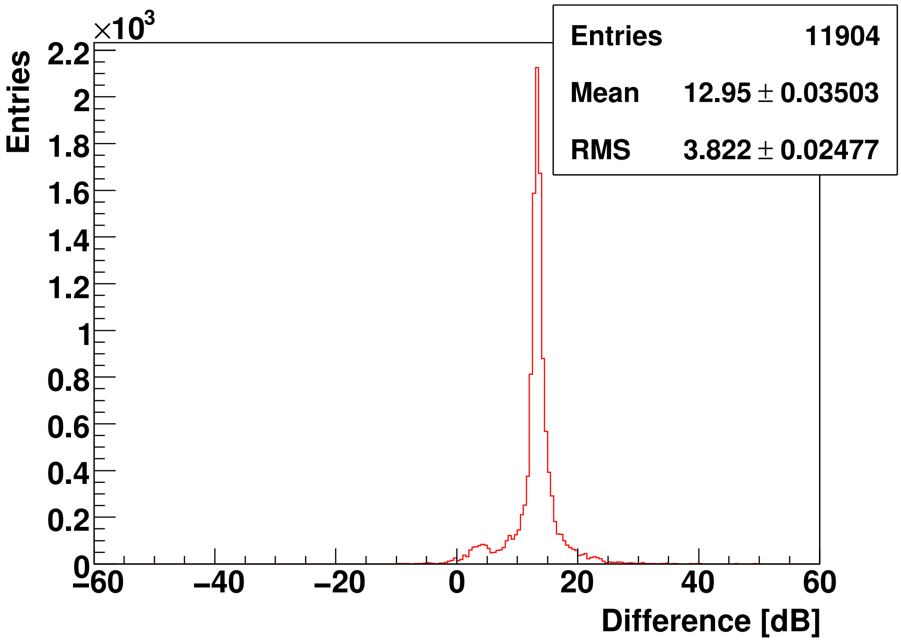

(b) A gull

Figure 11.17: Difference of the recorded noise with applied 2300 V with and without DC-DC converter. The plot is further described in the text.

Part VI

Summary and Conclusion

Chapter 12

Summary

Within the scope of this work extensive studies on different kinds of acoustic sensors were performed. One main part being the calibration of sensors for the following reasons:

- Differences between the ambient noise characteristics in the deep-sea recorded by the AMADEUS setup within ANTARES and the ones expected from simulations. These differences occur on a 4 dB level in the compared data;
- The recovery of ANTARES detector Line 12 (L 12) allowing to test the change in performance of acoustic sensors which were exposed to the deep-sea environment.

In addition to these calibrations of standard AMADEUS sensors efforts were made to develop and characterise new acoustic devices, opto-acoustical modules called OAMs, taking into accout the experiences made in AMADEUS. These OAMs combine two complementary detection strategies:

- An optical part consisting of a PMT inside a pressure resistant glass sphere, the standard device for water (ice) Cherenkov neutrino telescopes;
- An acoustical part based on the design of the Acoustic Modules (AMs) in AMADEUS, therefore acoustic sensors are glued inside the same sphere housing the PMT.

This combination provides the OAM with a set of unique properties.

As plausible reasons for the observed discrepancy between measured and simulated noise spectra, the influence of hydrophone support structures and of the readout electronics were suspected. To test these assumptions, different test setups were created and measurements were performed. The results for this measurements showed only minor changes in the obtained hydrophone sensitivities and could not explain the aforementioned differences. With a high probability it can be excluded that the discrepancies are generated in the DAQ path, but are of the noise generation and propagation mechanism which have to be studied further.

The acoustic devices which were unmounted from L 12 (HTI/LTI hydrophones and AMs) were transported to ECAP, where the functionality of all sensors was tested. Two inoperable sensors were exchanged which were damaged during the pressurisation of deployment and recovery. After the recovery spallings on two lower AM spheres caused by their mounting as well as one detached sensor was observed. As repair measures all AMs were opened and all sensors reglued accordingly to replacement hemispheres. After all sensors were tested successfully, a full calibration set with different signal pulses was performed for every single sensor. The results of this calibrations were compared to the calibrations performed prior to the first deployment of the detection line. The differences for the hydrophones, in the order of a few dB, in the obtained spectra show only a small degradation of the sensors due to the exposure to the deep-sea environment. The differences for the AMs are more obvious but less meaningful as all AM sensors were reglued and thus cannot be assumed identical to the original version. The calibration measurements are biased by systematic uncertainties. In the short time of about seven weeks, between the recovery with subsequent transport of the devices and the return of the devices for reintegration on L 12 and final testing, it was not possible to optimise the test setup or to eliminate other biasing effects. The data obtained during the calibrations contain additional not analysed information with the potential to improve these measurements. This further improvements have to be achieved by processing of the data with refined algorithm and methods. The acoustic devices used in AMADEUS continue their operation with suited performance and taking data continously since their successful reconnection.

The studies towards OAMs concerning the combination of two complementary detection devices, which were started in the scope of this work, showed first promising results. The effect of high voltage generation inside an OAM as well as the influence of a combined power supply (of both high voltage power supply and acoustic sensor) on the performance of an acoustic sensor was studied. The main influences on the acoustic sensor in these measurements occurred in high frequency ranges irrelevant for acoustic particle detection. The remaining influences, mostly narrow frequency bands, can be removed by improvements of the used devices. Further tests are ongoing to take the next steps towards OAMs.

Chapter 13

Conclusion

The results presented in this work validate the high-performance of all acoustic devices used in the AMADEUS setup. The exposure to the deep-sea environment with its high ambient pressure for about 300 days (for the devices on Line 12 of the ANTARES neutrino telescope) resulted in no significant degradation of the performance of the involved sensors. Only at the pressurisation and depressurisation during the deployment and recovery one out of 18 sensors was damaged. This allows for ongoing long term studies of the deep-sea acoustic environment with AMADEUS with stable data-taking conditions. Such studies are essential to validate the feasibility of acoustic neutrino detection.

All custom-built hydrophones developed at the ECAP show comparable performance to the commercial sensor types rendering them a reasonable alternative. The results of the performed calibrations with respect to the results of the calibrations performed prior to deployment confirm this statement.

The performed calibrations with different signal pulses contain a lot of information not used in this work and thus a potential for the understanding of the acoustic devices. To uncover all informations from these calibration measurements as well as to refine the measurements with equivalent devices in the laboratory has to be part of future work.

The feasibility of the AMs and their successful operation with very good direction reconstruction capabilities paved the way for further developments. The performed first principle tests with a combination of acoustical and optical detection devices into one detector element shows promising results for the design of an opto-acoustical module (OAM). These modules might build up parts of a next generation large scale neutrino telescope.

Appendix A

Differences in the obtained data

A.1 HTI hydrophones

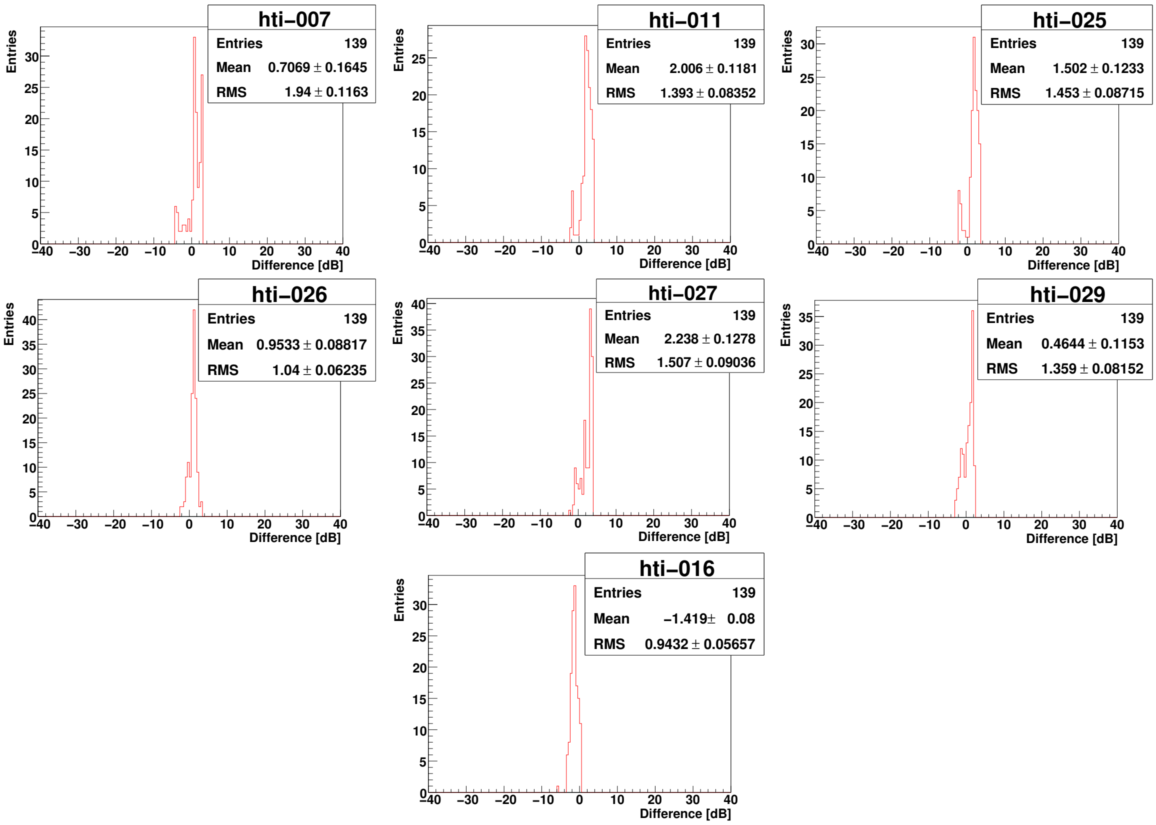

Figure A.1: Distribution of differences in the performed HTI calibrations (sensitivity prior to deployment minus sensitivity after recovery).

A.2 LTI hydrophones

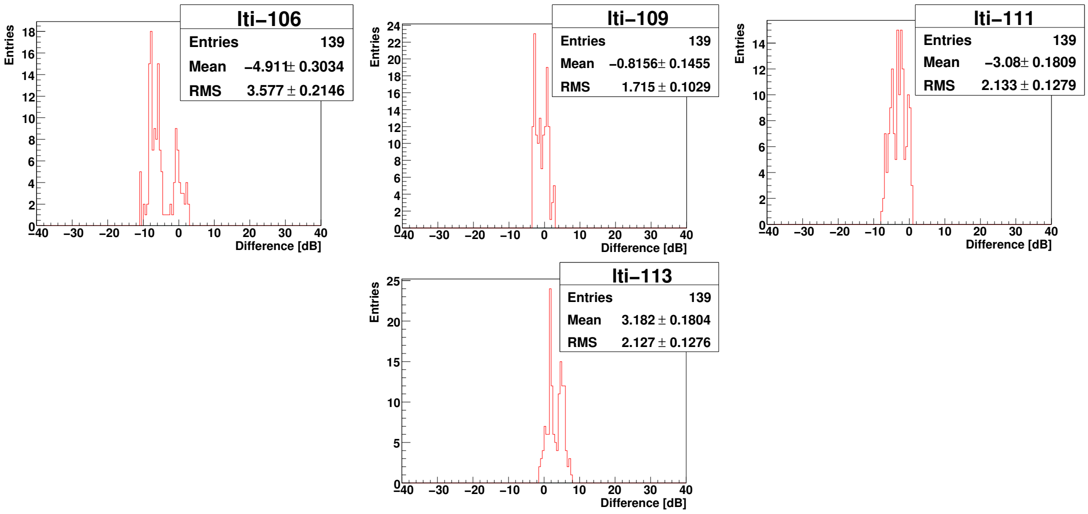

Figure A.2: Distribution of differences in the performed LTI calibrations (sensitivity prior to deployment minus sensitivity after recovery).

A.3 AMs

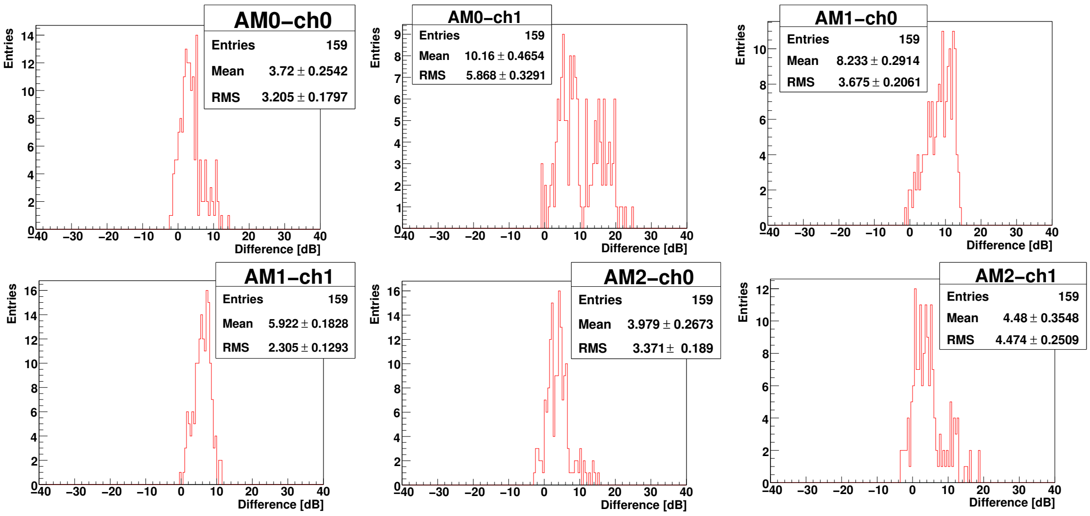

Figure A.3: Distribution of differences in the performed AM calibrations (sensitivity prior to deployment minus sensitivity after reglueing). These distributions show no real evolution of the AMs as the compared sensors are not identical (see Section 7.2).

Appendix B

AM assembly

Assembly of Acoustic Modules

Version 0.9

Author: Alexander Enzenhöfer

alexander.enzenhoefer@physik.uni-erlangen.de

Abstract

This document describes the procedure of assembling the so called Acoustic Modules (AMs) developed at ECAP[1]. These AMs are part of the AMADEUS[2]system which studies the feasibility of acoustic particle detection in the deep sea within the ANTARES[3]detector. Different sensor types and configurations were used in the AMADEUS setup. For the AMs, acoustic sensors are mounted to the inside of standard ANTARES OM glass spheres. These acoustic sensors in turn consists of piezo electrical ceramics and their preamplifiers (due to the small signal amplitudes relevant for acoustic particle detection).

B.1 Preparation

B.1.1 Required Material

- Acoustic sensors, cylindrical shape with 28 mm in diameter and 60 mm in length (28 × 60 mm) see Figure B.1, consisting of:
  Piezo disk, 25.4 × 10 mm, connected to a preamplifier printed circuit board and secured with polyurethane into a copper tube to ensure electromagnetic shielding and providing the sensor with a rigid structure;

- Two glass hemispheres, *"VITROVEX 17"-sphere"*, one with penetrator to connect the sensors with the detector;

- Rubber o-ring, 32 × 5 mm, to define the position of the sensor and to prevent the glue from spreading allover the glass;

- Instant adhesive in gel form, *"UHU sekunden alleskleber gel - ohne Lösungsmittel"*, to glue the rubber o-ring to the inside of the hemisphere;

- Lint-free cloth, to clean the hemisphere and the sensors;

- 2-component adhesive on a epoxy resin base for heavy-duty requirements, *"2-Komponentenkleber UHU plus endfest 300"*, to glue the sensors to the hemisphere;

---

[1] Erlangen Centre for Astroparticle Physics (http://www.ecap.physik.uni-erlangen.de)

[2] ANTARES Modules for Acoustic DEtection Under the Sea (http://www.acoustics.physik.uni-erlangen.de)

[3] Astronomy with a Neutrino Telescope and Abyss environmental RESearch (http://antares.in2p3.fr)

- Ethyl alcohol, *spirit*;
- Lint-free gloves;
- Adhesive tape, *“tesafilm”*;
- Permanent marker.

B.1.2 Preparation of the sensors

The sensors have to be cleaned very carefully, see Figure B.1. This was done with ethyl alcohol and lint-free cloth. Afterwards they are stored at a place, where they are not exposed to pollution.

Figure B.1: left: both sensors ready for mounting, right: cleaned surface of one sensor, here sensor 4.

B.1.3 Preparation of the hemisphere

Cleaning of the hemisphere

To ensure a good connection of hemisphere and sensors and to help recognize the marking on the glass, the hemisphere also has to be cleaned very carefully with ethyl alcohol and lint-free cloth.

Position of the sensors

Before mounting the sensors to the hemisphere, the precise position of the sensors in the final AM was determined. For the design of the AM the decision was made to mount them:

- 45° below the equator of the hemisphere, which means that all 6 sensors (3 per AM) are located in horizontal plane when they are integrated on the OMF (the same support-structure as for OMs is used);
- separated by 60° on the great circle (i.e. the circle with its centre at the centre of the sphere) defined through the item above, to provide the storey with full geometrical coverage in the horizontal plane. This 60° angle on the great circle results in a 90°

angle at the smaller circle in the horizontal plane of the storey that intersects the positions of both sensors.

To get the position it is helpful to draw some auxiliary lines and points on the outer side of the hemisphere. The first point is the pole of the hemisphere, see Figure B.2, the second one is a point along the equator which is chosen as origin in between the final position of both sensors. From this origin one has to go 1/8 of the circumference of the equator, corresponding to 45° or about 17 cm for a 17“-diameter sphere, to the left and to the right along the equator and mark the endpoints. From these two new points draw a line to the pole. These are the azimuthal-coordinates (φ-coordinates) of the sensors. On this two lines one has to go again 1/8 of the circumference from the equator to the pole to get the polar-coordinate (ϑ-coordinate). Around this final points, draw two circles with the diameter of the copper tube to get the region where to glue the rubber o-ring to the inside of the hemisphere. Protect this points and circles by applying some transparent adhesive tape on them as seen on Figure B.2.

Figure B.2: left: pole, right: position of the sensors on the outside of the hemisphere.

B.2 Glueing

B.2.1 Glueing of the rubber o-ring

Turn the sphere to allow working on the inside, see Figure B.3, and clean it again very carefully with lint-free cloth and ethyl alcohol. In the same way clean the rubber o-ring. Handle the o-ring with lint-free gloves to ensure that the o-ring stays clean. Put some instant adhesive on the rubber o-ring and glue it to the position marked from outside with little pressure and wait for a few seconds, see Figure B.4. Fix the o-ring additionally with some adhesive tape to ensure a correct positioning during hardening. Depending on which adhesive is used, wait for 5 to 10 minutes; in the meantime prepare the second o-ring and proceed as before, see Figure B.4. While waiting for the hardening of the adhesive joint of the second o-ring, prepare the 2-component adhesive.

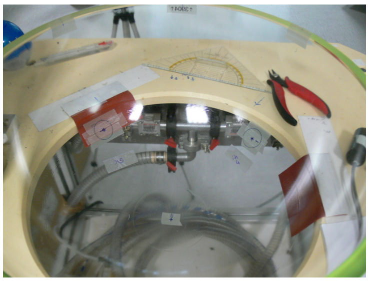

Figure B.3: View on the inside of the hemisphere with the positions of the sensors visible through the glass.

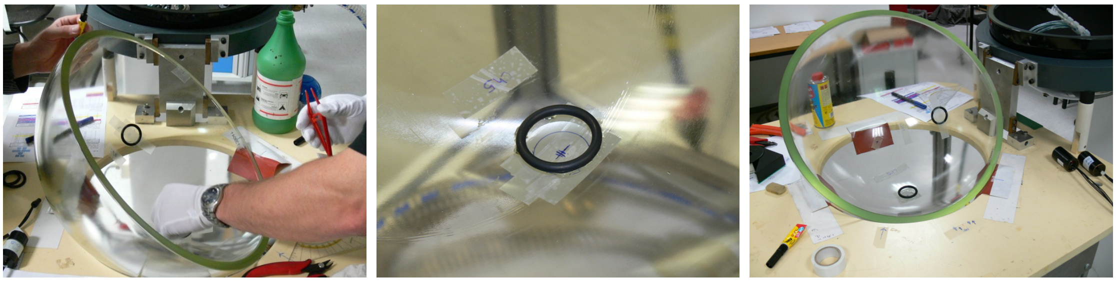

Figure B.4: left: glueing of one o-ring, middle: glued o-ring, right: both o-rings, with one fixed by adhesive tape.

B.2.2 Preparation of the 2-component adhesive

Mix the two components as described in the instructions for the adhesive[4]. Afterwards outgas the adhesive with a vacuum pump at approx. 0.2 bar pressure until all big air bubbles have been removed. After 10 min of outgasing, it was observed that the number of bubbles did not decrease anymore; at the same time, 10 min is short compared to the working time of the adhesive of 2 h, such that further processing as described in the instructions is not affected. The adhesive is now ready for use.

B.2.3 Glueing of the sensors

In order to keep the glueing as easy as possible and in order to prevent the adhesive from spreading into the sphere, position the sphere in such way that the sensor is in the lowest possible position. This is an additional precaution due to the long setting time of about 12 hours and the low viscosity of the adhesive which keeps it liquid for a long time. Then fill the o-ring with a layer of about 1 mm adhesive by carefully avoiding big air bubbles, see Figure B.5.

---

[4] For the rest of this text, the 2-component adhesive is just called adhesive as no other adhesive is used from now on.

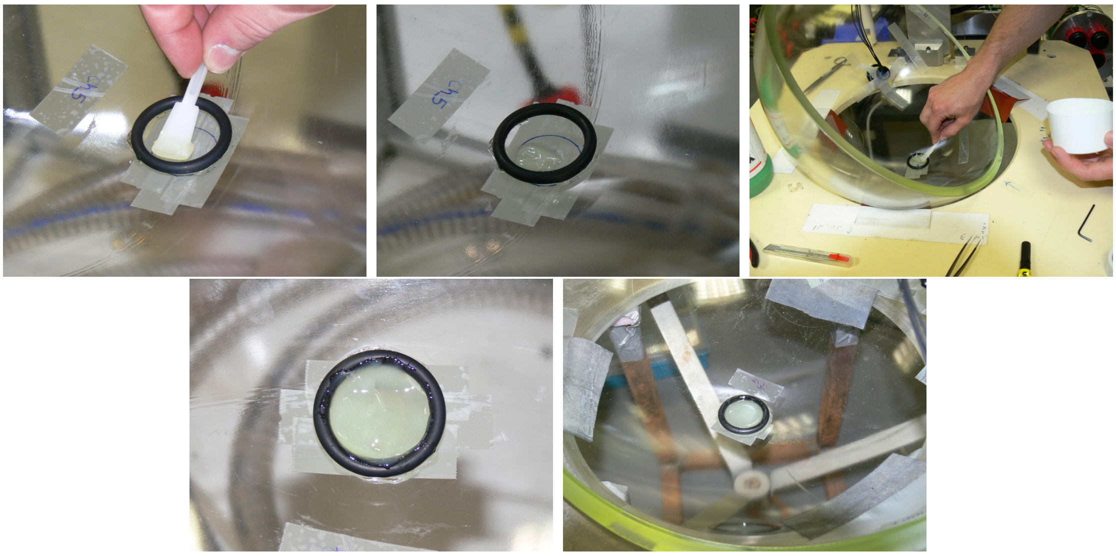

Figure B.5: top: Filling of the o-ring with the adhesive, bottom: finished filling.

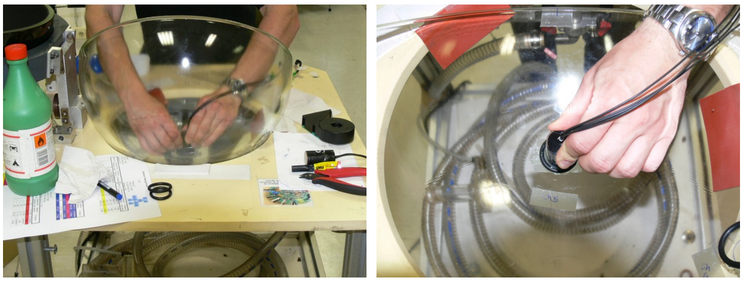

Figure B.6: Cant (left) and then press the sensor to the glass (right).

Also put a layer of about 1 mm of adhesive on the piezo surface to cover any roughness of the surface which could cause air bubbles. Cant the sensor on one side of the o-ring and then press it to the glass while turning it upright (Figure B.6). In the last step check the position of the sensor to be concentric with the marking of Section 1.3.2 and fix the sensor to the glass with adhesive tape (Figure B.7). To enlarge the connected area put some adhesive besides the o-ring. After about 10 to 12 hours (depending on the adhesive used) proceed for the second sensor using the same procedure (Figure B.8). For the closing procedure of the sphere refer to ANTARES Technical notes 3-OMS-00-19-A.

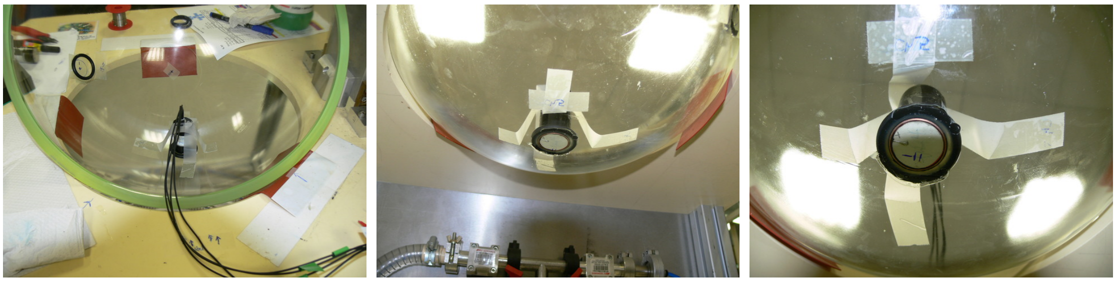

Figure B.7: Sensor fixed by adhesive tape.

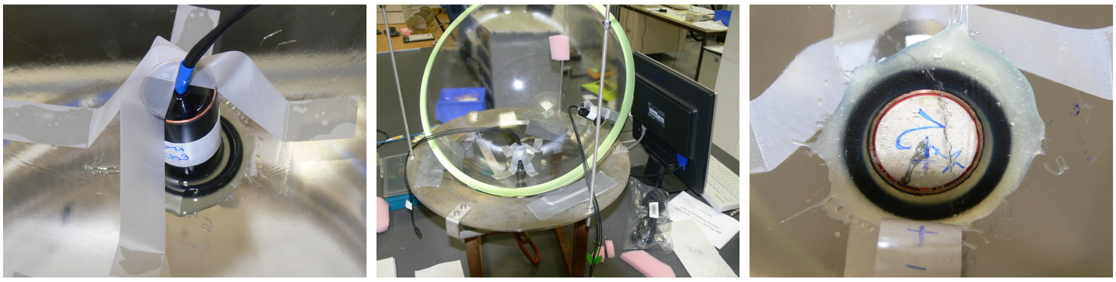

Figure B.8: Finished sensors glued to the hemisphere and quality check through the glass.

B.3 Finished AMs

Here are some photos of the finished AMs, taken at the laboratory in Erlangen after glueing, before closing (Figure B.9) and Foselev after integration on Line 12 (Figure B.10).

Figure B.9: Erlangen.

Figure B.10: Foselev.

List of Figures

List of Tables

Bibliography

[1] G. A. Askaryan. *Hydrodynamic Radiation From the Tracks of Ionizing Particles in Stable Liquids.* Sov. J. At. En. **3** (1957) 921.

[2] G. A. Askaryan, B. A. Dolgoshein, A. N. Kalinovsky and N. V. Mokhov. *Acoustic detection of high energy particle showers in water.* Nucl. Instr. Meth. **164** (1979) 267.

[3] J.A. Aguilar et al (ANTARES Coll.). *AMADEUS - The Acoustic Neutrino Detection Test System of the Deep-Sea ANTARES Neutrino Telescope.* To be submitted to Nucl. Instr. Meth. **A**, preprint obtainable from robert.lahmann@physik.uni-erlangen.de.

[4] The AMADEUS homepage. *http://www.acoustics.physik.uni-erlangen.de/* .

[5] The ANTARES Collaboration. *A Deep Sea Telescope for High Energy Neutrinos.* arXiv:astro-ph/9907432 (1999).

[6] The ANTARES homepage. *http://antares.in2p3.fr/* .

[7] The ECAP homepage. *http://www.ecap.physik.uni-erlangen.de/* .

[8] P. Amram et al. (ANTARES Coll.). *The ANTARES optical module.* Nucl. Instr. Meth. **A 484** (2002) 369.

[9] High Tech, Inc. *http://home.att.net/∼hightechinc/* .

[10] C.L. Naumann. *Development of Sensors for the Acoustic Detection of Ultra High Energy Neutrinos in the Deep Sea.* Doctoral thesis, Univ. Erlangen-Nürnberg, (2007, FAU-PI4-DISS-07-002).

[11] The KM3NeT homepage. *http://www.km3net.org/* .

[12] S. Kuch. *Aufbau eines Hydrophon-Teststands und vorbereitende Studien zur akustischen Detektion ultrahochenergetischer Neutrinos.* Diplomarbeit, Univ. Erlangen-Nürnberg, (2003, FAU-PI1-DIPL-03-002).

[13] P. Kollmannsberger. *Studien zur akustischen Detektion ultrahochenergetischer Neutrinos mit Hilfe des piezoelektrischen Effekts.* Diplomarbeit, Univ. Erlangen-Nürnberg, (2004).

[14] R. Ostasch. *Entwicklung einer Kalibrationsquelle für Hydrophone zur akustischen Detektion ultrahochenergetischer Neutrinos.* Diplomarbeit, Univ. Erlangen-Nürnberg, (2004, FAU-PI1-DIPL-04-001).

[15] K. Graf. *Teststrahlmessungen zur akustischen Neutrinodetektion: Thermoakustische Schallerzeugung in Wasser.* Diplomarbeit, Univ. Erlangen-Nürnberg, (2004, FAU-PI1-DIPL-04-002).

[16] S. Schwemmer. *Testmessungen zur akustischen Neutrinodetektion mit einem Nd:YAG-Laser.* Diplomarbeit, Univ. Erlangen-Nürnberg, (2005, FAU-PI1-DIPL-05-002).

[17] K. Salomon. *Simulation und Messung verschiedener Hydrophonkomponenten zur akustischen Teilchendetektion.* Doctoral thesis, Univ. Erlangen-Nürnberg, (2007).

[18] T. Butz. *Fouriertransformation für Fußgänger.* Vieweg+Teubner, 6. Edition, 2009.

[19] Agilent Technologies. *http://www.agilent.com/* .

[20] LeCroy Corp. *http://www.lecroy.com/.*

[21] ROOT - A Data Analysis Framework. *http://root.cern.ch/* .

[22] K. Graf. *Experimental Studies within ANTARES towards Acoustic Detection of Ultra-High Energy Neutrinos in the Deep-Sea.* Doctoral thesis, Univ. Erlangen-Nürnberg, (2008, FAU-ECAP-DISS-08-001).

[23] FFTW. *http://www.fftw.org/* .

[24] M. Neff. *Studie zur akustischen Teilchendetektion im Rahmen des ANTARES-Experiments: Entwicklung und Integration von Datennahmesoftware.* Diplomarbeit, Univ. Erlangen-Nürnberg, (2007, FAU-PI1-DIPL-07-003).

[25] SEA CON®. *http://www.seaconbrantner.com/* .

[26] CT. Chen and FJ Millero. *Speed of sound in seawater at high pressures.* J. Acoust. Soc. Am., Volume 62, Issue 5, pp.1129-1135 (1977).

[27] Nautilus Marine Service GmbH. *http://www.nautilus-gmbh.de/* .

[28] M. Ardid for the ANTARES Coll. *Positioning system of the ANTARES neutrino telescope.* Nucl. Instr. Meth. **A 602** (2009) 174.

[29] The Texas Instruments homepage. *http://www.ti.com/* .

[30] SubConn®. *http://www.subconn.com/* .

[31] R. Lahmann. *Specifications of the cables for acoustic storeys with hydrophones.* ANTARES technical note to be published .

[32] iseg Spezialelektronik GmbH. *http://www.iseg-hv.de/* .

[33] Delta Elektronika BV. *http://www.delta-elektronika.nl/* .

[34] Heinzinger electronic GmbH. *http://www.heinzinger.de/* .

[35] TRACO ELECTRONIC AG. *http://www.tracopower.com/* .

Danksagung

An dieser Stelle möchte ich mich ganz herzlich bei allen bedanken die diese Arbeit ermöglicht haben und maßgeblich am erfolgreichen Abschluß meines Studiums beteiligt waren. All jene die ich vergessen habe hier zu erwähnen, mögen mir dies bitte verzeihen.

Besonderer Dank gilt:

Herrn Prof. Dr. Uli Katz für die Vergabe dieses interessanten Themas sowie für die mir gewährte Unterstützung und Freiheit bei dessen Bearbeitung.

Herrn Dr. Kay Graf und Herrn Dr. Robert Lahmann für die kompetente Betreuung sowie für deren ständige Hilfsbereitschaft.

Den Mitgliedern der Akustik-Gruppe, die mir stets mit Rat und Tat zur Seite standen und mit denen die Zusammenarbeit stets produktiv und angenehm war.

Den Mitgliedern der Erlanger ANTARES-Gruppe sowie allen Mitgliedern des ECAP für die gute Arbeitsatmosphäre.

Den Mitarbeitern der Elektronikwerkstatt, der mechanischen Werkstatt und der Betriebstechnik des Physikalischen Instituts für die Anfertigung der benötigten Geräte und Bauteile.

Anneli Schulz und Martin Wimmer, ohne deren Hilfe einige Messungen zeitlich nicht möglich gewesen wären.

Herrn Prof. Dr. Erhard Steffens, der freundlicherweise die Zweitkorrektur dieser Arbeit übernommen hat.

Herrn Dr. Kay Graf und Herrn Dr. Robert Lahmann danke ich zusätzlich für das sorgfältige Korrekturlesen, sowie für die konstruktiven Korrekturvorschläge nicht nur bei dieser Arbeit.

Carolin Legl für die große moralische Unterstützung vor allem während des Studiums.

Mein ganz besonderer Dank gilt meinen Eltern sowie meinen Geschwistern mit Familie, die mir stets grenzenloses Vertrauen und Unterstützung entgegengebracht haben und damit im Wesentlichen zum Gelingen dieser Arbeit beigetragen haben.

Erklärung

Ich versichere, diese Arbeit selbstständig verfasst und keine anderen als die angegebenen Quellen und Hilfsmittel benutzt zu haben.

Erlangen, im Januar 2010

Alexander Enzenhöfer